IMPROVED SINGLET OXYGEN GENERATION BY A NOVEL BODIPY DYE AND A STUDY OF UPCONVERISON NANOPARTICLES MIXED WITH A FUNCTIONALIZED BODIPY COMPOUND

A thesis submitted in fulfillment of the requirements for the degree of

Masters of Science

of

RHODES UNIVERSITY

by

Martijn Johannes Wildervanck

February 2016

Dedication

To my extraordinary family, for their love and support throughout this journey.

Acknowledgements

My MSc degree was not the accomplishment of myself alone but a collective of all those in my life. First and foremost my gratitude goes out to the staff and support staff of Rhodes University who have, over the years, become somewhat of an extended family. Their collective enthusiasm has cultivated my love for chemistry since undergrad and initiated my passion for the subject. I have the deepest appreciation and respect for my supervisor Dr John Mack and co-supervisor Prof Tebello Nyokong. This work would have been directionless without your teachings and mentorship.

To my home away from home, my fellow lab mates of S22. Work was made fun and the fun times even better, especially with the company of Justin, Zane, Marcel, Ivan, Alison and Taryn. Lastly, this work would not have been possible without the love and support of Shannon Hardman, for all the help during the writing up process at the end of my journey. You continue to be a light in my life.

This work was supported by the DST/NRF South African Research Chairs Initiative for Professor of Medicinal Chemistry and Nanotechnology, and by the South Africa/Japan Joint Science and Technology Research Collaboration (uid: 92425) promoted by the Japanese Society for the Promotion of Science and the National Research Foundation (NRF) (to Prof. Tebello Nyokong). Financial support for the research was also provided by NRF through a CUSR grant (uid: 93627) and a China-South Africa joint research program in cooperation with The National Natural Science Foundation of China (NSFC) (uid: 95421) (to Dr. John Mack). This work was also supported by the

CSIR National Laser Centre, Rental Pool Programme, and the theoretical calculations were carried out at the Centre for High Performance Computing in Cape Town, South Africa.

Abstract

This research explores the use of the versatile 4,4-difluoro-4-boro-3a,4a-diaza-*s*-indacene (BODIPY) dyes and the modification of their spectroscopic properties. The synthesis of a tetramethyl-BODIPY bearing a sterically hindered meso-phenyl ring with an ethynyl functional group at the para-position was compared to that of its freely rotating counterpart with no methyl substituents on the BODIPY core, with the fluorescence properties in particular proving to be markedly different. These phenyl-ethynyl-substituted BODIPYs were used as the starting materials for the synthesis of novel BODIPY dyes for sensor applications via Sonogashira coupling reactions at the ethynyl position, but this resulted instead in the serendipitous synthesis of a novel BODIPY dimer in which the para-positions of the meso-phenyl rings are linked by a diethynyl bridge. Following iodination at the 2, 6-positions, the dimer was found to have a singlet oxygen quantum yield of 0.88, compared to the value of 0.86 that was obtained for the analogous monomer. Since the ε_{max} values for the main spectral bands of the dimers are significantly higher, the compounds may be of interest for singlet oxygen generation applications.

A second study was carried out on the interaction between methyl ester functionalized BODIPY dyes and upconversion nanoparticles (UCNPs) to explore the possible use of BODIPY-UCNP conjugates in biomedical applications. The singlet oxygen generation properties of the BODIPY were tested following iodination at the 2, 6-positions, a singlet oxygen quantum yield value of 0.86 was obtained. Three sets of oleate capped UCNPs were synthesized with different diameters and were rendered water dispersible with the addition of a silica shell. The necessary scaffolding for conjugation to the BODIPY was provided by amine groups following functionalization of this shell.

All of the sets of oleate capped and silica coated UCNPs were characterized by transmission electron microscopy (TEM) and X-ray diffractometry (XRD) and their emission properties were studied upon excitation at 978 nm with a diode laser with a Picoquant Fluotime 300 spectrophotometer that enables the measurement of anti-Stokes emission. The potential utility of UCNP-BODIPY conjugates for singlet oxygen applications, such as PDT, was then assessed.

Table of contents

List of Symbols xi

List of Abbreviations xiii

List of Schemes xvi

List of Tables xviii

List of Figures xix

1. Introduction 2

1.1. Origins of Luminescence 3

1.1.1. Fluorescence and phosphorescence 4

1.1.2. Emission characteristics 8

1.1.2.1. Stokes and anti-Stokes shifts 8

1.1.2.2. The fluorescence quantum yield and lifetime 10

1.1.3. Singlet oxygen generation 13

1.2. BODIPY dyes 15

1.2.1. Structure of the BODIPY core 15

1.2.2. Synthesis and spectral properties 20

1.2.3. Strategies for modification 24

1.2.3.1. A) Meso-aromatic substitution 24

1.2.3.2. B) Photoinduced electron transfer (PeT) 26

1.2.3.3. Core modification strategies and the extension of π conjugation 28

1.3. Nanotechnology 31

1.3.1. Upconversion Nanoparticles ($NaYF_4$: Yb, Er/Gd): The basics 33

1.3.2. Sensitizers and activators 34

1.3.3. Dopant/Host relationship 37

1.3.4. Mechanisms of upconversion 38

1.3.4.1. Energy transfer upconversion (ETU) 40

1.3.5. Size and phase control 42

1.3.6. Synthesis and surface modification 44

1.3.7. Applications of upconversion nanoparticles 46

1.4. Summary of aims 48

2. Experimental 51

2.1. Materials 51

2.2. Instrumentation 51

2.3. Syntheses 54

2.3.1. 4,4-difluoro-1,3,5,7-tetramethyl-8-(4-ethynylbenzene)-4-boro-3a,4a-diaza-*s*-indacene (BDY1) 54

2.3.2. 4,4-difluoro-1,3,5,7-tetramethyl-2,6-diiodo-8-(ethynylbenzene)-4-boro-3a,4a-diaza-*s*-indacene (IBDY1) 55

2.3.3. 4,4-difluoro -8-(4-ethynylbenzene)-4-boro-3a,4a-diaza-*s*-indacene (BDY2) 56

2.3.4. 4,4-difluoro-1,3,5,7-tetramethyl-8-(methyl benzoate)-4-boro-3a,4a-diaza-*s*-indacene (BDY3) 56

2.3.5. 4,4-difluoro-1,3,5,7-tetramethyl-2,6-diiodo-8-(methyl benzoate)-4-boro-3a,4a-diaza-*s*-indacene (IBDY3) 57

2.3.6. Synthesis of *N, N*′-di-(*tert*-Butoxycarbonyl)-4-bromo-1,2-diaminobenzene and *N, N*′-di-(*tert*-Butoxycarbonyl)-4-bromo-1-aminobenzene 58

2.3.7. Synthesis of novel ethynyl bridged BODIPY dimer (AxBDY) 58

2.3.8. Iodination of ethynyl BODIPY dimer (IAxBDY) 59

2.3.9. Synthesis and functionalization of Upconversion Nanoparticles 60

2.3.9.1. Synthesis of oleate capped $NaYF_4$ upconversion nanoparticles 60

2.3.9.2. Silinization of oleate capped upconversion nanoparticles (Si@UCNP) 60

2.3.9.3. Functionalization of silica coated upconversion nanoparticles 61

2.3.9.4. Conjugation of amine functionalized upconversion nanoparticles and iodinated esterBODIPY 61

3. BODIPY Dyes 63

3.1. Synthesis and characterization 64

3.1.1. 4,4-difluoro-1,3,5,7-tetramethyl-8-(4-ethynylbenzene)-4-boro-3a,4a-diaza-*s*-indacene (BDY1) 64

3.1.2. 4,4-difluoro -8-(4-ethynylbenzene)-4-boro-3a,4a-diaza-*s*-indacene (BDY2) 68

3.1.3. 4,4-difluoro-1,3,5,7-tetramethyl-8-(methyl benzoate)-4-boro-3a,4a-diaza-*s*-indacene (BDY3) 71

3.2. Iodination of ethynyl and ester functionalized BODIPYs 74

3.2.1. Synthesis and characterization 74

3.2.2. Singlet oxygen studies 76

3.3. Sonogashira Coupling and a Novel BODIPY dye 78

3.3.1. Sonogashira coupling towards a series novel BODIPY dye 78

3.3.2. Synthesis and characterization of an axial BODIPY dimer (AxBDY and IAxBDY) 81

3.3.3. Iodination and singlet oxygen studies of axial BODIPY dimer (IAxBDY) 85

3.4. Summary of photophysical properties 87

4. Molecular Modelling 91

4.1. Molecular modelling parameters 91

4.2. Electronic structure of BODIPY dyes 91

4.2.1 BODIPYs and their iodination 92

5. Upconversion Nanoparticles 101

5.1. Synthesis of upconversion nanoparticles ($NaYF_4$: Yb/Er/Gd) 102

5.2. Characterization of upconversion nanoparticles 104

5.2.1. Transmission Electron Microscopy (TEM) 104

5.2.2. Powder X-ray Diffraction (XRD) 107

5.2.3. Steady state and time resolved fluorescence spectroscopy 111

5.3. Studies on NIR stimulated singlet oxygen generation: Upconversion and BODIPYs 115

6. Conclusion 122

References 125

List of Symbols

$^1O_2$	-	Singlet oxygen
$^3O_2$	-	Molecular, triplet oxygen
S_0	-	Ground singlet state
S_1	-	First excited singlet state
S_2	-	Second excited singlet state
S_n	-	n^{th} excited singlet state
T_1	-	First triplet state
Z	-	Atomic number
S	-	Spin angular momentum
v’	-	lowest vibrational level of the ground state
v’’	-	lowest vibrational level of the first state
ϕ_F	-	Fluorescence quantum yield
ϕ_F^{std}	-	Fluorescence quantum yield of standard
F	-	Integrated area of fluorescence emission curve
F_{std}	-	Integrated area of fluorescence emission curve of standard
A	-	Absorbance of sample at the excitation wavelength
A_{std}	-	Absorbance of standard at the excitation wavelength
n^2	-	Refractive index for sample
n^2_{std}	-	Refractive index for standard
τ	-	Lifetime

τ_F - Fluorescence lifetime

ϕ_Δ^{std} - Standard singlet oxygen quantum yield

ϕ_Δ - Sample singlet oxygen quantum yield

W^{std} - Rate of standard photobleaching

W - Rate of sample photobleaching

I_{abs}^{std} - Absorbance intensity of standard at cross over wavelength

I_{abs} - Absorbance intensity of sample at cross over wavelength

Ln^{3+} - Trivalent lanthanide ions

α - Cubic crystallographic phase

β - Hexagonal crystallographic phase

ε - Absorption coefficient

List of Abbreviations

PS	-	Photosensitizer
NIR	-	Near infrared
PDT	-	Photodynamic therapy
BODIPY	-	4,4-difluoro-4-boro-3a,4a-diaza-*s*-indacene
UCNP	-	Upconversion nanoparticle
Si@UCNP	-	Silica coated upconversion nanoparticle
UC	-	Upconversion
TTA	-	triplet – triplet annihilation upconverison
TCSPC	-	Time correlated single photon counting
FRET	-	Forster Resonance Energy Transfer
ADMA	-	Anthracene-9; 10 – bis – methylmalonate
DPBF	-	1,3-diphenylisobenzofuran
TPP	-	Tetraphenylporphyrin
TFA	-	Trifluoroacetic acid
DDQ	-	2,3-dichloro-5,6-dicyano-*p*-benzoquinone
PeT	-	Photo induced electron transfer
HOMO	-	Highest occupied molecular orbital
LUMO	-	Lowest unoccupied molecular orbital
MO	-	Molecular orbital
DFT	-	Density functional theory

TD-DFT - Time-dependent density functional theory

CR - Cross relaxation

ETU - Energy transfer upconversion

XRD - X-ray diffraction

OE - Oleic acid

AuNP - Gold nanoparticle

PEG - Poly ethylene glycol

DCM - Dichloromethane

NIS - *N*-iodosuccinimide

TEOS - Tetraethoxysilane

PET - Petrleum ether

TEA - Triethylamine

DMF - Dimethyl formamide

THF - Tertahydrafuran

APTES - 3-aminopropyltriethoxysilane

TEM - Transmission electron microscope

UV-vis - Ultraviolet/visible light

FTIR - Fourier transform Infrared

NMR - Nuclear magnetic resonance

TLC - Thin layer chromatography

ESI - Electron spray ionization

BDY1 - 4,4-difluoro-1,3,5,7-tetramethyl-8-(4-ethynylbenzene)-4-boro-3a,4a-diaza-*s*-indacene

IBDY1 - 4,4-difluoro-1,3,5,7-tetramethyl-2,6-diiodo-8-(ethynylbenzene)-4-boro-3a,4a-diaza-*s*-indacene

BDY2 - 4,4-difluoro-8-(4-ethynylbenzene)-4-boro-3a,4a-diaza-*s*-indacene

IBDY2 - 4,4-difluoro-2,6-diiodo-8-(4-ethynylbenzene)-4-boro-3a,4a-diaza-*s*-indacene (theoretical compound)

BDY3 - 4,4-difluoro-1,3,5,7-tetramethyl-8-(methyl benzoate)-4-boro-3a,4a-diaza-*s*-indacene

IBDY3 - 4,4-difluoro-1,3,5,7-tetramethyl-2,6-diiodo-8-(methyl benzoate)-4-boro-3a,4a-diaza-*s*-indacene

AxBDY - Ethynyl bridged BODIPY dimer

IAxBDY - Iodination of ethynyl BODIPY dimer

List of Schemes

Scheme 1.1: Two synthetic pathways towards BODIPY dyes. Pathway A follows the one pot reaction utilizing TFA as the oxidizing agent. The second pathway, B, involves the use of aqueous HCl (0.18 M) with the resulting dipyrromethane 1.1 precipitating out of solution. Following purification the subsequent synthetic steps and reaction conditions are identical.

Scheme 3.1.1: Pathway outlining the synthesis of the meso-substituted ethynyl BODIPY (BDY1).

Scheme 3.1.2: An HCl catalyzed method for the selective synthesis of the ethynyl functionalized pyrrole BODIPY (BDY2).

Scheme 3.1.3: The synthesis of BDY3.

Scheme 3.2.1: Synthetic procedure for the iodination at the 2, 6-positions of BDY1 and BDY2. Reaction carried out under Ar gas.

Scheme 3.3.1: The Boc_2O protected diamine (A) and amine (B) groups formed by using guanidine hydrochloride as a green organo-catalyst. The synthesis was carried out using procedures described in the literature.

Scheme 3.3.2: The Sonogashira coupling cycle of Boc_2O protected groups with the BDY1 (Scheme 3.1.1) using $PdCl_2(PPh_3)_2$ as the catalyst, a CuI co-catalyst and piperidine as the amine base (**1a-c**). A derivative formed by using the BDY2 is also proposed (**2a-c**).

Scheme 3.3.3: Pathway outlining the Sonogashira coupling reaction for the synthesis of AxBDY. The functionalized with iodine atoms at both positions BODIPY core is also depicted resulting in the formation of IAxBDY. The reaction was conducted under Ar atmosphere.

Scheme 5.1: Synthetic pathway for silica modified and amine functionalized of UCNPs

List of Tables

Table: 3.1.1. Photophysical data for synthesized BODIPY compounds.

Table 4.2.1: TD-DFT calculated transitions for the synthesized BODIPY compounds with a B3LYP optimized geometries and CAM-B3LYP functional.

Table 4.2.2: TD-DFT calculated transitions for the BODIPY compounds AxBDY and IAxBDY with a B3LYP optimized geometries and CAM-B3LYP functional.

List of Figures

Figure 1.1: A Jablonski diagram showing the major transitions associated with the luminescence processes. Electronic excitation to either the second (S_2) or first (S_1) excited states with their respective vibronic energy levels is indicated (blue). The internal conversion, process A, shows the transition from $S_2 \rightarrow S_1$ and subsequent vibronic relaxations through internal conversions to its lowest energy level which, according to Kasha's Rule, is the origin of the fluorescence process. Energy loss during relaxation from an electronic level can also take place without the emission of a photon, this is referred to as nonradiative decay and is shown by process (B). Here, energy is lost as heat through phonon interactions or through internal conversion to the S_0 state. Intersystem crossing (C) involves a change in spin of an electron so that a triplet (T_1) state is formed. The T_1 state is the origin of the slower phosphorescence process. The final process (D) is termed as delayed fluorescence or E-type fluorescence.

Figure 1.2: A Morse potential diagram (top) displaying the excitation profile from the electronic ground state (v' = 0) to the individual excited vibrational levels (v'' = 1 to 4) as well as the electronically excited state (v'' = 0) to the ground vibrational levels (v' = 1 to 4). Below is the corresponding fluorescence spectrum for this absorption (blue line) and emission (emission), characteristically mirror images of each other.

Figure 1.3: Figure 1.3: Typical data obtained during Φ_F measurements using the TCSPC method at a 165 ns pulse length with residual counts shown.

Figure 1.4: The typical structure of a tetraphenylporphyrin (left) showing the structural similarity to a meso-phenyl-BODIPY (right). The TPP example above is shown in its metal free form which can be chelated with the addition of a metal bearing a 2+ oxidation state. The BODIPY on the other hand is chelated with a BF_2 moiety.

Figure 1.5: Typical resonance structure of the BODIPY chromophore showing IUPAC numbering system (1–8) for the possible functionalization sites. Also indicated is the common nomenclature that is used widely in literature.

Figure 1.6: A diagram of the first unsubstituted BODIPY crystal structure obtained by Tran et al. The atoms are shown with 50% probability displacement ellipsoids.

Figure 1.7: The excitation (dotted) and emission (solid) profile of an unsubstituted BODIPY dye run in MeOH.

Figure 1.8: The absorption (abs) and emission (em) wavelengths of the main spectral bands for various BODIPY dyes and how they relate to asymmetric and symmetric substitution around the BODIPY core.

Figure 1.9: Diagram showing the sterically hindered *meso*-phenyl group (1.4) with a 1,3,5,7 tetramethyl BODIPY core and the freely rotating analogue with an unsubstituted core (1.5). Images taken from **Schemes 2.3.1** and **2.3.2.**

Figure 1.10: A Zn^{2+} ion sensor based on intramolecular electron transfer from donor (D) to acceptor (A). Compounds bearing suitable functionality, shown as an inset on the right, are known PeT compounds and will favourably undergo the process.

Figure 1.11: Styrylation of the BODIPY core and how it relates to the absorption maxima with respect to position, number and substituent.

Figure 1.12: An unsubstituted BODIPY core displaying the resonant forms for delocalization of the positive charge. The 2, 6-positions possess a significant negative charge and as such has a more nucleophilic character.

Figure 1.13: Mechanisms of energy transfer between sensitizer and activator ions within UCNPs. Resonant energy absorption (A) takes place with the transfer of a real photon and resonant absorption based on dipole-dipole coupling (B) which is nonradiative in nature. C displays a small energy mismatch between sensitizer and activator, which is bridged by Stokes phonons, and mechanism B the cross relaxation between level pairs of dopant ions.

Figure 1.14: Schematic showing the different mechanisms producing anti-Stokes emission. Solid blue lines indicate photon absorption and dashed versions resonant transfer absorption. Solid red lines indicate emission. E_1 and E_2 indicate excited state 1 and 2, respectively, while V_1 and V_2 are the 1^{st} and 2^{nd} virtual state, respectively.

Figure 1.15: Sensitized energy transfer upconversion (sensitized ETU) between the Yb^{3+} and Er^{3+} ions. Population and relaxation from the higher energy levels $^2H_{9/2}$, $^2H_{11/2}$ and $^4F_{9/2}$ states result in the blue, green and red emission bands, respectively.

Figure 1.16: Diagram showing the effects phase change dopants (Sm^{3+}, Nd^{3+}, Gd^{3+}) have on the energy transfers from sensitizer to activator. Insets for α-phase (A) and β-phase (B) are also shown with the different arrangement of ions in their respective unit cells. A: dark blue balls show the RE^{3+} and Na cation sites. B: Light blue balls represent the Na^+ sites (1) and purple the RE^{3+} sites (2). F^- ions, in both cases, are highlighted in yellow.

Figure 1.17: Diagram outlining the organic compounds synthesized with their assigned nomenclature used throughout.

Figure 2.1: Diagram showing the internal components and laser path for the Fluotime 300.

Figure 3.1.1: Normalized absorption (blue), excitation (orange) and emission (green, λ_{exc} 480 nm) spectra of BDY1. Corner inset showing the absorption coefficient calculation (summarized in Table 3.1.1) from spectra measured in THF.

Figure 3.1.2: Exponential decay curve found for BDY1 measured in ethanol. Residuals indicated below (λ_{exc} 518 nm).

Figure 3.1.3: Ground state absorption spectrum for BDY2 (toluene). The inset diagram displays the calculation for the ε value (THF) and the rotational motion experienced by the ethynylphenyl group.

Figure 3.1.4: Ground state absorption (red) spectrum of BDY3 with the excitation (blue) and emission (orange, λ_{exc} 480 nm) run in toluene. A linear plot for the calculation of the ε value (THF) is presented as an inset.

Figure 3.1.5: Experimental fluorescence decay curve in THF with residuals (λ_{exc} 519 nm)

Figure 3.2.1: Ground state absorption spectrum showing the wavelength shift from BDY1 (dashed red) to IBDY1 (red) and BDY3 (dashed blue) to IBDY3 (blue). Spectrum produced in toluene.

Figure 3.2.2: Decrease in DPBF absorbance over 30 s intervals in the presence of Rose Bengal as the ϕ_{Δ} standard. Excitation was carried out at 536 nm for IBDY1 and 542 nm for IBDY2 (EtOH).

Figure 3.3.3: Absorption (blue) and Fluorescence spectra obtained (λ_{exc} 480 nm) for AxBDY at room temperature in toluene. A linear plot showing absorption co-efficient (THF).is also displayed.

Figure 3.3.4: Fluorescence decay profile for AxBDY (ethanol) with residuals (λ_{exc} 522 nm).

Figure 3.3.5: Shift in absorption spectrum observed of the AxBDY (dashed blue) to IAxBDY (orange) with a linear plot showing the calculation for the ε value (THF).

Figure 3.3.6: Singlet oxygen degradation over 30 s intervals with Rose Bengal as the standard and DPBF as the scavenger molecule.

Figure 4.2.1: Figure 4.2.1: HOMO and LUMO diagrams (isosurface value of 0.05 a.u) for BODIPY dyes showing the major transitions associated with the main spectral bands in the visible region. All of the compounds were synthesized with the exception of IBDY2.

Figure 4.2.2: The MO diagrams (isosurface value of 0.05 a.u) for the near degenerate HOMOs and LUMOs that result for AxBDY and IAxBDY, due to their dimer structures. The diagrams also show the major transitions associated with the band maxima in the visible region.

Figure 4.2.3: The predicted frontier π-MO energies for BDY1-3, IBDY1-3, AxBDY and IAxBDY. The HOMO and LUMO levels are indicated in bold (primary axis) and the HOMO–LUMO gap values are highlighted with red triangles (secondary axis).

Figure 5.2: TEM images depicting oleate@UCNP samples A-C and their subsequent silica coating (D-F) each with the corresponding average diameter.

Figure 5.3.1: Powder X-ray diffraction pattern for sample A showing oleate and silica capping.

Figure 5.3.2: Powder X-ray diffraction pattern for sample B showing oleate and silica capping.

Figure 5.3.2: Powder X-ray diffraction pattern for sample C showing oleate and silica capping.

Figure 5.3.3: Emission profile of UCNPs sample A with an oleate cap (cyclohexane, top) and the silica coating (EtOH, bottom) after excitation at 972 nm.

Figure 5.3.4: Emission profile of UCNPs sample B with an oleate cap (cyclohexane, top) and the silica coating (EtOH, bottom) after excitation at 972 nm.

Figure 5.3.5: Emission profile of UCNPs sample C with an oleate cap (cyclohexane, top) and the silica coating (EtOH, bottom) after excitation at 972 nm.

Figure 5.3.6: [top] An overlay spectrum between Si@UCNPs emission spectrum (red, EtOH) against the absorption of IBDY3 (blue, EtOH), secondary axis. [bottom] Spectrum showing the prewashed solution for attempted conjugation between Si@UCNPs with IBDY3, Scheme 5.1.

Figure 5.3.7: The observed decrease in the Si@UCNP sample Cs peak with increasing IBDY3 concentration (EtOH). The inset shows intensity as a function of concentration.

CHAPTER ONE

Introduction

1. Introduction

The initial report of singlet oxygen ($^1O_2$) formation in the 1924 paper by Khan and Kasha has inspired research in physics, biochemistry and chemistry with applications being most prevalent, but not limited to, the life sciences. This energetically rich form of oxygen can be produced through various processes including exothermic chemical reactions and molecular photosensitization, and can be performed pharmaceutically or even in enzyme catalyzed systems[1]. The method of photosensitization is of particular importance, since it utilizes specific dye molecules for light absorption known as the photosensitizer (PS). The most important requirement for these sensitizer molecules is efficient transfer of energy from the singlet state (S_1) to the triplet state (T_1) followed by $^1O_2$ generation from the ground state of molecular dioxygen. The higher energy of this more reactive species is what has inspired the research interest since it may cause, in the case of biological applications, cell necrosis or damage to the surrounding tissue. This has paved the way towards treatments such photodynamic therapy (PDT) and photodynamic anti-microbial chemotherapy (PACT). Sensitizers used in PDT can be tailored with specific functional groups targeted at, for example, cancer cells. When biological samples are considered, the stimulating radiation is usually in the near infrared (NIR) region where biological autofluorescence is not encountered. This will be expanded further in Sections 1.1.3 and 1.2.3. Other areas that exploit $^1O_2$ generation include the treatment of wastewater, blood sterilization and targeted DNA damage[2,3].

The chemical processes that take place for $^1O_2$ generation though photosensitization have already been well documented[4]. Current research tends to focus on enhancing the effectiveness of the PS through greater specificity, functionality and response range to the target molecule/compound.

These areas have been substantially developed with the emergence of novel materials that are suitable for applications that require $^1O_2$ generation, for example in the growing field of nanotechnology, and in advances in synthetic procedures for modifying light absorbing compounds. The study described in this thesis focusses on the synthesis and properties of the versatile 4,4-difluoro-4-boro-3a,4a-diaza-*s*-indacene (BODIPY) class of dyes, and the rational modification of their photophysical properties. A set of BODIPY dyes was synthesized with various forms of functionality, including halogenation for $^1O_2$ generation, and their photophysical properties were characterized. A study was also conducted on the interaction between an iodinated BODIPY and upconversion nanoparticles (UCNPs), which had been modified for water dispersibility. This created a donor acceptor system where NIR radiation could be used to stimulate the UCNPs and its emission would be absorbed by an iodinated BODIPY. This interaction was studied for the purposes of $^1O_2$ generation.

The focus throughout is on how incident photons interact with the synthesized compounds and how their optical and photophysical properties can be refined and tailored towards specific applications.

1.1. Origins of Luminescence

The absorption of a photon may cause an excitation from the electronic ground state, S_0, to an electronic excited state, S_n, if the energy of the incident photon matches the energy gap between particular states ($S_0 \rightarrow S_n$). Each of these electronic states possess a number of closely lying vibrational levels that can also be accessed[5]. The electronic excited states are energetically unstable and, broadly speaking, there are three main pathways back to the ground state:

1. *Radiative processes*: Electronic relaxation results in the emission of a photon from either of the lowest lying electronic states. The emitted light can be used to provide information regarding molecular conformation or purity since the properties are characteristic for a particular compound. Two types of emissive radiative relaxation processes can be distinguished; fluorescence and phosphorescence, which are discussed in detail in Section 1.1.1[5].
2. *Nonradiative processes*: nonradiative de-excitation has no accompanying photonic emission with energy loss from excited levels being transferred via relaxation to other closely lying energy levels or by removal of this energy through collisions with solvent molecules[5].
3. *Quenching effects*: Quenching refers to the energy transfer from one molecule to another resulting from their collision. These effects occur predominantly in solution where molecular motion plays a more significant role.

These photophysical processes give rise to changes in the electronic states only and as such are markedly different from photochemical processes, where a reaction or molecular rearrangement takes place.

1.1.1. Fluorescence and phosphorescence

The light emitting processes of fluorescence and phosphorescence are distinguished by the nature of their excited state. If there is no change in spin state after photoexcitation, ground singlet to excited singlet ($S_0 \rightarrow S_1$), then fluorescence is observed, typically in the time frame of $< 10^{-8}$ s since the ground and excited electrons are in their original spin orientations[6,7]. Each electronic level is

comprised of closely stacked vibrational levels (Franck-Condon principle, **Figure 1.2**) which normally undergo rapid relaxation to their lowest respective electronic states through nonradiative internal conversions, $S_2 \rightarrow S_1$ or $S_1 \rightarrow S_0$, represented in the Jablonski diagram, **Figure 1.1**[8,9]. The emission of a photon via fluorescence usually occurs from the S_1 electronic level according to Kasha's Rule, since a vibrationally excited molecule or molecule in a higher excited state has a much shorter lifetime, in the order of 10^{-12} s, than the fluorescence process[10]. This affect can be attributed to the vibrational levels of the electronic wavefunction which experience a much larger overlap due to their close proximity[11]. However, if there is a change in multiplicity via intersystem crossing (ISC) from the S_1 to the T_1 state prior to electronic relaxation a much slower descent to the S_0 is observed, with the lifetime varying between 10^{-4} to 10 s. This process is referred to as phosphorescence[11,12].

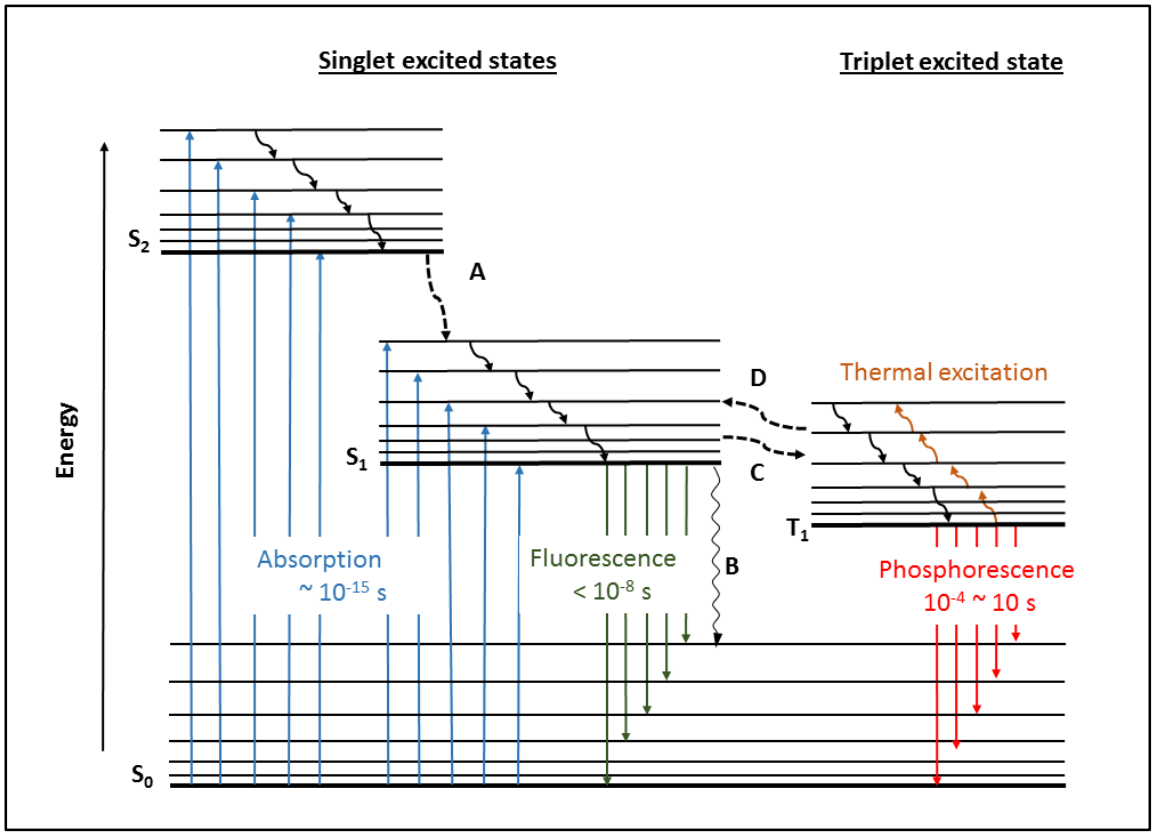

Figure 1.1: A Jablonski diagram showing the major transitions associated with the luminescence processes. Electronic excitation to either the second (S_2) or first (S_1) excited states with their respective vibronic energy levels is indicated (blue). The internal conversion, process A, shows the transition from $S_2 \rightarrow S_1$ and subsequent vibronic relaxations through internal conversions to its lowest energy level which, according to Kasha's Rule[13], is the origin of the fluorescence process. Energy loss during relaxation from an electronic level can also take place without the emission of a photon, this is referred to as nonradiative decay and is shown by process (B). Here, energy is lost as heat through phonon interactions or through internal conversion to the S_0 state. Intersystem crossing (C) involves a change in spin of an electron so that a triplet (T_1) state is formed. The T_1 state is the origin of the slower

phosphorescence process. The final process (D) is termed as delayed fluorescence or E-type fluorescence.

According to the Wigner rule for conservation of electronic spin ISC, process C in **Figure 1.1**, is a forbidden transition since spin multiplicity must be conserved for any given excitation. However this rule can be lifted with the introduction of a heavy atom thereby enhancing the spin-orbit coupling of the molecule[14,15]. That is to say; if the coupling between orbital motion and the intrinsic spin within the system is sufficiently strong the distinction between states of different multiplicity, S_1 and T_1, becomes less fixed and the rate of ISC becomes shorter than that of fluorescence or nonradiative decay[16]. The strength of this interaction is dependent on a number of factors such as the size of the spin, the orbital angular momentum vectors *s* and *l* and most importantly the spin-orbit coupling constant. This is where the heavy atom effect gets its name as this constant depends, among other things on the 4^{th} power of the atomic number, Z[11,17]. The transfer from the singlet to the triplet manifold is analogous to an intramolecular charge transfer (ISC) i.e. between two sets of orbitals within a single molecule[6]. The electronic T_1 level indicated in **Figure 1.1** is slightly lower in energy compared to the S_1 level. This is because the overall spin angular momentum (S) of the electrons are now opposed and the multiplicity, given by Hund's rule $2S + 1$, is raised[18].

A molecule may also exhibit what is known as delayed or E-type fluorescence, **Figure 1.1 D**. This has two basic mechanisms: the first is kinetically driven with the collision of a second triplet state molecule generating a singlet excited state from the combined energies. Fluorescence from this point depends on the accumulation of molecules in the triplet state and thus appears delayed, this

type of behaviour is favoured in an upconversion process termed triplet – triplet annihilation (TTA)[11]. The second mechanism is temperature controlled, with the alternative name thermally activated reverse ISC, and occurs from the vibrationally excited levels of the T_1 state[19]. The main point of consideration is the energy splitting between the S_1 and T_1 states. If this splitting is small the energetic requirements are minimal. This means that the process is therefore favoured at lower temperatures and thermal excitation allows for reverse ISC[20].

1.1.2. Emission characteristics

1.1.2.1. Stokes and anti-Stokes shifts

There are a number of aspects of the fluorescence process that are key to understanding the research described in this thesis. The first of these is the Stokes shift, which refers to the slight lowering in the emission energy relative to the corresponding band in the excitation spectrum. This is caused by the small vibrational relaxations during the internal conversion to the lowest electronic level of the S_1 electronic state as can be seen with the Morse potentials of **Figure 1.2**[21]. These vibrational levels arise from the small change in the molecular structure resulting from the electronic ground state no longer containing the same electron configuration upon photoexcitation. Particularly in the context of photosensitization, it can also be assumed that since the analysis is carried out in solution, some vibrational energy is lost through collisions with solvent molecules when it is converted to translational motion, and this also enhances the rate of internal conversion to the S_1 electronic state[22,23].

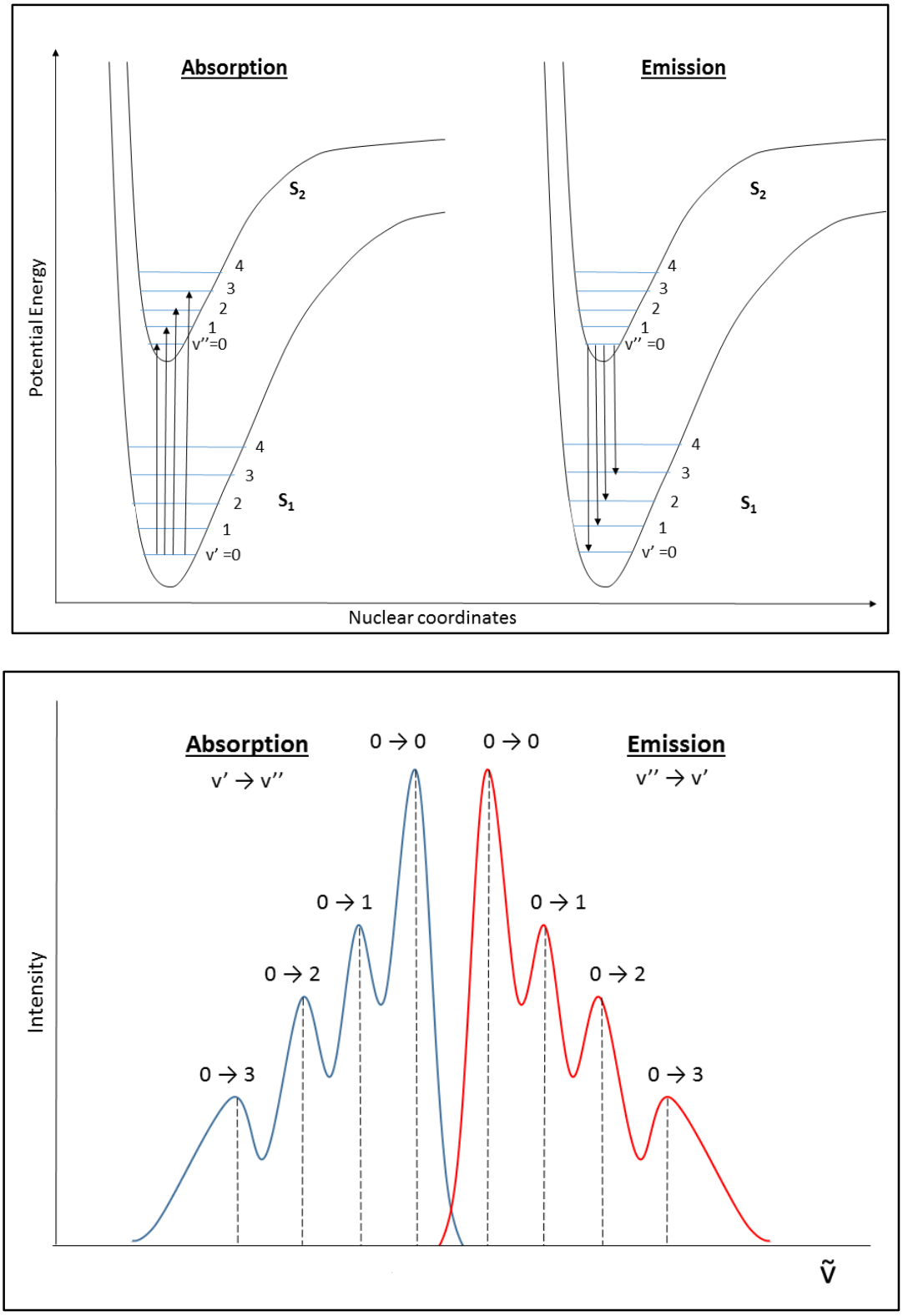

Figure 1.2: A Morse potential diagram (top) displaying the excitation profile from the electronic ground state (v' = 0) to the individual excited vibrational levels (v'' = 1

to 4) as well as the electronically excited state (v'' = 0) to the ground vibrational levels (v' = 1 to 4). Below is the corresponding fluorescence spectrum for this absorption (blue line) and emission (emission), characteristically mirror images of each other.

As can be inferred, an anti-Stokes process is precisely the opposite, with a resulting gain in energy in the emitted photon. The occurrence of anti-Stokes emission is unusual as the energetic laws and electronic requirements limit its feasability[24]. Nanoparticles that can display anti-Stokes emission due to their unique electronic arrangement, termed upconversion nanoparticles (UCNPs), are studied extensively in this work and a detailed explanation of their properties is provided in **Section 1.3.** In this study, specific lanthanide ions possessing sequential, metastable energy levels allow for the population of higher energy electronic states and, upon their relaxation, release photons with a shorter wavelength and therefore higher energy[25].

1.1.2.2. The fluorescence quantum yield and lifetime

Fluorophores possessing high fluorescence intensity and long fluorescence lifetimes are sought after in the design of molecular probes and sensors[26]. As discussed above, the fluorescence of a molecule usually occurs from the lowest electronic state, $S_1 \rightarrow S_0$, according to Kashas' rule, **Figure 1.2**. The efficiency of this process is described by the fluorescence quantum (ϕ_F) yield value. These values are generally derived using a comparative method which requires a standard sample with a known ϕ_F yield value. Here, the number of emitted photons is related to the number of absorbed photons and compared to the values obtained for the standard, **Equation 1.1**[27]. This provides a measure of the efficiency of the fluorescence process.

$$\phi_F = \phi_F^{std} \frac{F.A_{std}n^2}{F_{std}.A.n_{std}^2} \quad (1.1)$$

F and F_{std} are the integral of the area under the fluorescence emission curve of the sample and standard, respectively. A and A_{std} represent the absorbance of the sample and standard at the wavelength of excitation, respectively. n^2 and n^2_{std} are, respectively, the refractive indices for the sample and standard, if applicable, and ϕ_F^{std} is the known fluorescence quantum yield value for the standard.

The comparative method[28] can only be used if the optical parameters are held constant. This ensures that the energy received by both the sample and standard is identical, so an accurate value can be determined. A ϕ_F value of 1.0 indicates that there is only radiative relaxation taking place as all absorbed quanta of light result in fluorescence emission. Compounds that are able to generate near unity ϕ_F values display an almost linear correlation between fluorescence intensity and absorption intensity, due to their resistance towards the quenching effects of self-aggregation, and are often used as standards for comparison during measurements. For example, Rhodamine 101 in methanol has a ϕ_F value of 1.0; 9, 10-diphenyl anthracene in cyclohexane has a ϕ_F value of 0.90 and Rhodamine 6G in methanol has a value of 0.86[27,29].

The fluorescence lifetime (τ_F) is a measure of the average time an electron spends in the S_1 electronic state before returning to the ground state via the emission of a photon. The complexity involved in separating the fluorescence decay from all other decay processes is greatly simplified by selecting and analyzing only the S_1 radiative band. Data is obtained by deconvoluting an experimental decay profile using the time correlated single photon counting (TCSPC) instrument.

The τ_F value can also provide information on quenching effects, band polarization and Forster Resonance Energy Transfer (FRET).

In the context of BODIPY dyes, their excited states are not particularly long lived but they are well-known more for their efficiency of absorption and fluorescence intensity. The measurements of τ_F values for the BODIPY dyes synthesized in this research were found to lie in the nanosecond (ns) region. A significantly longer τ_F value is observed for UCNPs with values in the microsecond (µs) time frame. This is essential for the upconversion process to occur[25] and are discussed in greater detail in Sections 3.1 and 5.1.

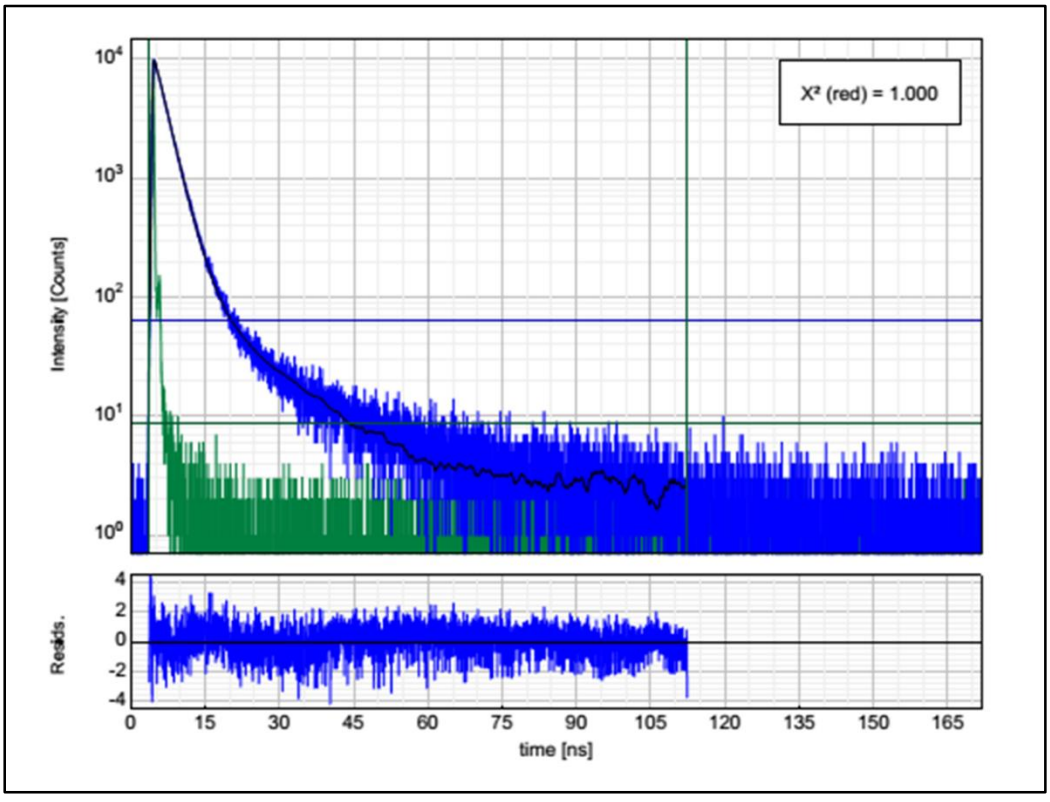

Figure 1.3: Typical data obtained during ϕ_F measurements using the TCSPC method at a 165 ns pulse length with residual counts shown.

1.1.3. Singlet oxygen generation

Singlet oxygen forms the foundation for research fields such as PDT and PACT due to its ability to cause cell necrosis in the surrounding tissue[3]. The method of photosensitization uses a combination of a PS, light (*hv*) and ground state molecular dioxygen ($^3O_2$). The main criteria in the selection of a BODIPY as a PS is sufficient T_1 state formation after the incorporation of heavy atoms. When a PS is excited to its S_1 state and undergoes ISC to its T_1 state, an energy transfer to the molecular dioxygen T_1 state occurs through a type two mechanism, Scheme 1.1. In this case, the $S_0 \rightarrow T_1$ band gap of the PS should be greater than 0.98 eV, the energy gap between the singlet excited and triplet ground state, resulting in an efficient energy transfer between the T_1 state of the PS and the dioxygen[30].

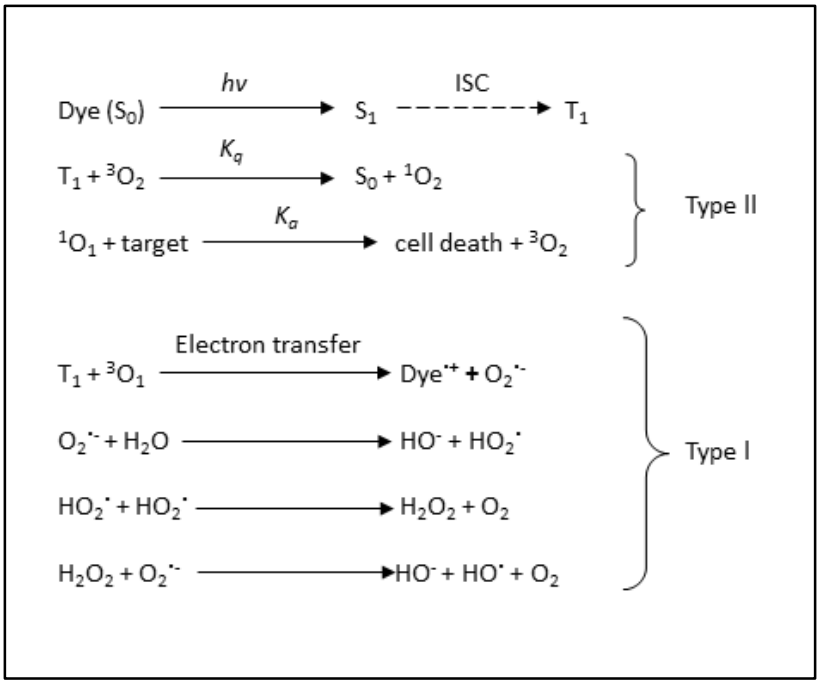

Scheme 1.1: Triplet state interaction molecular oxygen for singlet oxygen production (Type II) or radical formation (Type I).

The type one mechanism on the other hand, describes the interaction of the T_1 state with ground state triplet dioxygen, usually resulting in the generation of toxic peroxides and superoxides. Singlet oxygen quantum yields (ϕ_Δ) are derived using a comparative method[30] by monitoring the decrease in a singlet oxygen quencher with respect to a known standard, **Equation 1.3**. The singlet oxygen scavengers used in this context include anthracene-9,10–bis–ethylmalonate (ADMA) and 1,3-diphenylisobenzofuran (DPBF)[30,31].

$$\phi_\Delta = \phi_\Delta^{std} \frac{WI_{abs}^{std}}{W^{std}I_{abs}} \quad (1.3)$$

ϕ_Δ^{std} is the singlet oxygen quantum yield of the standard and ϕ_Δ is that of the sample. W^{std} and W are the photobleaching rates of the scavenger molecule and sample, respectively. I_{abs}^{std} and I_{abs} are, respectively, the light absorption intensity for the standard and sample. There are alternative methods for determining the singlet oxygen quantum yields. The above method is the most practical in the context of this thesis.

1.2. BODIPY dyes

1.2.1. Structure of the BODIPY core

The serendipitous discovery in 1968 of BODIPY dyes by Alfred Triebs and Franz-Heinrich Kreuzer initially led to only limited interest from other researchers. In recent years, however, BODIPY chemistry has gained momentum due to their use in fluorescent based sensors[32,33]. BODIPYs are often referred to as structural analogues of porphyrins, since they form roughly half of the structure of a typical tetraphenylporphyrin (TPP), Figure 1.2.

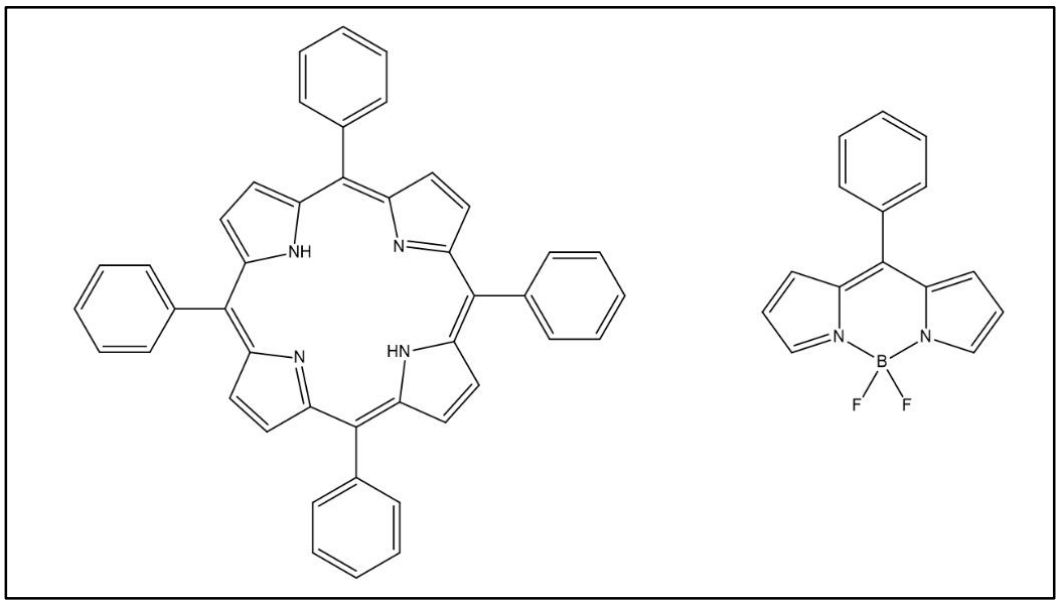

Figure 1.4: The typical structure of a tetraphenylporphyrin (left) showing the structural similarity to a meso-phenyl BODIPY (right). The TPP example above is shown in its metal free form which can be chelated with the addition of a divalent metal ion. The BODIPY on the other hand is coordinated by a BF_2 moiety.

BODIPYs have favourable spectroscopic properties that offer a number of advantages over other fluorescent based dyes[34]. BODIPYs display strong absorption in the visible region with high molar absorption coefficients (40000 to 80000 $M^{-1}cm^{-1}$), high fluorescence quantum yields with lifetimes in the ns range, and relatively small Stokes shifts[35,36]. Additionally, BODIPYs possess chemical robustness towards environmental pH and thermal fluctuations with negligible sensitivity to solvent effects. These enhanced properties make them suitable for use as a PS[36,37] for PDT or as light harvesting compounds in a range of applications including TTA upconversion and solar cell technology. Their main drawbacks, in the context of PDT is that although they are highly soluble in a variety of organic solvents only a handful have been adapted for water solubility, and their spectral bands lie outside the therapeutic window, between 600–1000 nm[38]. These can be addressed with the addition of suitable functional groups to specific sites on the BODIPY core[39,40].

The numbering system of the parent unsubstituted BODIPY structure is shown in **Figure 1.3,** along with the more traditional nomenclature[41,42]. The complexation of the dipyrromethene ligand with a borondifluoride (BF_2) moiety results in a rigid planar structure through the N–B–N linkage, which enables the π-electrons to be delocalized with the positive charge on the nitrogen stabilized

between the two resonant structures[42]. This completes the π-conjugation through the carbon nitrogen backbone with the adjacent pyrrole moieties and meso-carbon.

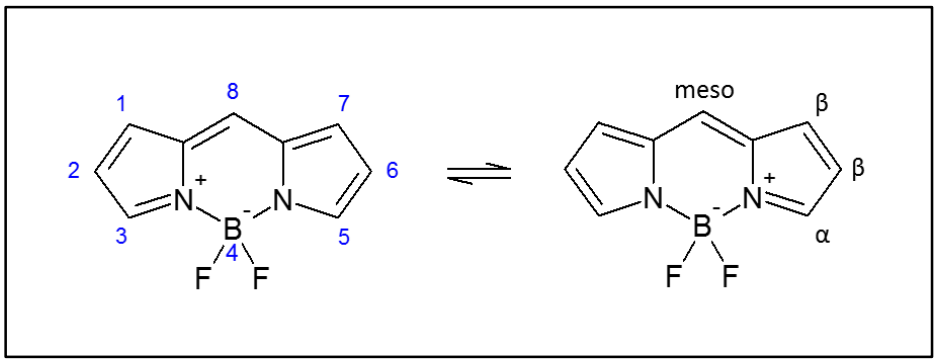

Figure 1.5: Typical resonance structures of the BODIPY chromophore showing the IUPAC numbering system (1–8) for the possible functionalization sites. Also indicated is the common nomenclature that is used widely in literature [41,42].

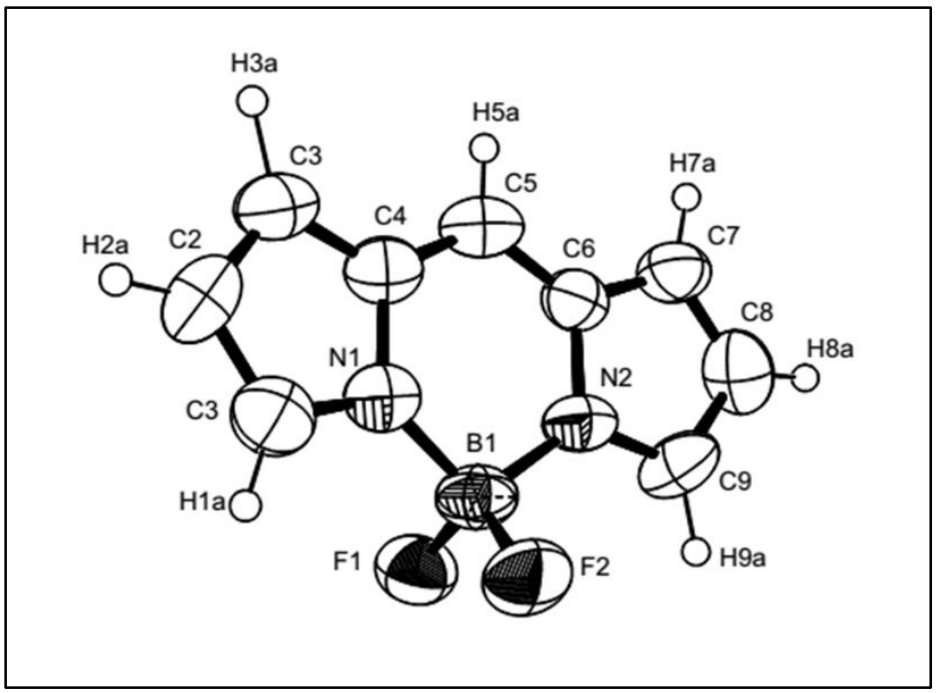

Figure 1.6: A diagram of the first unsubstituted BODIPY crystal structure obtained by Tran et al. The atoms are shown with 50% probability displacement ellipsoids[43].

Inspection of the crystal structure of the unsubstituted BODIPY chromophore[43], **Figure 1.4**, aids in the elucidation of the unconventional valency observed at the BN_2F_2 centre. Bond angles between the N_1–B_1–N_2 and the F_1–B_1–F_2 are consistent with a tetrahedral (sp^3) configuration which is adopted when an electron pair is accepted from a Lewis base thus satisfying the octet rule. This configuration means that the orthogonal fluoride atoms play no part in the extension of the π-conjugated system but still influence the electronic distribution around the BODIPY core, due to high electronegativity[43,44].

The BODIPY structure does not obey Hückel's 4n+2 rule for aromaticity due to the absence of a cyclic macrocycle, so it can be referred to it as having 'pseudo' aromatic properties[45] since it exhibits aromatic characteristics, due to the rigidity of the chromphore.

There were numerous unsuccessful attempts to synthesize the parent unsubstituted BODIPY structure due to the relative favourability of the unsubstituted dipyrromethanes towards side reactions and polymerization, before the first successful synthesis was reported as recently as 2009 by Tran et al.[43] The absorption spectrum of the parent unsubstituted BODIPY dye is shown in **Figure 1.7**. The reaction was carried out at –78°C under anhydrous conditions[43]. Further difficulties arise because the unsubstituted pyrrole is prone to further electrophilic attack, particularly at the 3 and 5-positions of the BODIPY core, **Figure 1.5**, and can further cyclize into a porphyrin[46,47].

In order to avoid this problem and increase the overall yields, BODIPYs are typically synthesized with a methyl-substituted pyrrole or 2,4-dimethylpyrrole, since this blocks further electrophilic polymerization at the pyrrole rings. A range of BODIPY dyes with this type of conformation have already been synthesized and, since they can be produced in near quantitative yields, have been made commercially available[48].

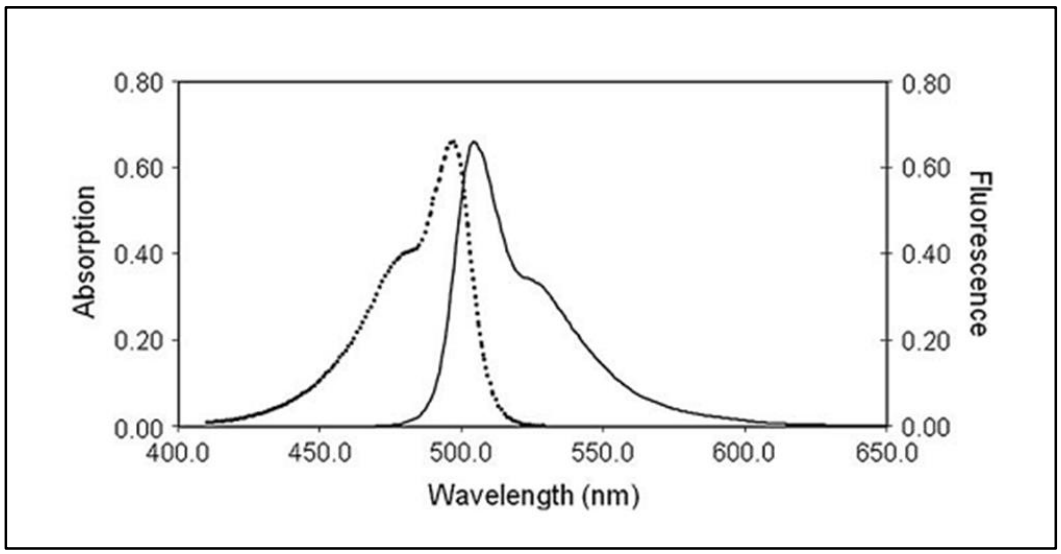

Figure 1.7: The excitation (dotted) and emission (solid) spectra of an unsubstituted BODIPY dye run in MeOH[43].

The BODIPY chromophore, while not formally aromatic, displays aromatic characteristics. An intense band is observed at ca. 500 nm, Figure 1.7. This can be attributed to the electronic transition from the $S_0 \rightarrow S_1$ ($\pi \rightarrow \pi^*$) electronic transition, while a characteristic shoulder at lower energy can be assigned as a vibrational transition (0-1)[49]. A less intense and broader band envelope arising from the $S_0 \rightarrow S_2$ ($\pi \rightarrow \pi^*$) transition, also appears at ca. 350 nm. The fluorescence emission spectrum that is obtained upon excitation into either the S_1 or S_2 states exhibits a small

Stokes shift between 10-15 nm. Mirror symmetry between the emission and excitation spectrum is usually, but not always, maintained irrespective of the extent of modifications made to the BODIPY core[50].

The high electronegativity of the fluorine atoms at the 4-position induces a slight polarization which results in a set of electronically diverse sites on the pyrrolic rings providing scope for a wide range of post synthetic functionalizations. These include electrophilic substitution at the 2, 6-position, nucleophilic substitutions at the 3, 4, 5 or 7-position, condensation reactions or Suzuki and Sonogashira coupling reactions at the 2, 3, 5 and 6-positions[51,52]. The results of these modifications are two-fold in many circumstances. Firstly, they provide the necessary scaffold for further linking or bio conjugation, and secondly they enable the fine tuning of the absorption and fluorescent properties. Sonogashira coupling reactions will be the main focus of this thesis, and can occur at any of the available positions with the exception of direct addition at the 8-position.

1.2.2. Synthesis and spectral properties

The approaches used during the synthesis of BODIPY dyes have varied little since their initial characterization. Synthetic yields can be significantly improved with stringent control over the reaction conditions and reagent preparation[49]. Herein, two alternative routes have been used depending on the functionality of the starting materials. **Figure 1.6** shows the pathways used extensively in this study following the traditional one pot method, **A**, and a water precipitation method, **B**, as used in reaction **Scheme 2.3.2** for the synthesis of the pyrro-ethynyl BODIPY[53,54].

The first approach uses anhydrous DCM containing the pyrrole or pyrrole derivative together with an aromatic aldehyde. An acid catalyst is then added, typically trifluoroacetic acid (TFA), which

affords the dipyrromethane intermediate, **1.1**. Conversion to a dipyrromethene, **1.2**, is achieved with a highly reactive oxidizing agent such as *p*-chloranil or DDQ (2,3-dichloro-5,6-dicyano-*p*-benzoquinone). Yields are significantly increased by lowering the temperature to 0 °C, since this prevents of side reactions[49]. Basic conditions are created with the addition of a tertiary amine followed by complexation with boron trifluoride diethyletherate ($BF_3 \cdot Et_2O$). When unsubstituted pyrrole or impure pyrrole derivatives are used the formation of tripyrromethanes, or even complete cyclization to form a porphyrin, occurred after the addition of the acid catalyst. Careful monitoring of the catalyst reaction time with TLC should always be carried out to prevent unnecessary polymerization[55,56].

This problem was addressed by using a green method pioneered by Rohand et al.[53] and adapted for the synthesis of porphyrins and porphyrin derivatives whereby the starting dipyrromethanes advantageously precipitates out of solution. The TFA catalyst is exchanged for hydrochloric acid (HCl) which is prepared in aqueous media at 0.18 M. The pyrrole or pyrrole derivative is then added followed by the aromatic aldehyde at 0.15 M. The dipyrromethanes form at the interface between the organic micelles and inorganic layers catalyzed by the HCl. The precipitate is then filtered and washed with petroleum ether (PET) and water. The remaining steps, **1.2** to **1.3**, are analogous to the classical method described above.

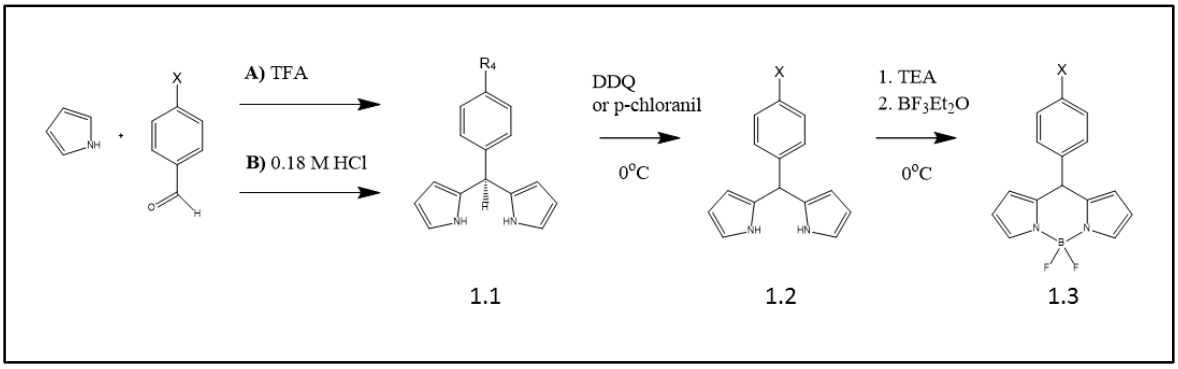

Scheme 1.1: The general scheme outlining two synthetic pathways towards BODIPY dyes. Pathway A follows the one pot reaction utilizing TFA as the oxidizing agent. The second pathway, B, involves the use of aqueous HCl (0.18 M) with the resulting dipyrromethane 1.1 precipitating out of solution. Following purification the continuing steps and conditions are identical.

Pre and post-synthetic modifications are facile, since the starting pyrrole can be substituted at any of the positons leaving the α carbon available for pyrrole-methine-pyrrole formation. This is also true for the 8-position which can be adjusted by varying the starting aromatic aldehyde. BODIPYs synthesized using these methods can bear multiple functionality such as ester, hydroxyl and amines groups and halogen atoms, providing scope for a wide range of synthetic diversity.

Figure 1.6 provides a general indication of how the position of substitution and the symmetry of the complex affect the BODIPY spectral properties. There is a slight hypsochromic shift in the maxima of the main spectral bands of asymmetric BODIPYs 2 and 5 with respect to the maxima of their symmetric equivalents, 3 and 6, which are slightly more red shifted.

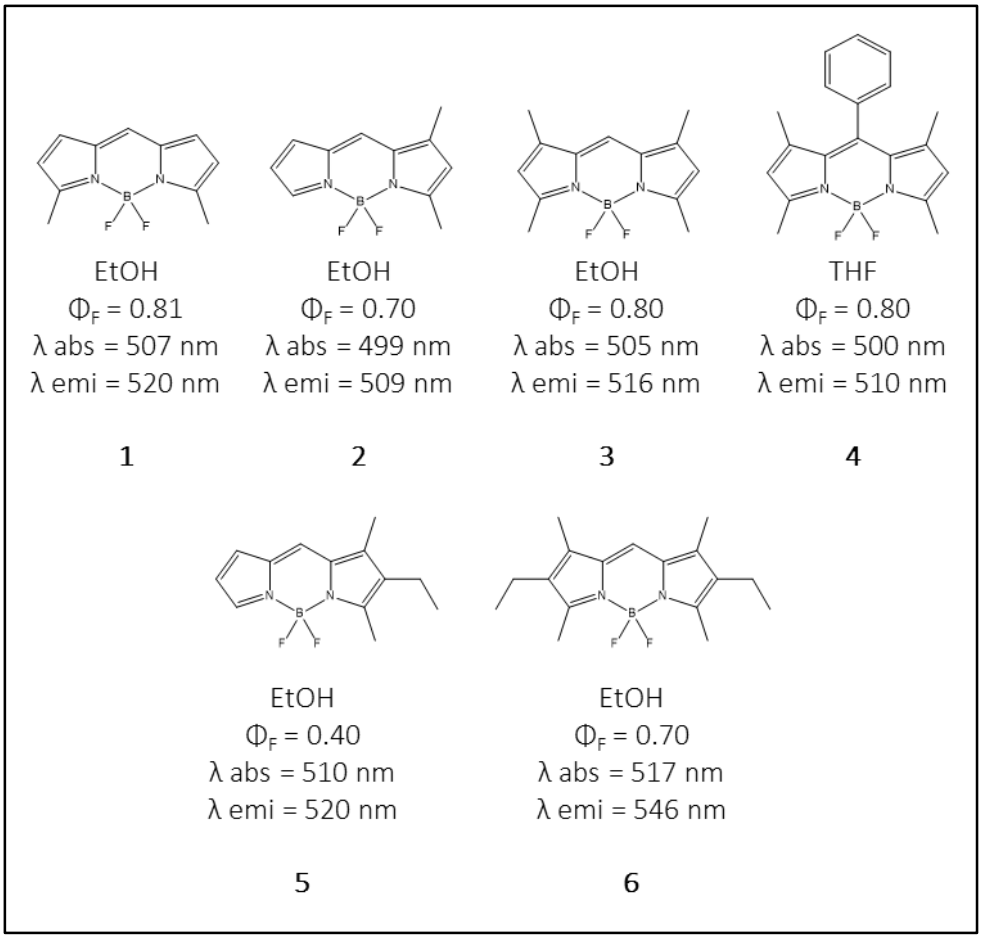

Figure 1.8: The absorption (abs) and emission (em) wavelengths of the main spectral bands for various BODIPY dyes and how they relate to asymmetric and symmetric substitution around the BODIPY core[57,58].

BODIPYs 1 and 4 do not follow this general trend. Apart from solvent effects, the absorption and emission properties are dependent on the electron distribution at the sites of substitution given the electron donating or withdrawing nature of the attached group. Various structural modifications can be made since the chemically robust core remains inert during synthesis[59,60].

1.2.3. Strategies for modification

The markedly differing distribution of electron density at specific sites around the BODIPY core creates the possibility for a wide range of different structural modification reactions both pre- and post-BODIPY synthesis depending on the position and type of modification that is involved. Furthermore, the robustness of the BODIPY core enables the attachment of linkers, biomolecules, acceptors and receptors, organic conjugates, or other methods of functionalization without molecular degradation[46,61]. There are a number of different strategies that are typically employed for modifying specific sites on the BODIPY core. Since these are numerous[46] and have been extensively reviewed elsewhere, only the two most relevant types shall be discussed here in detail: meso-aromatic substitution and modifications around the core structure.

1.2.3.1. A) Meso-aromatic substitution

As mentioned above, facile substitution at the meso-position is, in part, what accounts for the wide range of BODPIY structures that have been reported to date. The attachment of aryl groups at this position has a minimal effect on the absorption and emission band maxima when compounds have a methyl or any other reasonably bulky substituent at the 1, 7-positions, since this causes the meso-group to lie out of plane relative to the BODIPY core. This orthogonal arrangement between the phenyl ring and the BODIPY plane minimizes energy loss via intramolecular rotation[62]. In contrast, when the meso-phenyl group is freely rotating, there is an observed decrease in their fluorescence quantum yields due to non-radiative decay, while the absorption maxima of the compounds are largely unaffected[59,63]. Figure 1.9 summarizes these effects. With regards to BODIPY **1.4**, the presence of electron donating/withdrawing groups at the

meso-position does not significantly alter the π-conjugation system of the core, since the meso-phenyl groups lie out of the dipyrromethene plane. In contrast, the meso-aryl group of BODIPY **1.5** can freely rotate. Upon photoexcitation, the energy is transferred and effectively dissipated by the rotational motion and emission of a photon is not observed[62]. The significance of this will be discussed in greater detail in **Section 3.1.2.**

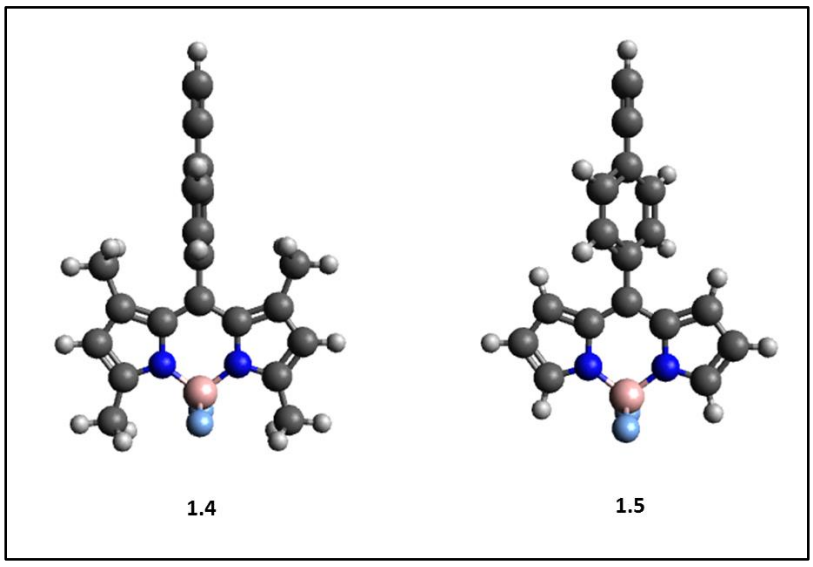

Figure 1.9: Diagram showing the sterically hindered meso-phenyl group (1.4) with a 1, 3, 5, 7-tetramethyl BODIPY core and the freely rotating ring analogue with an unsubstituted core (1.5).

The substituent at the meso-position can be tailored towards specific applications. Large areas of BODIPY chemistry involve the fine tuning of the BODIPY structure to form sensor molecules for the detection of metal ions, hazardous gases, biological labelling or changes in pH. These types of sensors are usually based on the relationship between the meso-aryl functional groups and the

BODIPY core. The detection mechanism for sensor applications tends to be related to ISC associated with an effect referred to as photoinduced electron transfer (PeT)[64].

1.2.3.2. B) Photoinduced electron transfer (PeT)

The driving force for the PeT process is an energy difference between donor and acceptor portions of the molecule[65]. This is particularly notable in the S_1 excited state of the BODIPY, in which the 8-position carbon carries the largest amount of charge density. Figure 1.8 shows one of the many examples taking advantage of this phenomenon for the creation of a Zn^{2+} sensor[66]. Groups carrying a lone pair of electrons, such as this, form the donor and can donate electron density to the electron vacancy created after photo-excitation of the BODIPY core, which forms the acceptor[66].

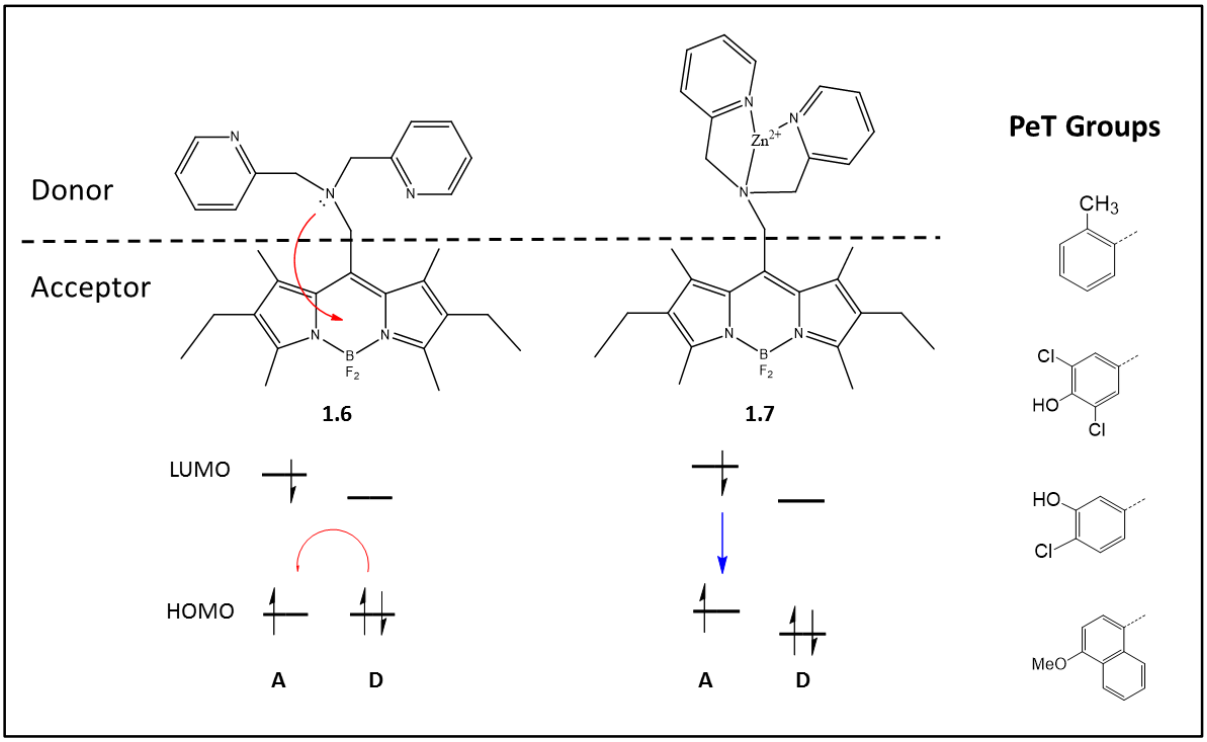

Figure 1.10: A Zn^{2+} ion sensor based on intramolecular electron transfer from donor (D) to acceptor (A). Compounds bearing suitable functionality, shown as an inset on the right, are known comopunds and will favourably undergo the PeT process[66,67].

The electron transfer has a rate of < 1 ps which is significantly lower than the BODIPY fluorescence lifetime of between 1–10 ns[36]. This means that the fluorescence is effectively quenched so that the response of the BODIPY is switched "off". In the presence of a target analyte, however, the meso-position lone pair will chelate to the analyte effectively lowering the energy gradient preventing the transfer of electrons, **Figure 1.7**, causing the fluorescence response to switch "on"[68].

1.2.3.3. Core modification strategies and the extension of π conjugation

While the incorporation of different meso-groups results in a largely unchanged emission spectrum when the ring is rotated out of plane of the BODIPY core, modifications on the core tend to have a much more significant effect on the optical properties. The most commonly used 2, 4-dimethylpyrrole results in a BODIPY dye with methyl carbons at the 1, 3, 5 and 7-positions. In a similar manner, the use of 2-methylpyrrole results in the BODIPY core with methyls at the 3 and 5-positions. The methyl groups have a strong nucleophilic character and can undergo styrylation by means of a Knoevenagel condensation reaction upon the addition of an aromatic aldehyde[69]. This approach is commonly used to form BODIPY dyes with extended π-conjugation systems due to the high yields they afford and the highly controlled formation of products that can be achieved through careful modulation of the molar ratios, reaction times and temperature. The synthesis and characterization of tetra-styryled BODIPYs using a 1, 3, 5, 7-tetramethyl BODIPY a starting platform have been reported by a number of research groups[69]. The electron density located around the BODIPY core causes the methyl groups attached to these positions to have strongly nucleophilic character with the 3, 5-positions being the most reactive towards Knoevenagel condensation[46,70]. Examples of mono-, di-, and tetra-styryl-BODIPYs are shown in **Figure 1.9** along with the changes in the absorption band maxima for each compound.

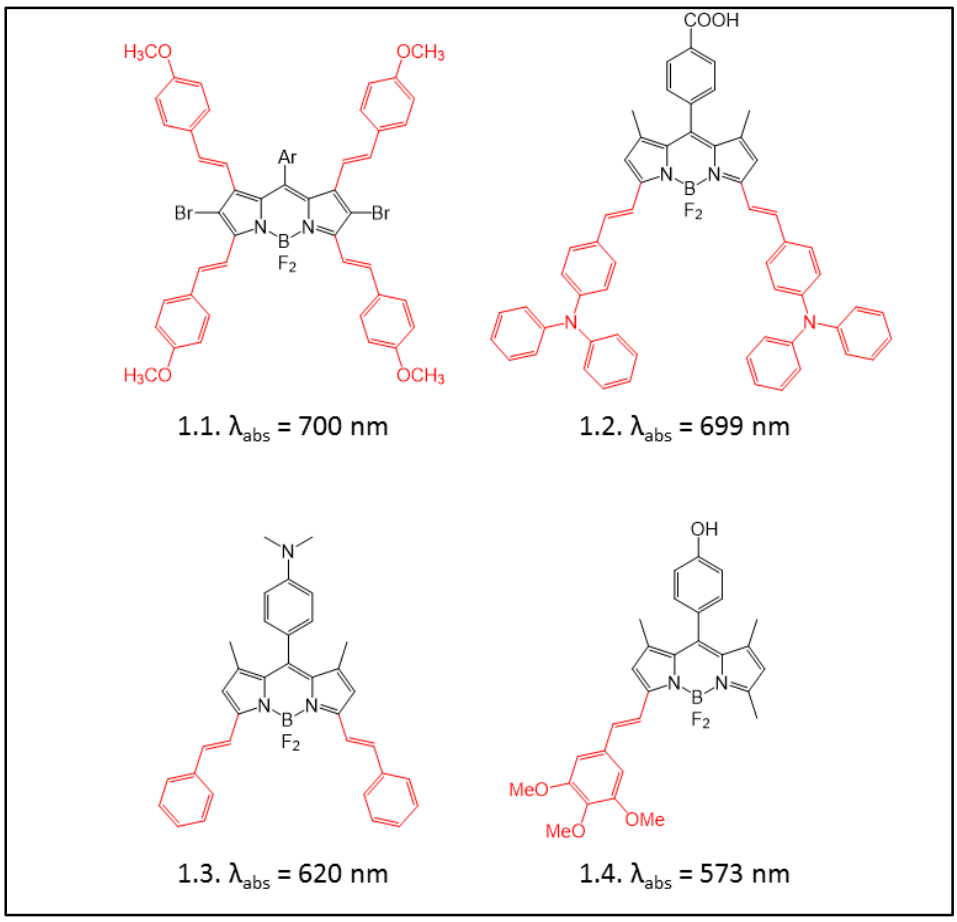

Figure 1.11: Styrylation of the BODIPY core and how it relates to the absorption maxima with respect to position, number and substituent. (1.1. [71], 1.2 [72], 1.3 [46], 1.4 [73])

Structural modifications that extend the π-conjugation at these positions result in larger bathochromic shifts (ca. 50 – 100 nm) than modification to form 2, 6-substituted compounds[74]. The electron donating properties of the styryl substituents is one of the most effective to obtain long wavelength absorbing dyes. Dyes of this nature can also be obtained through halogenation with an additional synthetic step. For example, the use of *N*-chlorosuccinimide (NCS) or *N*-iodosuccinimide (NIS) allows for the functionalization with chlorine or iodine atoms, respectively.

In order to obtain this functionality with, for example, chlorine atoms at the 3, 5-positions, NCS is added during synthesis at the point where the dipyrromethanes have formed. When chlorine or iodine atoms are used as a leaving group, various nucleophilic substitution reactions can be carried out which have enabled the design of molecular probes for sensor applications[75,76]. This approach makes use of the ISC effect which heavily influences both the absorption and emission spectra of the BODIPY[68,77,78].

Modifications at the 2, 6-positions will now be considered. These sites possess the most electron rich character when the electronic resonance structures are taken in to consideration, **Figure 1.10**[59]. Electrophilic substitution reactions such as halogenation, sulfonation, formylation and nitrations are therefore favoured[76,79,80]. An example of a halogenation reaction using iodine atoms showing the preferential substitution at the 2, 6-positions is described in detail in **Section 3.2**.

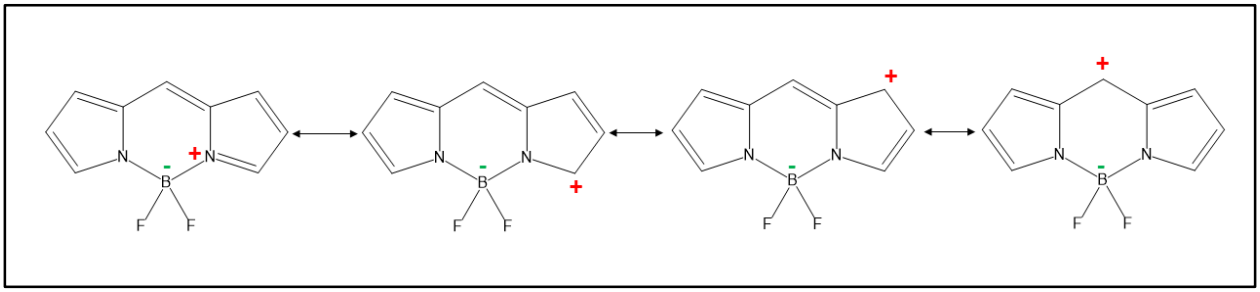

Figure 1.12: An unsubstituted BODIPY core displaying the resonant forms for delocalization of the positive charge. The 2, 6-positions possess a significant negative charge and as such has a more nucleophilic character[59].

The strong π-character at these positions usually results in a ca. 20–50 nm red shift of the main spectral band when a halogen atom is introduced. Iodinated or brominated BODIPYs are an important building block for Sonogashira, Suzuki and Heck coupling reactions[81]. There is also a marked decrease in the fluorescence quantum yield owing to the increased probability for ISC to the T_1 state due to the heavy atom effect[82].

Formyl groups can also be added by using the Vilsmeier-Haak reaction with yields as high as 80% due to the electron rich nature of these sites. It is noteworthy that the formation of a mono-formyl-BODIPY as opposed to the symmetrical 2, 6-diformyl is favoured[83]. This is because the required excess amount of Vilsmeier-Haak reagent forms an intermediate 2-mono-iminium which deactivates the 6-position and prevents further electrophilic attack. While the presence of these groups alter the spectroscopic properties significantly they can be used to further extend the π-system by using the Knoevenagel reaction.

It is important to emphasize that the typical examples of reactions provided in this section, which alter the chemical, spectroscopic and redox characteristics of BODIPYs provide only an introduction to the versatility that BODIPY dyes have to offer.

1.3. Nanotechnology

Nanoscience and nanotechnology is a rapidly growing field across disciplines combining the areas of chemistry, physics and engineering. This type of integration means that its impact has been far-reaching in commercial and industrial terms, and a number of technological and electronic advances have already been made.

The prefix 'nano' denotes particles within the nano domain at one billionth of metre in size. By comparison to the bulk states, nanoparticles have vastly different characteristics arising from the quantum confinement rule[84]. This applies when the dimensions of the particle are reduced to such an extent that they are smaller than the electrons' wavefunctions of the quantum states. Quantum confinement is generally grouped into three classes; quantum wells (spatially confined in one dimension), quantum wires (two-dimensionally confined) and quantum dots (confined in all dimensions)[85,86]. This quantization of electronic motion to discrete energy levels modifies the physical and chemical properties in such a way that they become size and shape dependent. A good example of such effects can be described in the context of quantum dots[84]. The band gap between the occupied and unoccupied energy levels of quantum dots becomes tunable when the particle size is smaller than the Bohr exciton radius[87]. An indication of their sizes can characteristically be estimated by their absorption wavelength.

A second consequence of size reduction in the context of nanoparticles is a dramatic increase in the surface to volume ratio[88]. In addition to the obvious increase in reactivity and sensitivity that results from a size decrease, some nanoparticles, such as indium nanostructures, have been found to possess variable melting points. Toxicity is another factor influenced by structural dimensions, and is particularly significant with gold nanoparticles[89]. Studies have shown that particle sizes smaller than 4 nm result in apoptosis while larger nanoparticles are found to be non-toxic. Interestingly, rod shaped nanoparticles with a 65 nm size display toxic effects[90]. The effects described provide only a fraction of the interesting properties nanoparticles possess. Others include superparamagetism, surface plasmon resonance and unique optical effects[91]. This

explains why nanotechnology has gained so much momentum in research terms. Among the multitude of nanoparticles currently being developed this thesis focuses on the study of UCNPs. The upconversion (UC) process refers to the absorption of long wavelength photons which are converted to a much shorter emitted wavelength of higher energy. This has profound implications for *in vivo* studies, since biological autofluorescence often interferes with that of the fluorophores lying outside the therapeutic window, 650–1000 nm[92]. Since its discovery by Auzel et al.[93] in the mid-1960's, research into UC has provided some remarkable advances such as infrared quantum counter detectors, temperature sensors and compact solid state lasers to name only a few[93,94]. Despite the potential for biological applications, research into UCNPs initially focused on bulk glass or crystalline materials and only in the last 15 years has there been a shift towards medical applications. The driving force behind this progression was the fine tuning of synthetic methodologies and an enhanced understanding of the mechanisms involved[25,95].

1.3.1. Upconversion Nanoparticles ($NaYF_4$: Yb, Er/Gd): The basics

UCNPs are nanocrystalline structures consisting of a $NaYF_4$ matrix which host luminescent centres in the form of dopant ions. The dopant ions are divided into two groups; sensitizer ions and activators[96]. After photoexcitation the sensitizer causes the activator ion to become excited through non-radiative energy transfer. Energy is then received from a second sensitizer and, following the same energetic process, this causes a second excitation to a higher energy state in the activator. Hence, after relaxation to the lower electronic state, fluorescence is observed. The appropriate selection of sensitizer/activator combinations is the crucial factor for achieving a sequential absorption of photons[6].

While the UC process has been observed in the *d* block elements as well, the energy transfer relationship between trivalent lanthanide ions (Ln^{3+}) within the *f* block provides the highest UC efficiency due to their unique electronic arrangements[97]. Additionally, their transitions occur at the inner 4*f* shell which are shielded by the complete $5s^2 5p^6$ outer sub-shells. This results in relatively narrow spectral bands irrespective of dopant depth in the host lattice and a substantial reduction in electron-phonon coupling. The $4f \rightarrow 4f$ transitions are Laporte forbidden making the excited states relatively longer lived, an important requirement for upconversion to take place[96,98]. The major factor in determining the effectiveness of the UC process is the relationship between host lattice composition and dopant ion concentration.

1.3.2. Sensitizers and activators

Sensitization is a key factor in controlling the probability of UC luminescence. In single ion doped nanocrystals the efficiency is very low as there is a poor absorption cross-section between the activator ions and the incident radiation[96]. Select sensitizer ions serve to enhance the process via a non-radiative energy transfer of pump photons to the activator ion.

It has been demonstrated that, in contrast with other Ln^{3+} ions, there are four, namely: La^{3+}; Yb^{3+}; Ce^{3+} and Lu^{3+}, which possess a single excitation level. Of these, the Yb^{3+} ion is the most widely studied, since their excitation occurs at 980 nm due to the $^2F_{7/2} \rightarrow {}^2F_{5/2}$ transition with an absorption cross-section higher than for any other Ln^{3+} ion[96]. Resonant absorption with common activators such as Er^{3+} and Ho^{3+}, **Figure 1.13 B**, can take place since the relative band gaps are of similar magnitudes. The different energy transfer processes between the sensitizer and activator ions are shown in **Figure 1.13**.

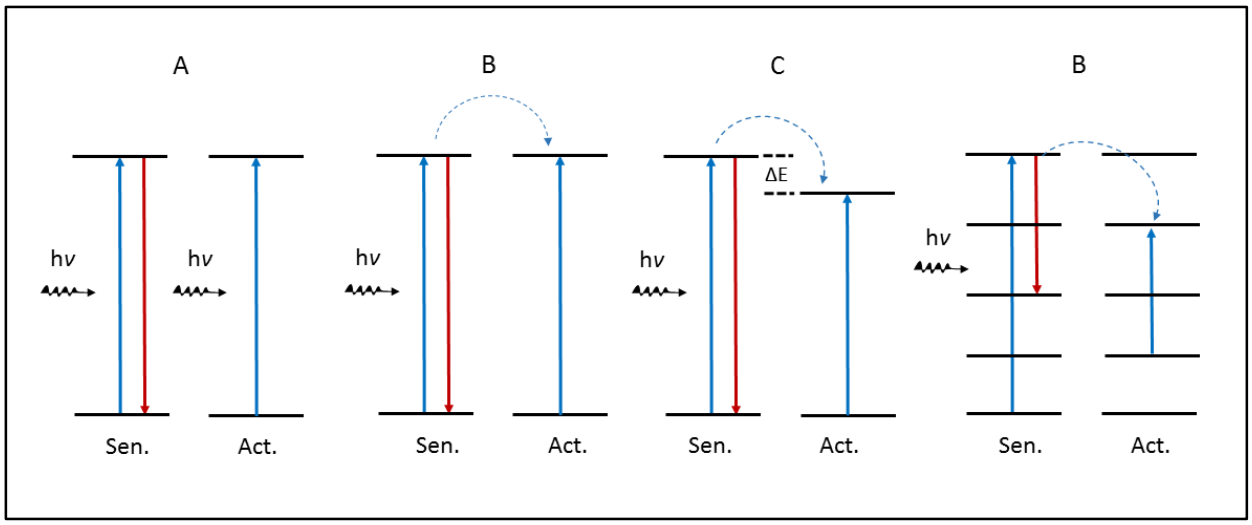

Figure 1.13: Mechanisms of energy transfer between sensitizer and activator ions within UCNPs. Resonant energy absorption (A) takes place with the transfer of a real photon and resonant absorption based on dipole-dipole coupling (B) which is nonradiative in nature. C shows a small energy mismatch between sensitizer and the activator, which is bridged by Stokes phonons, and mechanism B the cross relaxation between level pairs of dopant ions[99,100].

The first mechanism in **Figure 1.13** involves the transfer of energy via an emitted photon to the activator. Since the photon has no direct propagation path and instead radiates outwards the efficiency is based on the proximity of neighboring activators and is therefore relatively low[101]. Inset B on the other hand shows resonant transfer to the accepting ion which is assisted by dipole-dipole coupling and is nonradiative in nature. This phenomenon, known as FRET, increases by a factor of r^{-6} (where r is the distance between the donor and acceptor) and is the most efficient process for producing UC luminescence. In process C, there is an energy mismatch, ΔE, which can be bridged with the assistance of a phonon[102].

Transfer between energy levels can take place between any set of paired states provided there is only a minor energy difference between them. The equally spaced ladder-like energy levels, as observed in process **D**, cause an effect known as cross relaxation (CR). This is most common in single ion doped UC materials and systems where the activator concentration is present in excess[86]. High activator ion concentration can be increased to a threshold limit at which point the luminescence efficiency starts to decrease. In co-doped systems, a high sensitizer ratio is selected, Yb^{3+} ca. 18 mol %, facilitating the collection of pump photons. If the activator is more prevalent, CR becomes the dominant process, so consequently these ions are kept at no more than 3 mol % for Er^{3+} and 0.5 mol % when paired with Tm^{3+} [103,104].

Most Ln^{3+} ions possess multiple states involving the 4*f* orbitals which feature this ladder-like arrangement in their relative energies. The configuration features prominently in the energy level diagrams of Er^{3+}, Tm^{3+} and Ho^{3+} ions which are the most researched as dopant activators[105]. The energy gaps between excited states of these ions are relatively large and this favours multi-photon absorption and energy transfer upon sensitization[105]. For example, if the Er^{3+} ion is considered; the second excited state, $^4I_{11/2}$, and ground state, $^4I_{15/2,}$ have an energy difference of ca. 10350 cm^{-1} which closely matches that of the higher transition from $^4I_{11/2} \rightarrow {}^4F_{7/2}$ of ca. 10370 cm^{-1}, **Figure 1.15**, making the sequential absorption of photons through these levels favoured upon 980 nm excitation[96].

The population of these ascending energy levels with photons is dependent on their stability, being subject to the multiphonon relaxation rate constant[106]. The rate constant helps explain the overcoming of Kasha's law, **Section 1.1**, since fluorescence is normally observed from the lowest excitation level. As recently as 1988, a comprehensive study by van Djik and Schuurmans[106]

described this phenomenon in theoretical terms. The authors demonstrated that when 4*f* transitions are considered, fluorescence from higher energy states occurs faster than the decay rate to lower energies.

1.3.3. Dopant/Host relationship

The dopant/host relationship is arguably one of the more important aspects of the UC probability as it relates to the theory described in previous sections. Laporte's selection rule forbids a transition between levels of the same parity and this requires a partial lifting to enable the 4*f* → 4*f* transitions to take place. This can occur in the presence of a suitable ligand field where the 4*f* → 4*f* transitions can be mixed with a partially allowed transition of opposite parity. This is referred to as a forced electric dipole transition[96,107]. The embedded dopant ions are affected by the surrounding electric field, created by the host matrix, and this plays the key role in parity mixing. Host lattices are also chosen for their intrinsically low phonon energies and smaller ionic radii which reduce crystal defects and assist with the inclusion of the dopant into the unit cell[98]. High ionic radii values can cause non-radiative cross relaxations from the dopant ion excited states and subsequently lower UC emission. Initial research into UC focused on using oxide or fluoride host matrices, and the luminescent centres studied included rare earth metal oxides, phosphates and oxysulfides[108,109]. The fluoride host matrices were shown to provide superior results due to their appreciably lower phonon energies. The number of crystal defects is also limited during nanoparticle formation since the fluoride ions have similar ionic radii to the rare earth ions[99].

1.3.4. Mechanisms of upconversion

An understanding of the energy transfer processes that can take place between the sensitizer and activator guides the rational manipulation of the emission properties of UCNPs since, unlike conventional fluorescence, these processes do not occur within a single ion centre[110]. There are a number of different mechanisms that exist for the transformation of photons from a lower to a higher energetic state as shown in **Figure 1.14.**

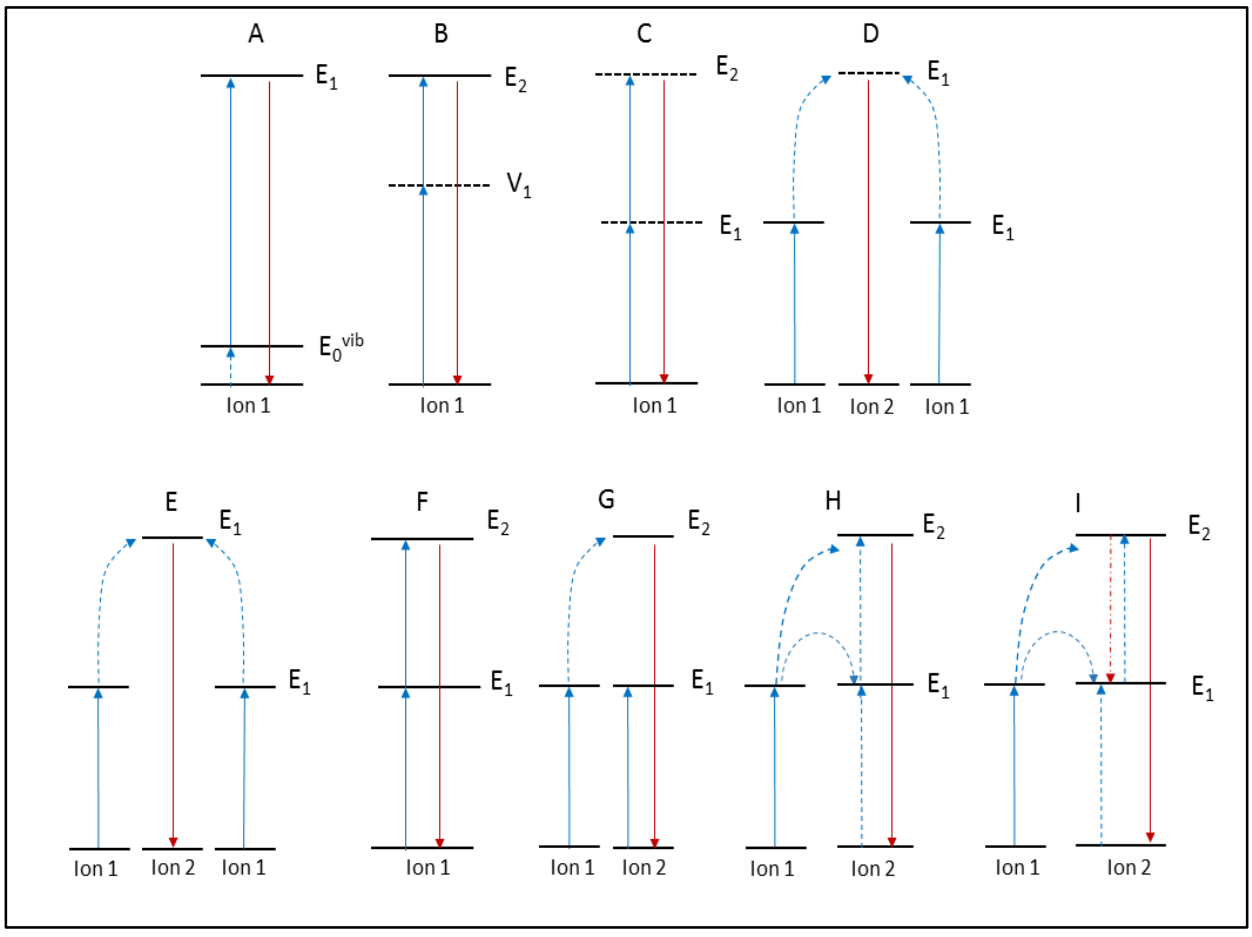

Figure 1.14: Schematic showing the different mechanisms producing anti-Stokes emission. Solid blue lines indicate photon absorption and dashed versions resonant transfer absorption. Solid red

lines indicate emission. E_1 and E_2 indicate excited state 1 and 2, respectively, while V_1 and V_2 are the 1st and 2nd virtual state, respectively.

These range from the simplest such as anti-Stokes Raman scattering (A) to second harmonic generation (C). It can also be achieved through two photon absorption (B) which is analogous to the mechanism in UCNPs with the exception that it occurs through a virtual transition state. Co-operative luminescence (D) and sensitization (E) have the same origin as the absorption of photons by two separate sensitizer ions with a lower excitation level to that of the activator[111]. The combined energies relax in the activator to yield an emission energy higher than that of the initial excitation energy[95]. The only variation comes from the point of decay, which for D, is a virtual state, and for E, a real state. Figure 1.14 F depicts two step absorption. Excitation to a metastable, real intermediate state takes place within a single ion, which subsequently undergoes a second transition to a higher level with the absorption of a photon from a second sensitizer, which follows the same relaxation process[111].

Mechanisms G and H both are termed energy transfer upconversion (ETU) and may involve sensitization from a single or multiple ions[112]. In the first case the energy is transferred to an already excited activator and with the second it occurs through sensitization, termed sensitized ETU. With the selected Yb^{3+}/Er^{3+} pairs this form of UC dominates over all other types and so will be discussed in detail in Section 1.3.4.1. The final inset on the diagram, I, is a generalized scheme of UC through the photon avalanche process[101]. As the name suggests, higher metastable energy states become extensively populated prior to an intense relaxation and involves both ETU and CR. The effect is observed in particles with high dopant concentrations, facilitating the necessary ion-

ion interaction, for the states to become saturated by CR[101]. The avalanche is then a competition between the ability of these levels to store photons with the loss of this energy. When the excitation power reaches a certain threshold the photons relax with an intense emission[113].

1.3.4.1. Energy transfer upconversion (ETU)

In 1966, an early study on UCNPs by Auzel[93] demonstrated how the pump photons are absorbed by the sensitizer and, due to the close proximity of their absorption cross-section, allows the activator to excite through resonant energy transfer. This process, known as sensitized ETU **Figure 1.14 H**, causes the population of higher excited states of the activator when the excited electron is transferred from the sensitizer to the activator[114]. The analogous case, **G**, occurs through a straight forward absorption where the activator has already been excited either via non-resonant energy transfer or through direct ground state absorption. **Figure 1.15** below depicts this for the Yb^{3+}: Er^{3+} and Yb^{3+}: Tm^{3+} dopant systems with the observed emissions in the blue, green and red regions[115].

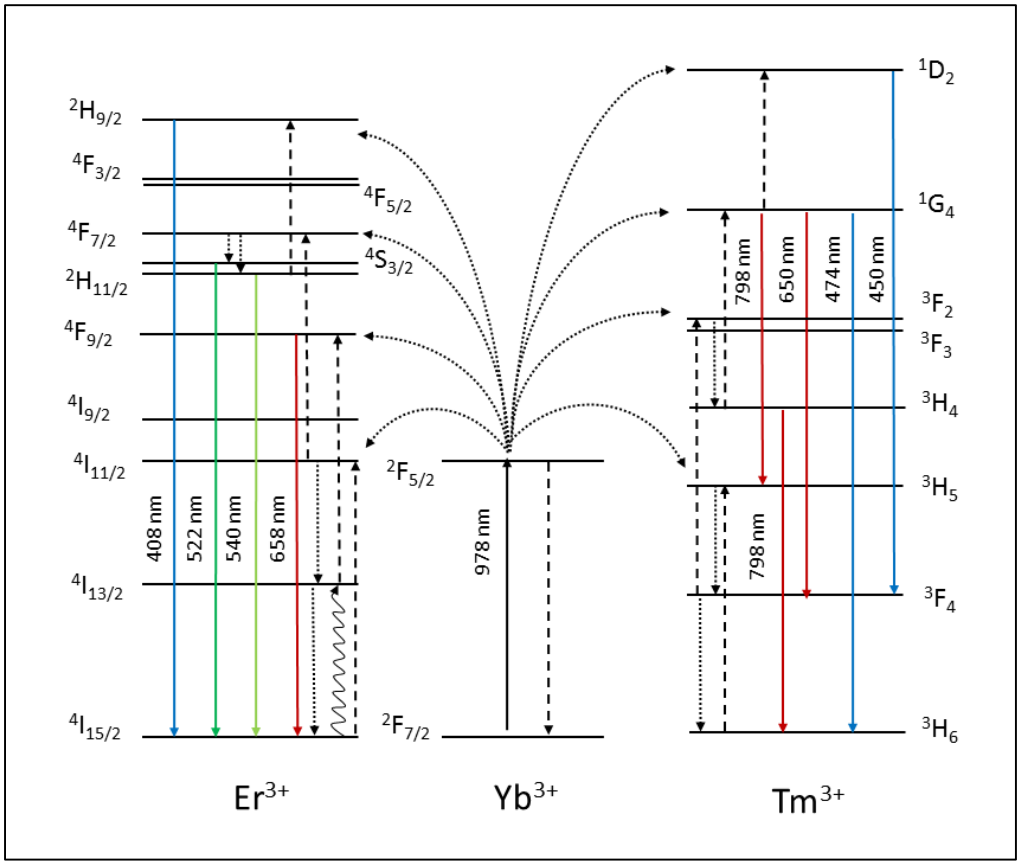

Figure 1.15: Sensitized energy transfer upconversion (sensitized ETU) between the Yb^{3+} and Er^{3+} ions. Population and relaxation from the higher energy levels $^2H_{9/2}$, $^2H_{11/2}$ and $^4F_{9/2}$ states result in the blue, green and red emission bands, respectively.

The main reason for the high upconversion efficiency of this particular mechanism stems from a) the resonant absorption between the ions and b) the similar energy levels that Er^{3+} and Tm^{3+} have to the single transition of the Yb^{3+} ion[116]. This transition, $^2F_{7/2} \rightarrow {}^2F_{5/2}$, occurs upon absorption of a photon at ca. 980 nm and will preferentially occur relative to the $^4I_{15/2} \rightarrow {}^4I_{11/2}$ transition of the Er^{3+} ion. Green emission levels, in the ca. 540 nm region, are populated by a second energy transfer to the $^4F_{7/2}$ state followed by a non-radiative decay to the $^2H_{11/2}$ and $^4S_{3/2}$ states[117].

The red emission from the $^4F_{9/2}$ state centered on 660 nm can be reached with a non-radiative decay from the $^4S_{3/2}$ state. An alternative route involves the cross relaxation from one Er^{3+} ion to another causing an excitation from its ground state to the $^4I_{13/2}$ level followed by sensitized energy transfer. This type of mechanism becomes more prominent when there is high pump photon intensity at 978 nm[118]. Lower intensity emissions in the blue region, at 410 nm, can be attributed to the higher $^2H_{9/2}$ and $^4F_{5/2}$ states and can be reached with a three step energy transfer[105]. The Tm^{3+} ion follows much the same process in reaching its respective emission levels. There is however a slight energetic mismatch with the initial transfer from sensitizer to the $^3H_5$ level. This, as has already been discussed above, can be bridged with the aid of phonon energies.

It is important to emphasize that the relaxation probability from each of these levels is reflected in their respective emission spectra. The research presented here employs co-doped Yb^{3+}/Er^{3+} UCNPs and this will be elaborated on further in Chapter 5.

1.3.5. Size and phase control

There are two main crystallographic phases for $NaYF_4$, cubic (α) and hexagonal (β), and this heavily influences the UC efficiency[105]. β-Phase crystals have been found to possess orders of magnitude greater efficiency in UC as compared to their α-phase counterparts. The phase change occurs during the heating or annealing step of the UCNP synthesis[86], Scheme 2.3.7. The lower symmetry β-phase crystals result in a closer proximity of the ions than in the α phase crystals and this increases the efficiency of resonant energy transfer[115]. A study conducted by Liang et al.[119] found that the change from the α- to β-phase is dependent on both reaction time and temperature.

They found that heating at 280 °C for a 3 h period completes the phase change, since the β-phase is more thermodynamically stable and is favoured at higher temperatures[120].

While small crystal sizes are desired for their favourable surface to volume ratio, they also result in a reduced UC efficiency due to quenching effects caused by solvent molecules and the nanoparticle capping agent[121]. A technique often employed for the control of both size and phase is doping with lanthanides bearing larger ionic radii than that of the luminescent centres. The addition of Gd^{3+} (r = 1.193 Å)[122] has proved extremely effective in producing hexagonally pure UC nanoparticles.

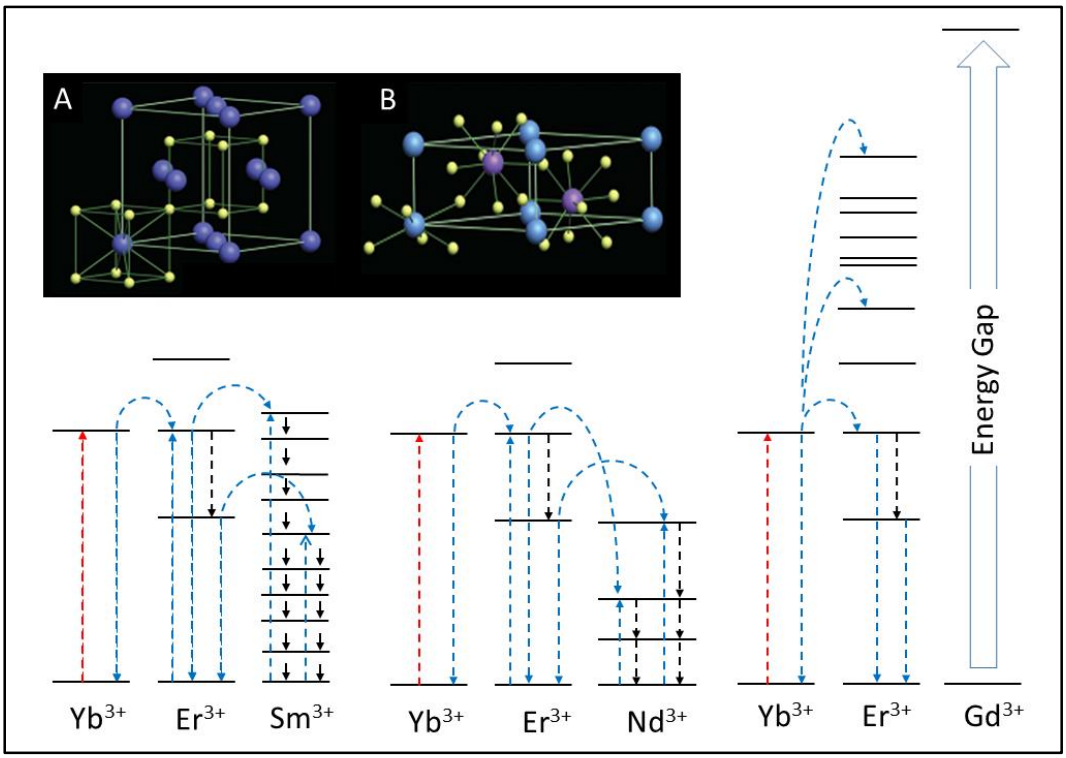

Figure 1.16: Diagram showing the effects of phase change dopants (Sm^{3+}, Nd^{3+} and Gd^{3+}) have on the energy transfers from sensitizer to activator. Insets for α-phase (A) and β-phase (B) are also shown with the different arrangement of ions in their

respective unit cells. A: dark blue balls show the RE^{3+} and Na cation sites. B: Light blue balls represent the Na^{+} sites (1) and purple the RE^{3+} sites (2). F^{-} ions, in both cases, are highlighted in yellow[117,123].

Other phase control dopants such as Sm^{3+} (r = 1.219 Å)[122] and Nd^{3+} (r = 1.249 Å)[122] have also been tested, however quenching effects and CR are prevalent in these contexts. These drawbacks are addressed with the addition of the Gd^{3+} ion[122]. Figure 1.16 demonstrates that the first excited state situated at a much higher energy level than the transitions involved in the UC process and, hence, no CR or quenching can take place. The inclusion of the Gd^{3+} ions large radii into the unit cell causes an irregular distortion in the electron cloud surrounding the ions due to their large radii, which assists in the α- to β-phase change. Initial studies revealed that a 20 h reaction time was required for this phase change to occur and, upon its addition, was reduced to 2 h[123] and resulted in high quality UCNPs. Research conducted by Feng Wang and co-workers[123] showed that no additional peaks were observed in X-ray diffraction (XRD) measurements. This indicates that there was no change in the ionic arrangement of the unit cell since the $NaYF_4$ and $NaGdF_4$ host lattices occupy the same space group, the only difference being in their unit cell volumes[123].

1.3.6. Synthesis and surface modification

The synthesis of UCNPs can be achieved through a number of chemical methods; these being co-precipitation, thermal decomposition, hydro(solvo) thermal synthesis[115], sol-gel processing[124] and a combustion method[125], the most prominent in this research field being the former three. Each method offers control of different aspects of the NP characteristics such as size distribution,

chemical composition, morphology, surface functionalization and optical properties[96]. For example, the co-precipitation method stands out as one of the most efficient in producing near uniform, ultra-small nanoparticles of ca. 5 nm diameter. The method is relatively cheap and time efficient. High temperatures are needed for the post synthesis annealing step, however with an optimum temperature at 300 °C[96]. High pressure is used for the hydro(solvo) thermal synthesis producing nanoparticles with an increased solubility at a much lower temperature[96]. Reactions are carried out in autoclaves which can reduce the reaction time with temperatures and pressures above the solvent critical point. This method has been used for synthesis of phase pure UCNPs with the main drawback being the lack of control over β-phase formation[124].

The nanoparticles presented in this work were synthesized using the thermal decomposition method, known for its production of high level crystalline nanoparticles and size mono-dispersity[96]. The metal precursors used decompose at high temperatures and therefore require the use of a high boiling point solvent such as 1-octadecene[123]. High temperatures and costly reagents are a disadvantage along with the toxic gases that these metal trifluoroacetates produce upon decomposition[126,127]. The size and shape of the nanoparticles are controlled with oleic acid (OE) acting as the capping agent and surfactant during nanoparticle growth[127]. Its small carbon chain prevents aggregation of the nanoparticles but lends itself to surface defects and quenching effects for surface dopant ions. OE capped nanoparticles can only be dispersed in a few organic solvents which form colloidal solutions after lengthy sonication but do not provide the necessary surface groups that are compatible with biomolecules.

Surface modification is therefore an important further step towards *in vivo* studies. The preferred and well established method is coating with an amorphous silica (SiO_2) layer[111]. Two methods

have been developed for this modification: the Stober and reverse microemulsion methods[128]. The former will not work for the hydrophobic surface of UCNPs as the procedure requires dissolving in an organic solvent such as ethanol or isopropanol. The microemulsion method has proven to be far superior in this regard. The name comes from the water-in-oil emulsion formed by dissolving the nanoparticles in cyclohexane, ammonia and Igepal CO-520[128]. This is proceeded by a sonication period to ensure single nanocrystals encapsulated within each microemulsion. The coating process can be quite tedious and if the previously mentioned step is carried out incorrectly, it can cause the nanoparticles to aggregate[129,130]. A silica shell also provides the scaffold for further functionalization necessary for the conjugation to biomolecules[105]. This thesis describes an attempt to place amine groups on the surface allowing for covalent linkages to be created with a carboxylic acid and ester groups. This will be dealt with in more detail in Chapter 5.

1.3.7. Applications of upconversion nanoparticles

The ability of UCNPs with different dopants to generate various high energy emission bands from low energy excitation is sought after in many applications. There have seen successful applications in the fields of lasers[131], photovoltaic solar cells[132] as well as more unusual areas such as anti-counterfeiting[133], currency security[134] and molecular memory switches[135,136]. They have also found applications in various biomedical fields with a strong emphasis on four key characteristics: their absorption in the NIR region gives them an extremely favourable signal to noise ratio as most biological samples display autofluorescence upon UV excitation; the nanoparticles are not degradable under ambient light or temperature; the nanoparticles exhibit excellent photostability;

their small size and ability to be functionalized makes them target specific[105]. On this basis they can be divided into three classes in sensor related applications: *in vivo* imaging, *in vitro* detection and sensing utilizing the FRET process between surface functionalized molecules. The imaging of biological processes, first carried out by Zijlmans and co-workers in their 1999 paper[137], is one of many diagnostic techniques where biomolecules have been conjugated to UCNPs with binding sites towards a specific target receptor. A study carried out by Lim et al.[138] showed that the UCNPs could be used to visualize the digestive system of worms. After 980 nm excitation the outlining of the intestines could clearly be visualized. A more recent development in the Zhang and co-workers group[139] were able to detect the presence of nanoparticles at 10 mm depth present in rats.

The luminescence capability of UCNPs can be applied to a variety of *in vitro* assays displaying a lower detection limit by comparison to conventional methods[96]. This was demonstrated over ten years ago by Hampl et al.[140] with a 10 fold improvement in the detection using large Y_2O_2S:Yb/Er particles in immunochromatogaphic assays at 10pg/100 µl. Using the same nanoparticles with a 400 nm diameter Tanke et al.[141] were able to lower the detection limit still further.

The coupling of UCNPs with organic fluorophores is a popular technique for increasing the detection specificity and efficiency. FRET systems have given rise to a multitude of chemical sensors where the UCNPs act as an energy donor towards a surface molecule tailored as an acceptor. One such example has grafted gold nanoparticles (AuNPs) onto the surface of lysine capped UCNPs[142]. Electrostatic forces hold the negatively charged AuNPs to the outer positive shell on the UCNPs effectively absorbing its emission, due to the overlap between the UCNP emission and AuNP absorption spectra. In the presence of Cr^{3+}, as the selected analyte, the AuNPs are removed from the surface and the fluorescence is switched on[142]. Similarly, the energy

transfer between UCNPs capped with poly ethylene glycol (PEG) embedded with an iodine modified BODIPY has been demonstrated to act as a PS for $^1O_2$ generation after NIR excitation enabling possible biomedical applications. This study proved successful for the death of cancer cells after the grafting and chemisorption of the iodinated BODIPYs into the PEG[143].

1.4. Summary of aims

This thesis strives to expand and enhance the level of understanding of BODIPY dye chemistry and their conjugate to UCNPs, by a) studying the $^1O_2$ generating capabilities of a novel BODIPY compound formed by a Sonogashira coupling reaction and b) the interaction between iodinated BODIPYs and UCNPs. The aims of this thesis may be summarized as follows:

1. The optimization of the Sonogashira coupling procedure
2. Synthesis and characterization of a novel BODIPY dimer
3. A comparison of the $^1O_2$ generating capabilities between this novel BODIPY and its precursor BODIPY
4. The synthesis and characterization of uncapped and silica coated $NaYF_4$:Yb^{3+}/Er^{3+} UCNPs.
5. The amine functionalization of silica coated UCNPs and its characterization.
6. The direct conjugation of these amine bearing silica coated UCNPs with an iodinated BODIPY dye containing a methyl ester functionalization.
7. The complete characterization of the aforementioned compounds.
8. A study of the interaction between the iodinated BODIPY and UCNPs
9. The molecular modelling of all BODIPY dyes synthesized.

Summary of synthetic compounds in this thesis

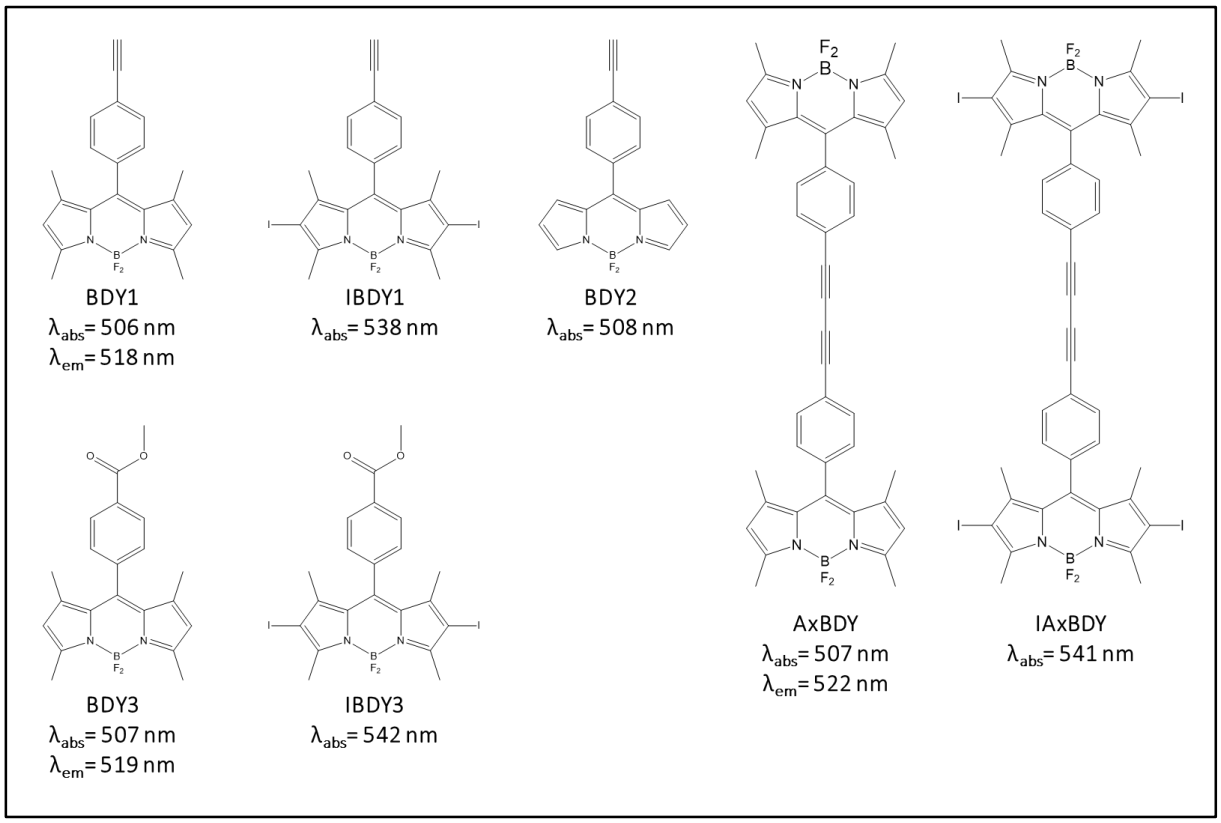

Figure 1.17: Diagram outlining the organic compounds synthesized with their assigned nomenclature used throughout and fluorescence properties measured.

CHAPTER TWO

Experimental

2. Experimental

2.1. Materials

All reagents were used without further purification unless otherwise stated. Dichloromethane (DCM) and hydrochloric acid (HCl) were purchased from B&M Scientific. Yttrium nitrate, erbium chloride, ytterbium chloride, gadolinium chloride, 3-aminopropyltriethoxysilane (APTES), 1-octadecene, Igepal CO-520, 4-formylbenzoic acid, 2,4-dimethylpyrrole, trifluoroacetic acid (TFA), 2,3-dichloro-5,6-dicyano-*p*-benzoquinone (DDQ), boron trifluoreide diethyl etherate ($BF_3{\cdot}Et_2O$), *N*-iodosuccinimide (NIS), triethylamine (TEA), palladium chloride triphenylphosphine ($PdCl_2(PPh_3)_2$), copper iodide, sodium sulphate, sodium fluoride, 4-bromo-1,2-diaminobenzene, 4-bromoanaline, di-tert-butyl dicarbonate (Boc_2O) and tetraethoxysilane (TEOS) were purchased from Sigma Aldrich. Oleaic acid (OE), sodium hydroxide and dimethyl formamide (DMF) were purchased from UnivAR, Fuka and Saarchem respectively. Toluene, reagent grade chloroform and 25% ammonia were supplied by Minema. Silica gel 60, for flash column chromatography and cyclohexane were purchased from Merck.

2.2. Instrumentation

- Transmission electron microscope (TEM) images were collected using a Zeiss Libra® transmission electron microscope.
- Monochromatic laser light in the 600–700 nm range was provided by an Ekspla NT 342B-20-AW pulsed laser (2.0 mJ/5 ns, 20 Hz) and used for obtaining the singlet oxygen quantum yields of all applicable compounds with DPBF as a $^1O_2$ quencher. All measurements were carried out with EtOH as the solvent.

- Analysis of samples by XRD were carried out on a Brucker D8 Diffractometer fitted with a Lynx Eye detector under Cu Kα (λ=1.5405 Å) with a scanning rate of 192 seconds per step. The samples were prepared on a zero background silicon wafer slide.
- UV-visible absorption spectra were recorded with a Shimadzu UV-2550 spectrophotometer.
- Fourier transform Infrared spectra (FTIR) data were obtained on a Brucker Alpha model FT-IR spectrophotometer with platinum ATR (attenuated total reflectance).
- Nuclear magnetic resonance (NMR) spectra were measured on a Brucker AMX 600 NMR spectrometer in chloroform-d_1, unless otherwise stated, and analyzed using MestReNova version 6.0 software.
- Mass spectral data were collected using the Brucker AutoFLEX III Smartbeam TOF/TOF mass spectrometer with dithranol as the MALDI matrix.
- Compounds possessing a mass lower than 500 g/mol were measured by electron spray ionization (ESI) mass spectrometry with an Expressions CMS Advion ESI-MS with CAMAG TLC-MS interface. Data processing was carried out using the Advion Data Express instrument software. The ESI tuning mix was obtained from Agilent technologies.
- Elemental analysis was run on a Vario-Elementar Microcube ELlll instrument.
- Fluorescence spectra of UCNPs were measured with a FluoTime 300 'Easy Tau' spectrophotometer (PicoQuant GmbH). The samples were excited at 975 nm with a diode laser (LDH-D-C-980, CW 180 mW, PicoQuant GmbH) with a Peltier cooled photomultiplier detector (PMA-C 192-M, PicoQuant GmbH). Continuous wave excitation was used to obtain steady state emission, while time resolved measurements were performed using an

80 MHz repetition frequency with a maximum pulse width of 500 ps. Emissions were detected under the magic angle utilizing a PMA-C 192-M photomultiplier tube (Picoquant, GmbH). Lifetime measurements for the green emission band was gathered using a 539 nm excitation wavelength from a PDL 800-B diode laser at an 80 MHz repetition rate. The magic angle was used for detection using an H10330A-45 NIR photomultiplier tube (Hamamatsu). The integrated TimeHarp 260-N TCSPC card (Picoquant, GmbH) was used for photon counting. Emission wavelengths were selectively detected using an Omni-λ300 grating monochromator at 1200 lines/ mm with a spectral width of 4 mm.

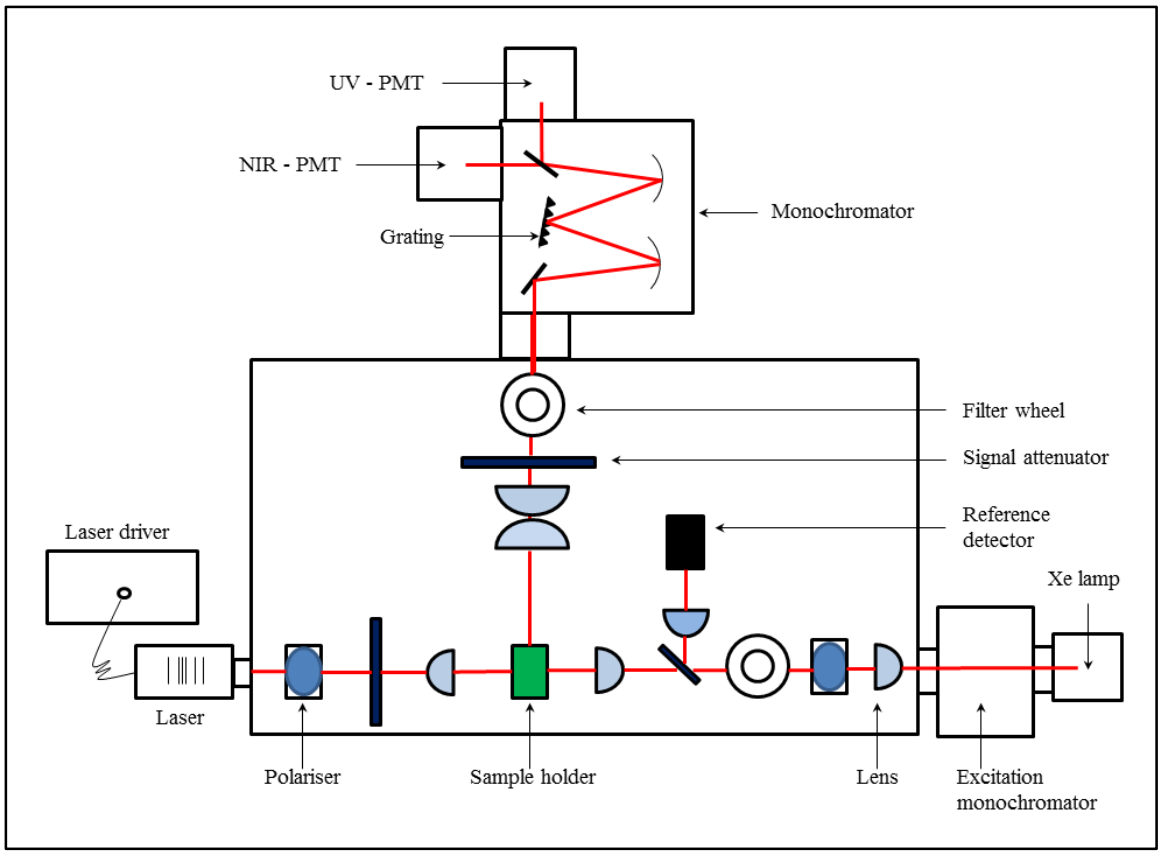

Figure 2.1: Diagram showing the internal components and laser path for the Fluotime 300.

- Optimized geometries and molecular orbitals (MOs) were derived for all BODIPY structures using the density functional method (DFT) for geometry optimizations with B3LYP functional together with 6-31G(d) basis sets. A time dependent method (TD-DFT) with the coulomb attenuated B3LYP (CAM-B3LYP) parameter was used for calculating the electronic absorption properties, since this contains a long-range correction that provides more accurate trends for electronic transitions that contain significant charge transfer effects.

2.3. Syntheses

2.3.1. 4,4-difluoro-1,3,5,7-tetramethyl-8-(4-ethynylbenzene)-4-boro-3a,4a-diaza-*s*-indacene (BDY1)

The synthesis of the ethynyl functionalized BODIPY was carried in a single step reaction. 2, 4-Dimethylpyrrole (0.475 ml) and 4-ethynylbenzaldehyde (0.3 g) were added to dry DCM (5 ml). To this mixture, 3 drops of TFA were added and the reaction was left to stir for 30 min under Ar gas. Consumption of the 4-ethynylbenzaldehyde was monitored by thin layer chromatography (TLC) after which the temperature was lowered to 0 °C and *p*-chloranil (0.678 g) was added. The solution was left to stir for 4 h. The temperature was lowered again to 0 °C followed by the dropwise addition of TEA (2.24 ml) and $BF_3{\cdot}Et_2O$ (3.11 ml). After overnight stirring the resulting solution was washed with deionized water and the product separated by flash column chromatography with toluene as the eluent. A diagrammatic representation can be seen in Scheme 3.2.1.

Dark blue crystals, 65 % yield

UV-Vis (toluene): 507 nm, log ε (THF): 74100 $M^{-1}.cm^{-1}$

IR (ν_{max}/cm^{-1}): 3255 (C-H, ethynyl), 2921 (C-H), ^{1}H NMR ($CDCl_3$, 300 MHz): δ, ppm 1.40 (s, 6H, methyl-H), 2.55 (s, 6H, methyl-H), 3.18 (s, 1H, ethynyl-H), 5.98 (s, 2H, core-H), 7.28 – 7.26 (d, *J* = 6.0 Hz, 2H, phenyl-H), 7.63 – 7.62 (d, *J* = 3.0 Hz, 2H, phenyl-H), Calc for: $C_{17}H_{12}BF_2N_2$: C 72.44, H 5.50, N 8.05. Found: C 70.76, H 6.00, N 7.71 (includes 1 mol THF). MS (ESI) m/z: calcd. 348.2; Found: 349.1.

2.3.2. 4,4-difluoro-1,3,5,7-tetramethyl-2,6-diiodo-8-(ethynylbenzene)-4-boro-3a,4a-diaza-*s*-indacene (IBDY1)

Following purification and characterization of BDY1 the attachment of iodine atoms at the 2, 6-positions was carried out through a facile halogenation reaction. NIS was added (0.1756 g, 3 eq.) to a stirring solution of anhydrous DCM (6 ml), prepared overnight on oven dried 4 Å molecular sieves, containing BDY1 (0.10 g, 1 eq.) and left to stir under an Ar gas overnight at room temperature. After the starting BODIPY fraction was no longer observed by TLC, the main band in the UV-visible absorption spectrum shifted to red from 501 nm to 536 nm. The reaction was quenched with the addition of water. The pure compound was attained by flash chromatography with toluene as the eluent. The general procedure can be viewed in Scheme 3.2.1.

Fine, deep red crystals, 83 % yield

UV-Vis (toluene): 537 nm, log ε (THF): 39000 $M^{-1}.cm^{-1}$

IR (ν_{max}/cm^{-1}): 3268 (C-H, ethynyl), 2919, 2853 (C-H), ^{1}H NMR ($CDCl_3$): δ, ppm 1.43 (s, 6H; methyl-H), 2.67 (s, 6H; methyl-H), 3.25 (s, 1H; ethynyl-H), 7.26 – 7.27 (d, *J* = 6.0 Hz, 2H; phenyl-H), 7.67 – 7.69 (d, *J* = 12.0 Hz, 2H; phenyl-H) Calc for: $C_{17}H_{12}BF_2N_2$: C 42.04, H 2.86, N 4.67. Found: C 46.84, H 5.23, N 2.26 (includes 2 mol THF). MS (ESI) m/z: calcd. 599.95; Found: 606.83 $[M+6H]^+$.

2.3.3. 4,4-difluoro -8-(4-ethynylbenzene)-4-boro-3a,4a-diaza-*s*-indacene (BDY2)

To a stirring aqueous HCl (0.18M, 11.2 ml) solution, pyrrole (351 µl, 2 eq.) was added followed by 4-ethynylbenzaldehyde (0.15 M, 0.22 g, 1 eq.). This mixture was left under Ar gas for approximately 2 h, until a brown precipitate had formed which was washed several times with water and petroleum ether. DCM (5 ml) was then added followed by the addition of *p*-chloranil (0.498 g, 1.2 eq.) at 0 °C and the mixture was left for a further 30 min. TEA (1.684 ml, 7 eq.) was added dropwise at 0 °C followed by $BF_3{\cdot}Et_2O$ (2.28 ml, 11 eq.). The solution was left to stir overnight after which it was extracted by column chromatography with a toluene eluent, as outlined in Scheme 3.1.2.

Dark blue crystals, 70 % yield.

UV-Vis (toluene): 507 nm, log ε (THF):28000 $M^{-1}.cm^{-1}$.

IR (v_{max}/cm^{-1}): 3296 (C-H, ethynyl), ^1H NMR ($CDCl_3$, 600 MHz): δ, ppm 3.28 (s, 1H ; ethynyl–H), 6.63 – 6.60 (d, *J* = 6.0 Hz, 2H; core-H), 6.99 – 6.95 (d, *J* = 6.0 Hz, 2H; core-H), 7.61 – 7.58 (d, *J* = 6.0 Hz, 2H; core-H), 7.72 – 7.69 (d, *J* = 6.0 Hz, 2H; phenyl-H), 7.99 (s, 2H; core-H) Calc for: $C_{17}H_{12}BF_2N_2$: C 69.90, H 3.80, N 9.59. Found: C 69.61, H 3.45, N 9.40. MS (ESI) m/z: calcd. 293.1; Found: 294.

2.3.4. 4,4-difluoro-1,3,5,7-tetramethyl-8-(methyl benzoate)-4-boro-3a,4a-diaza-*s*-indacene (BDY3)

The same procedure was followed as described in Section 2.3.1 by starting with methyl 4-formylbenzoate instead of 4-ethynylbenzaldehyde yielding the final methyl ester functionalized

BODIPY. This procedure is outlined in **Scheme 3.1.3.** Flash column chromatography with a 1:1 solution of ethyl acetate: hexane was used to purify the product.

Orange crystals, 61 % yield.

UV-Vis (toluene): 506 nm, IR (neat): 2950 cm^{-1}, log ε (THF): 54000 $M^{-1}.cm^{-1}$.

IR (v_{max}/cm^{-1}): 2955 (C-H), 1717 (C=O), 1274, 1055 (C-O), ^{1}H NMR ($CDCl_3$, 600 MHz): δ = 1.38 (s, 6H; methyl-H), 2.58 (s, 6H; methyl-H) 4.00 (s, 3H ; methyl ester-H), 6.01 (s, 2H, core-H), 7.44 – 7.42 (d, *J* = 12.0 Hz, 2H; phenyl-H), 8.21 – 8.20 (d, *J* = 6.0 Hz, 2H; phenyl-H), Calc for : $C_{17}H_{12}BF_2N_2$: C 65.99, H 5.54, N 7.33. Found: C 58.42, H 5.01, N 5.87 (includes 3 mol water). MS (ESI) m/z: calcd. 382.17; Found: 386 $[M+4H]^+$.

2.3.5. 4,4-difluoro-1,3,5,7-tetramethyl-2,6-diiodo-8-(methyl benzoate)-4-boro-3a,4a-diaza-*s*-indacene (IBDY3)

Iodination was carried out in the same manner as procedure 2.3.2, **Scheme 3.2.1.** The product was isolated with flash column chromatography by using a 1:1 Ethyl acetate:hexane as the eluent.

Bright red crystals, 81 % yield.

UV-Vis (toluene): 541 nm, log ε (THF): 73000 $M^{-1}.cm^{-1}$.

IR (v_{max}/cm^{-1}): 2921 (C-H), 1716 (C=O), 1275, 1052 (C-H). ^{1}H NMR ($CDCl_3$, 600 MHz): δ, ppm (s, 1H; ethynyl–H), 6.63 – 6.60 (d, 2H; core-H), 6.99 – 6.95 (d, 2H; core-H), 7.61 – 7.58 (d, 2H; core-H), 7.72 – 7.69 (d, 2H; phenyl-H), 7.99 (s, 2H; core-H) Calc for : $C_{17}H_{12}BF_2N_2$: C 42.04, H 2.86, N 4.67. Found: C 46.84, H 5.23, N 2.26 (includes 2 mol THF). MS (ESI) m/z: calcd. 633.96; Found: 634.89.

2.3.6. Synthesis of *N, N'*-di-(*tert*-Butoxycarbonyl)-4-bromo-1,2-diaminobenzene and *N, N'*-di-(*tert*-Butoxycarbonyl)-4-bromo-1-aminobenzene

The initial research of this thesis was aimed at the synthesis of novel BODIPYs bearing a diamine (A) and amine functional group (B) at the meso-position, Scheme 3.3.1. The procedure for the prerequisite di-tert-butyl dicarbonate (Boc_2O) protected amine compounds is described. Guanidine hydrochloride (GuHCl) (4 eq.) was added together with Boc_2O (0.15 eq.) in an. EtOH (3 ml). The mixture was purged with N_2 gas and stirred for 15 min, while maintaining an N_2 atmosphere, after which either 4-bromo-1,2-diaminobenzene (1 eq.) or 4-bromoanaline (1 eq.) for (B) was added. The mixture was then heated to 40 °C for 30 min and TLC was carried out to confirm the formation of a new product. The mixture was allowed to cool and the pure product was obtained by recrystallization from additional MeOH.

(A) Fine white crystals, 77% yield, (B) Large clear crystals, 86% yield.

(A) IR (ν_{max}/cm^{-1}): 3278 (N-H), 1707 (C=O, ester); ^{1}H NMR (600 MHz, DMSO-d_1): δ = 1.47 (2 × s, 18H, methyl-H), 7.22 (d, 1H, *J* = 8.7, 2.4 Hz, phenyl-H), 7.47 (d, 1H, *J* = 8.5 Hz, phenyl-H), 7.73 (s, 1H, phenyl-H), 8.64 – 8.60 (m, 2H, N-H). (B) ^{1}H NMR (600 MHz, DMSO-d_1): δ = 1.52 (s, 9H, methyl-H), 6.45 (s, 1H, N-H), 7.42 (m, 4H, phenyl-H).

2.3.7. Synthesis of novel ethynyl bridged BODIPY dimer (AxBDY)

The Sonogashira coupling reaction was followed as outlined by A. Hamze et al.[144], summarized in Scheme 3.3.2. A solution of $PdCl_2(PPh_3)_2$ (0.01 eq.), CuI (0.1 eq.) BDY1 (1 eq.) and piperidine (2 eq.) were added together in dry THF (3 ml). The reaction was allowed to proceed overnight, and

TLC was used to check for the complete consumption of the starting material. The product was separated via flash column with 1:1 ethyl acetate:hexane as the eluent. Piperidine was prepared by placing 10 ml on a pellet of NaOH for 1 week prior to synthesis. THF was dried on Na wire with benzophenone as an indicator and was distilled after 48 h. Synthesis was conducted under an Ar atmosphere and quenched with a saturated solution of Na_2SO_4. Column chromatography was used to purify the target compound with ethyl acetate:hexane (1:1) as the eluent.

Dark blue crystals, 54 % yield.

UV-Vis (toluene): 507 nm, log ε (THF): 119000 $M^{-1}.cm^{-1}$.

IR (v_{max}/cm^{-1}): 2920 (C-H, ethynyl), ^1H NMR ($CDCl_3$, 400 MHz): δ, ppm 1.36 (s, 12H ; methyl-H), 2.56 (s, 12H; methyl-H), 5.99 (s, 4H; core-H), 7.42 – 7.40 (d, *J* = 8.0 Hz, 4H; phenyl-H), 8.19 – 8.17 (d, *J* = 8.0 Hz, 4H; phenyl-H) Calc for: $C_{17}H_{12}BF_2N_2$: C 72.65, H 5.23, N 8.07. Found: C 71.36, H 3.97, N 5.16. MS (ESI) m/z: calcd. 694.38; Found: 694.30.

2.3.8. Iodination of ethynyl BODIPY dimer (IAxBDY)

The introduction of iodine groups onto both BODIPY chromophores was carried out following procedure outlined in Scheme 3.2.1. The mole ratio was adjusted to 6:1 with all other conditions kept the same.

Bright red crystals, 76 % yield.

UV-Vis (toluene): 538 nm, log ε (THF): 45300 $M^{-1}.cm^{-1}$

MS (MALDITOF) m/z: calcd: 1197.9; Found: 1203 $[M+5H]^+$.

2.3.9. Synthesis and functionalization of Upconversion Nanoparticles

2.3.9.1. Synthesis of oleate capped $NaYF_4$ upconversion nanoparticles

A thermal decomposition method was used in the synthesis of oleic acid capped UCNPs. $Y(NO_2)_3$ (5.2×10^{-4} mol, 199.2 mg), $ErCl_3$ (1.6×10^{-5} mol, 6.1 mg), $YbCl_3$ (1.4×10^{-4} mol, 55.8 mg), and $GdCl_3$ (1.2×10^{-4} mol, 44.1 mg) were added together with MeOH (4 ml). A solution of 1-octadecene (14 ml) and OE (6 ml) was added to this, sonicated for 10 min and subsequently heated to 160 °C for 30 min. After cooling to room temperature a MeOH (10 ml) solution containing NaF (3.1×10^{-4} mol, 116.1 mg) and NaOH (2.0×10^{-4} mol, 80 mg) was added and the mixture was heated further to 70 °C for 30 min. Once the MeOH had evaporated the solution was cooled down to room temperature, and was then heated to 300 °C for 1.5 h under Ar gas. The nanoparticles were extracted with cyclohexane, washed several times with a 1:1 EtOH/MeOH mixture and oven dried overnight at 100 °C before use.

2.3.9.2. Silinization of oleate capped upconversion nanoparticles (Si@UCNP)

Oleate capped UCNPs (70 mg) were dispersed in cyclohexane (65.0 ml) together with Igepal CO-520 (1.0 ml) and sonicated for 10 min. Additional Igepal CO-520 (4.0 ml) was added along with 25% ammonia (0.96 ml) and the mixture was left to sonicate for 1.5 h to ensure complete dispersion. Then, under rapid stirring, tetraethoxysilane (TEOS, 400.0 µl) was added and the solution was left to stir for 4 days. The product was initially washed with MeOH and then several times with a water:EtOH (1:1) mixture, and dried overnight at 70 °C before use. A schematic representation can be seen in Scheme 5.1.

2.3.9.3. Functionalization of silica coated upconversion nanoparticles

The Si@UCNPs (10.0 mg) were washed several times with anhydrous EtOH followed by toluene dispersed in a mixture of dry DMF (12.0 ml) and dry toluene (8.0 ml) and stirred for 8 min. 3-aminopropyltriethoxysilane (APTES) was then added dropwise and the reaction mixture was left to stir for 24 h at room temperature under an Ar atmosphere, Scheme 5.1. The nanoparticles were extracted using a 1:1 toluene/MeOH mixture and oven dried overnight before use.

2.3.9.4. Conjugation of amine functionalized upconversion nanoparticles and iodinated esterBODIPY

The introduction of an amide link between the functionalized UCNP, Section 2.3.8.3, and the iodinated ester BODIPY, Section 2.3.5, was performed in a single step. The nanoparticles (10 eq. by mass) were dispersed in MeOH (5 ml) after which the BODIPY (0.054 g, 1 eq.) was added. The solution was left to stir for 48 h, extracted with a 1:1 DCM/MeOH mixture until a clear supernatant appeared, and was then dried overnight on a bed of Na_2SO_4 before use.

CHAPTER THREE

BODIPY Dyes

3. BODIPY Dyes

The synthesis of BODIPY dyes was carried out using two different methods outlined in **Section 1.2.2**. Compounds BDY1 and BDY3, bearing methyl groups at the 1, 3, 5, 7-positions of the core, were synthesized following the TFA catalyzed method whereas the synthesis of BDY2, with an unsubstituted core, was carried out using the water precipitation method with an HCl catalyst. BDY1 and 3 were iodinated, forming IBDY1 and IBDY3 respectively, at the 2, 6-positions of the chromophore stimulating their ability to produce $^1O_2$ through the heavy atom effect.

In **Section 3.3** the attempted synthesis of a BODIPY series is discussed using BDY1 as the starting material for the Sonogashira coupling reaction. The proposed structures displayed varying amine groups at the meso-position. The unsuccessful synthesis did, however, lead to the formation of a novel BODIPY dimer, abbreviated as AxBDY. Following its iodination, forming IAxBDY, at all four possible sites on both BODIPY moieties, it was found to have an increased ability to generate $^1O_2$ by comparison to the monomer, IBDY1. The BODIPYs were characterized by mass spectrometry, and UV-visible absorption and NMR spectroscopy, with the exception of IAxBDY, since there was not enough sample to measure NMR spectroscopy. The photophysical data for the synthesized compounds were also measured where applicable.

3.1. Synthesis and characterization

3.1.1. 4,4-difluoro-1,3,5,7-tetramethyl-8-(4-ethynylbenzene)-4-boro-3a,4a-diaza-*s*-indacene (BDY1)

A BODIPY with an ethynylphenyl group at the meso-position was synthesized, Scheme 3.1.1, from 2, 4-dimethylpyrrole and subsequently provided the main building block for the Sonogashira coupling reaction described in Section 3.3. During the synthesis, strict oxygen free conditions were ensured as reports indicate the sensitivity of the reaction to air[59]. This was carried out with the preparation of anhydrous DCM (an. DCM) using 4 Å molecular sieves and glassware cooled down in the presence of N_2 gas after being oven dried overnight. The DCM was left for 24 h on the molecular sieves before use. As can be inferred, this reduced the chance for atmospheric water contamination. At each phase of the synthesis the reaction was purged with N_2 gas and was conducted under an N_2 atmosphere.

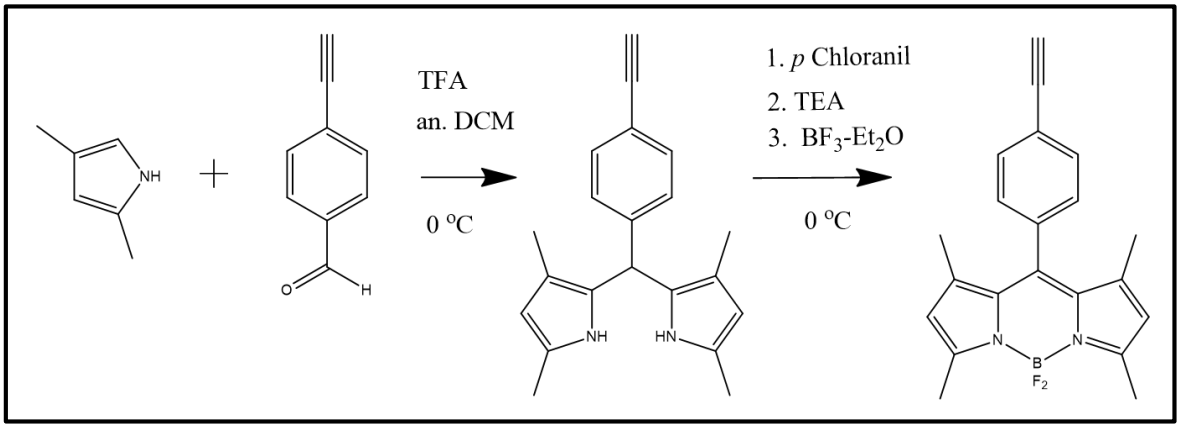

Scheme 3.1.1: Pathway outlining the synthesis of the meso-substituted ethynyl BODIPY, BDY1.

A solution of 2,4-dimethylpyrrole (3 eq.) and 4-ethynylbenzaldehyde (1 eq) was prepared in an. DCM. The reaction was catalyzed with the two drops of TFA which acts vigorously when added to the solution and produced an instant colour change to red indicating the formation of the dimethyldipyrromethane intermediate. After monitoring the reaction at 5 min intervals the starting material fraction disappeared on the TLC plates at ca. 30 min, as reported in the literature[46]. The π-conjugation between the two pyrrole moieties was achieved though the addition of *p*-chloranil, added, which reduced the meso-carbon atom from a tetrahedral sp^3 to a planar sp^2 conformation. The addition of *p*-chloranil was carried out at 0 ^oC, since this minimizes the occurrence of side reactions[46]. The formation of the BODIPY chromophore was completed with the removal of the protons from the pyrrole nitrogen atoms with TEA (7 eq.), added dropwise at 0 ^oC, followed by complexation with $BF_3{\cdot}Et_2O$ (12 eq.).

The presence of BDY1 was confirmed by measuring the ground state UV-visible absorption and fluorescence emission spectra, Figure 3.1.1. The characteristic BODIPY profile can be observed with a band maximum at 507 nm.

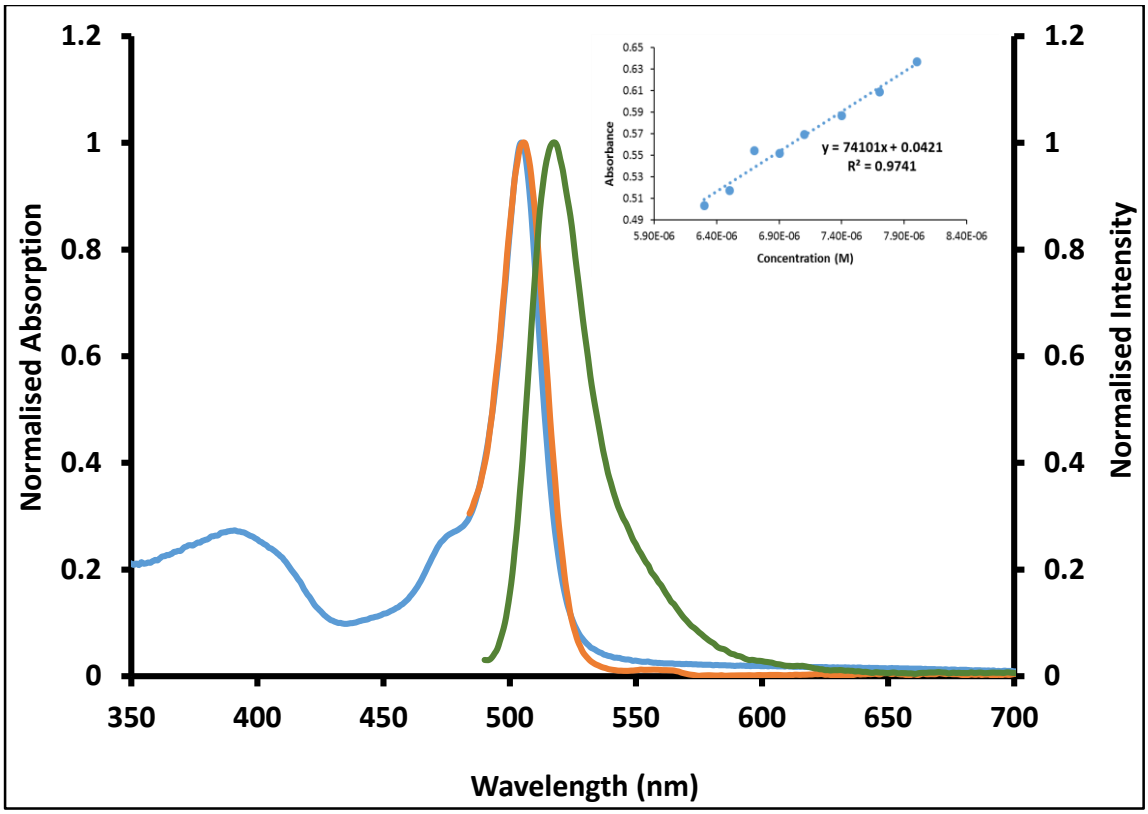

Figure 3.1.1: Normalized absorption (blue), excitation (orange) and emission (green, λ_{exc} 480 nm) spectra of BDY1. Corner inset showing the absorption coefficient calculation (summarized in Table 3.1.1) from spectra measured in THF.

A high ε value was calculated for the main absorption band with a value of 74100 $M^{-1}.cm^{-1}$, Table 3.1.1. When excited at either the S_1 or S_2 states, an intense absorption and emission band are observed with good mirror symmetry and the small Stokes shift, which are typical of BODIPY dyes. No fluorescence is observed from the S_2 state, due to relative rate of internal conversion to the S_1 state[145]. Moreover, in solution the product displayed an intense visible fluorescence in the presence of a hand held UV lamp, and was even visible under ambient solar radiation, Section 3.4. The ϕ_F value was determined to be 0.45 (i.e. 45%) in THF.

The fluorescence lifetimes (τ) values for the lowest lying energy state of BDY1 are displayed in Figure 3.1.2 which were obtained by fitting a dual exponential on the experimental decay curve with the main component having a value of 2.58 ns, as reported in literature[145].

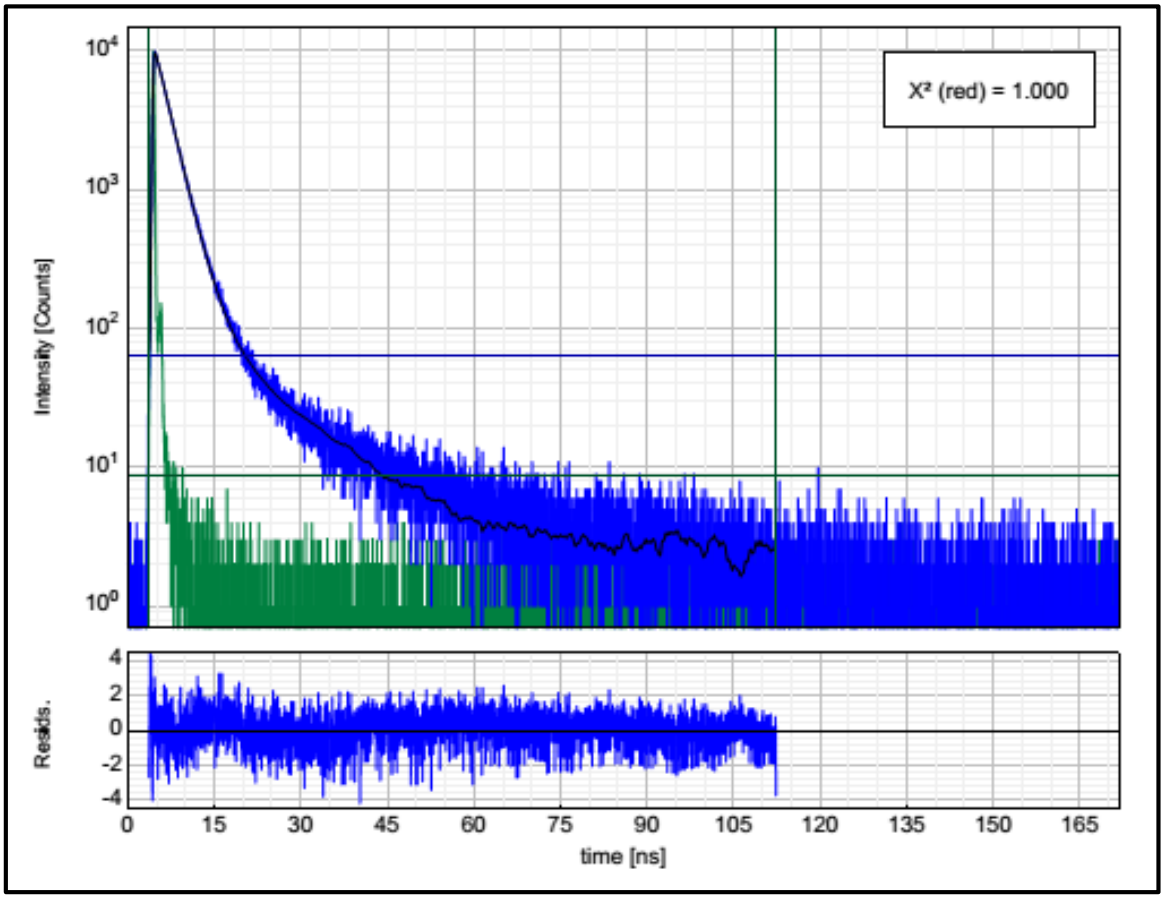

Figure 3.1.2: Exponential decay curve found for the ethynyl BODIPY measured in ethanol. Residuals indicated below. Excitation at 518 nm.

The ^{1}H-NMR data for this compound displayed peaks integrating to a total of nineteen protons. The two singlet peaks at 1.40 ppm and 2.55 ppm integrating to six protons each, can be assigned to the methyl group protons. A third singlet is observed at 3.18 ppm and can be attributed to the

single proton of the ethynyl functional group. A fourth singlet at 5.98 ppm indicates the presence of the 2 and 6-core positioned protons. A set of two doublets, integrating to two protons each, belong to the phenyl hydrogen atoms. CHNS elemental analysis afforded data slightly lower than expected possibly due to adsorbed water. BODIPY dyes are not known for their affinity to water which is often accumulated over extended periods of time.

3.1.2. 4,4-difluoro -8-(4-ethynylbenzene)-4-boro-3a,4a-diaza-*s*-indacene (BDY2)

For comparison purposes a second unsubstituted version of the ethynyl BODIPY was synthesized using pyrrole by following the water precipitation method[53] as described in **Section 1.2.2** with the pathway shown in **Scheme 3.1.2.** This method affords greater control over polymerization when pyrrole is used compared to the TFA method.

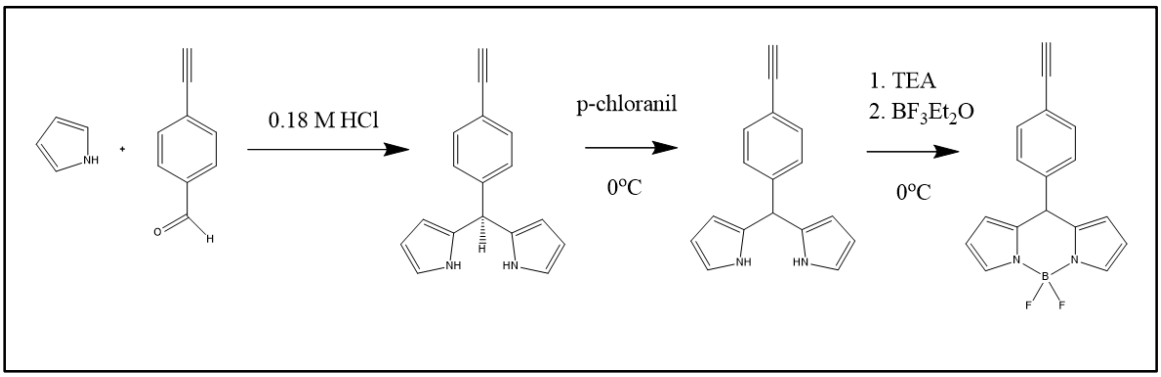

Scheme 3.1.2: An HCl catalyzed method for the selective synthesis of the ethynyl functionalized pyrrole BODIPY (BDY2).

This procedure is analogous to the previous method with the exception of the first step. An aqueous HCl (0.18 M) solution was prepared alongside 4-ethynylbenzaldehyde (0.15 M). When

the insoluble pyrrole (2 eq.) was added to the stirring aqueous HCl solution a microemulsion formed. The addition of the 4-ethynylbenzaldehyde to this solution causes the resulting dipyrromethanes to precipitate out as it is catalyzed by the HCl at the interface between the hydrophobic pyrrole and water layers. The product was extracted by filtration and washed with PET followed by deionized water and subsequently dissolved in an. DCM and degassed. The remaining steps have already been described in Section 3.1.1 with the product forming appreciably with a 70% yield.

The first level of characterization was carried out by measuring a UV-visible absorption spectrum in toluene, Figure 3.1.2., where the main absorption band lies at 507 nm. The characteristic broad shoulder due to the 0-1 vibrational band can be observed in the 460–480 nm range.

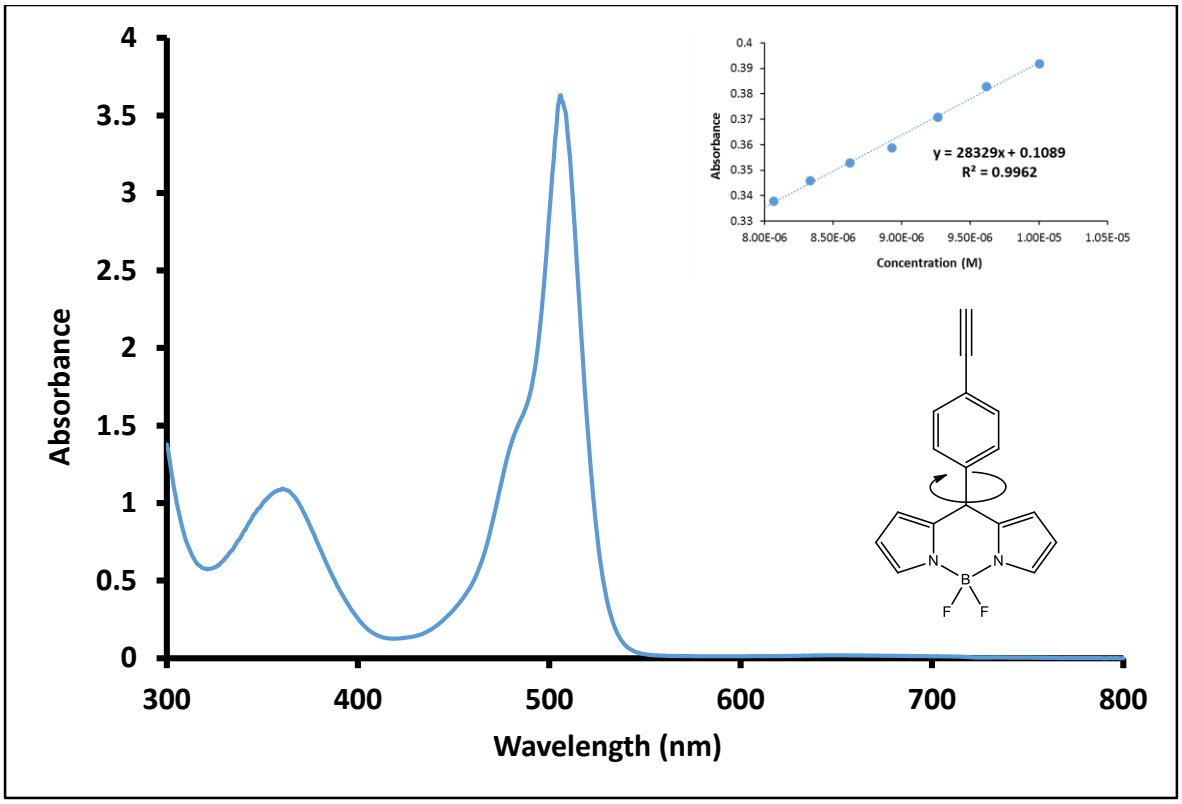

Figure 3.1.3: Ground state absorption spectrum for BDY2 (toluene). The inset diagram displays the calculation for the ε value (THF) and the rotational motion experienced by the ethynylphenyl group.

The ε value for the compound decreases dramatically from 74100 to 39000 $M^{-1}.cm^{-1}$, **Table 3.1.1**, in the absence of methyl groups at the 1, 3, 5, 7-positions. The now freely rotating phenyl ring dissipates the absorbed energy through the rotational motion of the phenyl ring which negates the fluorescence intensity[62]. This effect is lifted in the solid state where rotation of the phenyl ring is hindered and a slight fluorescence can be observed under ambient solar radiation. The images captured for all synthesized BODIPY dyes under UV lamp exposure and solar radiation are provided in **Figure 3.4.1.**

The ^{1}H-NMR spectrum integrates to a total of eleven protons with four doublet and two singlet peaks. The doublets at 6.63-6.60 and 6.99-6.95 ppm, and 7.61-7.58 and 7.72-7.69 ppm, correlated to two protons on the BODIPY core and two protons at the phenyl group, respectively. Two singlet peaks at 3.28 ppm, associated with the ethynyl proton, and 7.99 ppm, for core set of protons, integrating to two protons each were also observed. CHNS elemental data gave values within a ± 0.2% error margin.

3.1.3. 4,4-difluoro-1,3,5,7-tetramethyl-8-(methyl benzoate)-4-boro-3a,4a-diaza-*s*-indacene (BDY3)

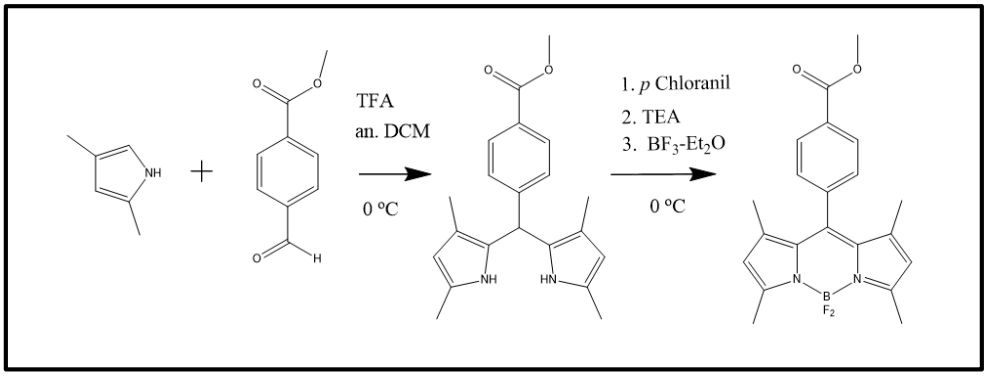

Scheme 3.1.3: The synthesis of BDY3.

The synthesis of BDY3, with a methyl ester functionalization at the meso-position, was carried out following the same procedure and conditions as described in section 3.1.1, giving the product in 61% yield. A similar absorption spectrum, Figure 3.1.4, was observed with the main absorption band (red) at 507 nm. The mirror image with the emission band (blue) at 519 nm suggests that the

ground and excited states have similar geometries. There is a small Stokes shift of 12 nm after excitation at 480 nm, with a ϕ_F value of 0.45 in EtOH.

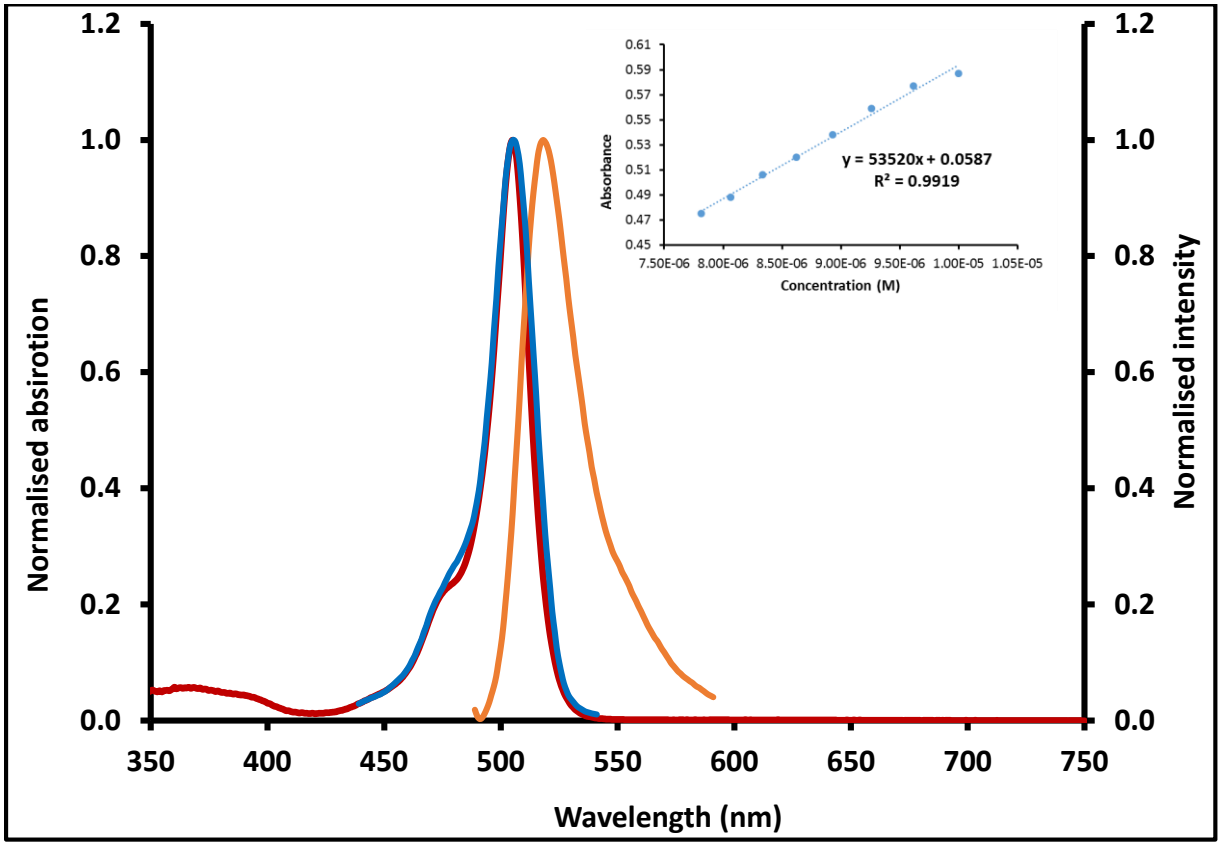

Figure 3.1.4: Ground state absorption (red) spectrum of BDY3 with the excitation (blue) and emission (orange, λ_{exc} 480 nm) run in toluene. A linear plot for the calculation of the ε value (THF) is presented as an inset.

The ^{1}H-NMR spectrum was comparable to that of the structurally similar BDY1, Scheme 3.1.1. The peaks that lie at 1.38 and 2.58 ppm can again be readily assigned to the methyl group protons. A singlet peak at 4.00 ppm integrating to three protons is consistent with the methyl group protons attached at the ester position. A second singlet integrating to two protons at 6.01 ppm can be

ascribed to the lone hydrogens at the core 2, 6-positions. Two doublets at 7.44-7.42 ppm and 8.21-8.20 ppm can be assigned to the phenyl group protons. The elemental analysis of this compound was found to be consistent with the presence of three additional water molecules. The τ value of BDY3 was fitted with a dual exponential, **Figure 3.1.5**, and the main component was found to have a value of 2.26 ns, similar to that of BDY1.

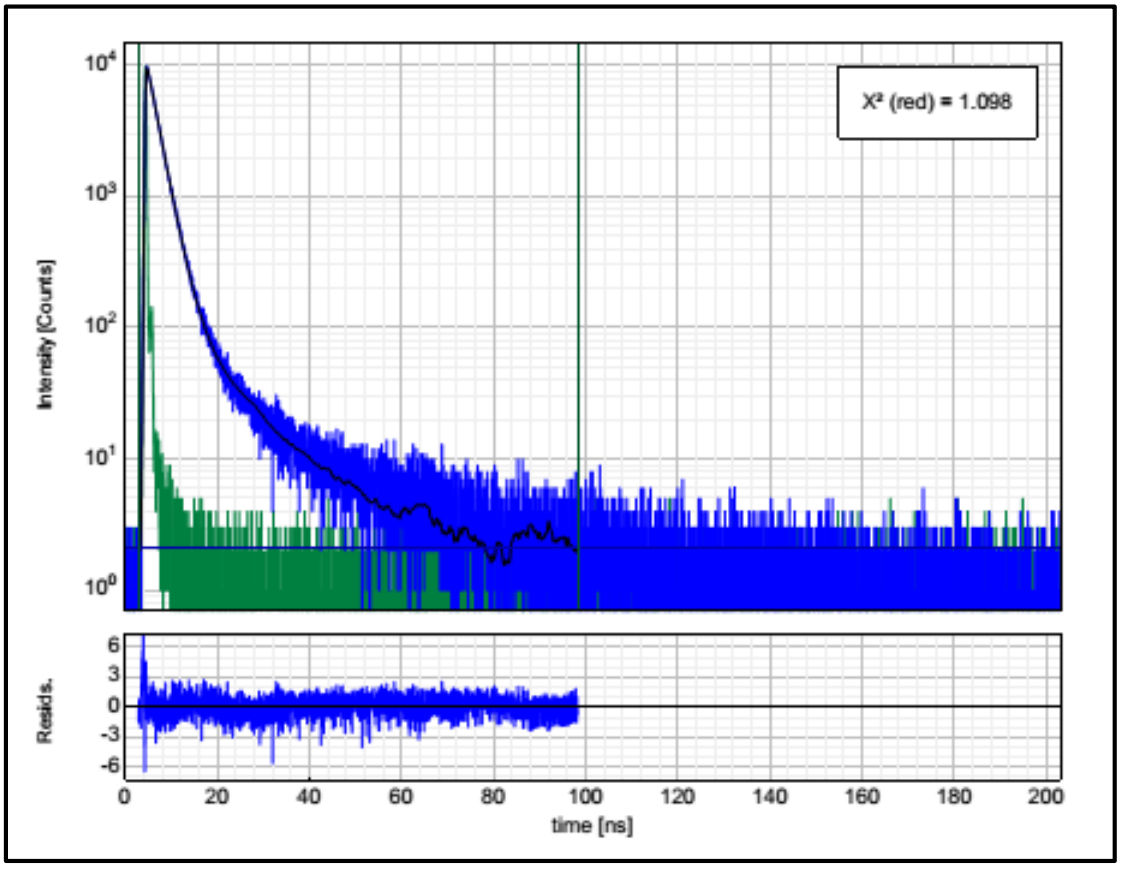

Figure 3.1.5: Experimental fluorescence decay curve for BDY3 in THF with residuals (λ_{exc} 519 nm).

3.2. Iodination of ethynyl and ester functionalized BODIPYs

3.2.1. Synthesis and characterization

Most BODIPY compounds possess an inherently low $^1O_2$ quantum yield (ϕ_Δ) value owing to the absence of a heavy atom to enhance the rate of ISC. This was addressed by halogenation with Iodine atoms at the 2, 6-positions of the BODIPY core. MO calculations, **Section 4.1**, have demonstrated that there is significant localization of electron density at the 2, 6-positions thus favouring electrophilic substitution reactions[76]. The synthetic pathways outlining this procedure for BDY1 and 3 are shown in **Scheme 3.2.1**, respectively, to form IBDY1 and IBDY3. This resulted in a red shift of the main absorption band to a longer wavelength resulting from the extension of the π-conjugation, due to the presence of the lone pairs on the iodine atoms.

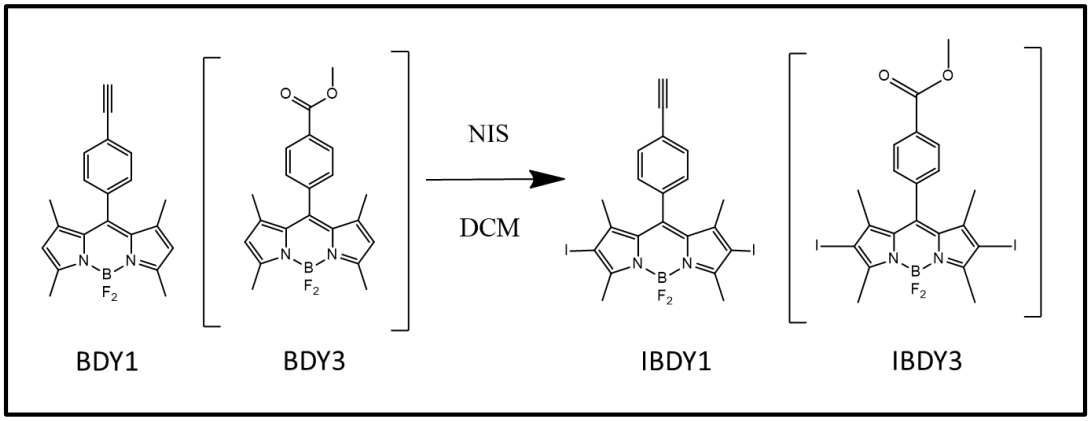

Scheme 3.2.1: Synthetic procedure for the iodination at the 2, 6-positions of BDY1 and BDY2. Reaction carried out under Ar gas.

The iodination procedure was carried out in an. DCM at room temperature in the presence of *N*-iodosuccinimide (3 eq.). The reaction was left to stir overnight under an Ar atmosphere protected

from light, this was carried out to reduce the risk of degradation by $^1O_2$ formation. The final product was isolated using flash column chromatography with a toluene eluent for IBDY1, in 83% yield, and a 1:1 ethyl acetate:hexane eluent for IBDY3, in 81% yield.

The ground state UV-visible absorption spectrum for IBDY1 and IBDY3 were recorded in toluene and are shown in **Figure 3.2.1**. A bathochromic shift of the $S_0 \rightarrow S_1$ transition is observed for both dyes. For IBDY1 there is a 31 nm red shift of the main spectral band relative to that of the starting BDY1, so the band maxima lies at 538 nm. For IBDY3, a slightly larger red shift of 35 nm was observed, and the band maxima lies at 542 nm.

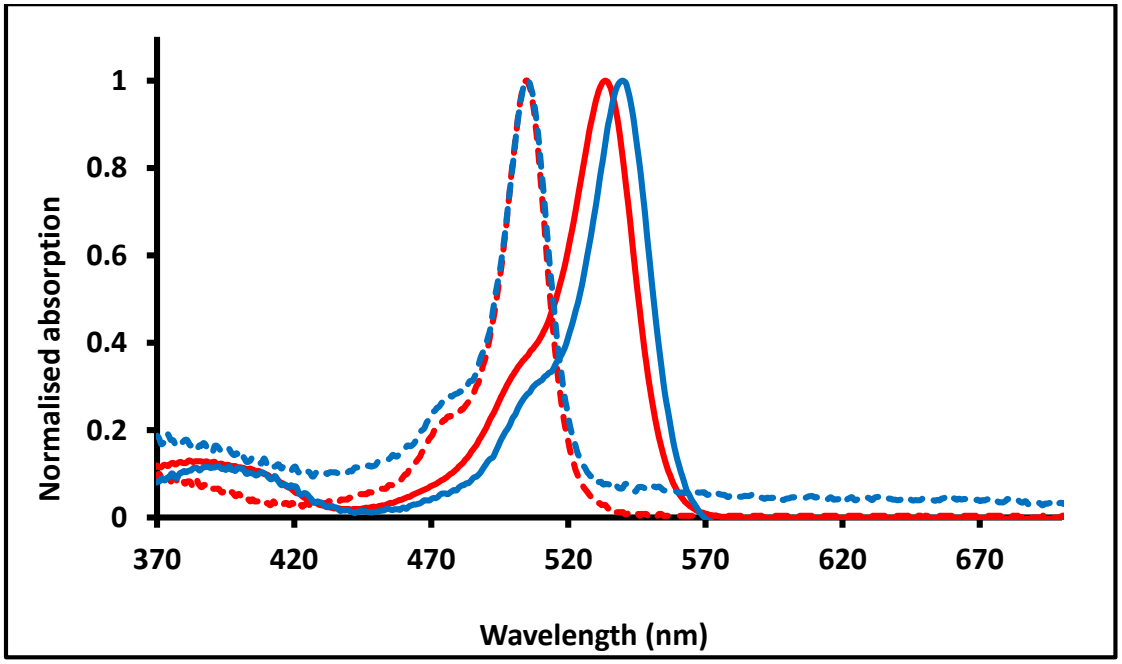

Figure 3.2.1: Ground state absorption spectra in toluene showing the wavelength shift from BDY1 (dashed red) to IBDY1 (red) and BDY3 (dashed blue) to IBDY3 (blue).

These changes arise from the extension of the π-conjugation due to the lone pairs on the iodine atoms. This is consistent with a decrease in HOMO-LUMO gap of the π-system. The reasons for this are discussed in greater detail **Section 4.2.1**. For both BODIPYs, the results are in line with those that have been reported previously in the literature[146,147].

To confirm the sites of iodination ^{1}H-NMR spectra were recorded for both BODIPYs in deuterated chloroform ($CDCl_3$). The regions of interest are the singlet peaks at 5.98 ppm for BDY1 and at 6.01 ppm for BDY3, since these can be assigned to the protons at the 2, 6-positions and are observed to completely disappear in the spectra of IBDY1 and IBDY3. The introduction of the iodine atoms caused no significant changes in the chemical shifts of the other peaks (no more than 0.2 ppm) in both cases. The differing functionalities at the out of plane meso-position have very little effect on the observed chemical shifts.

3.2.2. Singlet oxygen studies

The singlet oxygen quantum yields of BODIPY dyes have been extensively studied and are well documented[148,149]. One of the goals of this study was to identify BODIPY dyes that can generate $^{1}O_2$ making them suitable for future applications in areas such as PDT and PACT. A comparative method, discussed in **Section 1.1.3**, was used for the measurements of $^{1}O_2$ and were carried out using a known $^{1}O_2$ producer and quencher, respectively Rose Bengal and DPBF.

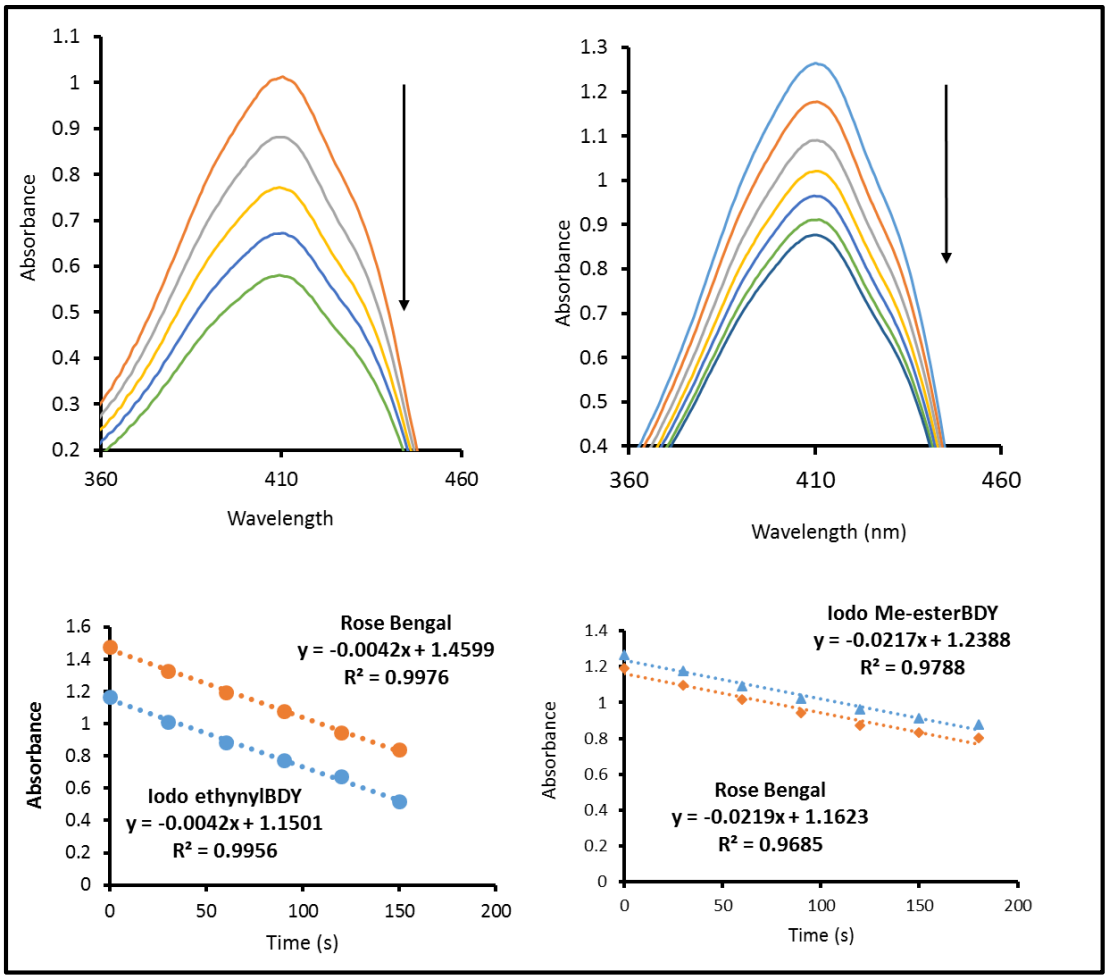

Figure 3.2.2: Decrease in DPBF absorbance over 30 s intervals in the presence of Rose Bengal as the ϕ_Δ standard. Excitation was carried out at 536 nm for IBDY1 and 542 nm for IBDY2 (EtOH).

Pulsed monochromatic laser light (20.0 Hz) was used to excite the samples at 536 and 542 nm for IBDY1 and IBDY2, respectively. Irradiation in 30 s intervals resulted in a linear decrease in the concentration level of the DPBF singlet oxygen scavenger. This is due to the type two photo-oxidation reaction, **scheme 1.1**, indicating the production of the reactive oxygen species. A plot of absorbance vs time for both the sample and standard appears in the lower portion of **Figure 3.2.2.**

The relative rates of their decrease when compared with the ϕ_Δ standard of Rose Bengal in EtOH yielded values of 0.86 for IBDY1 and 0.88 for IBDY3.

3.3. Sonogashira Coupling and a Novel BODIPY dye

3.3.1. Sonogashira coupling towards a series novel BODIPY dye

As stated in **Section 1.4**, the initial aim of this research project was the development of a series of novel dyes through the use of halide coupling between the ethynyl functional group on a BODIPY and, respectively, a brominated diaminophenyl, aminophenyl and phenyl ring. The amino groups provide the prerequisite for an amide linkage with, for example, a carboxylic acid or ester functionalized molecule, nanoparticle or for the coordination site to a metal analyte to act as a sensor. This research trajectory subsequently changed with the unexpected formation of a novel BODIPY dimer, **Scheme 3.3.1**.

Amino bearing compounds are known to be electron donating and therefore effectively render the leaving group, a bromine atom in this context, inactive. This was addressed by di-tert-butyl dicarbonate (Boc_2O) protection of the amine groups which efficiently removes the electron density localized on the ring away from the halogen group. Boc_2O protection was carried out via a green method using an organo-catalyst, guanidine hydrochloride (GuHCl) and Boc_2O in EtOH[150], **Scheme 3.3.1**.

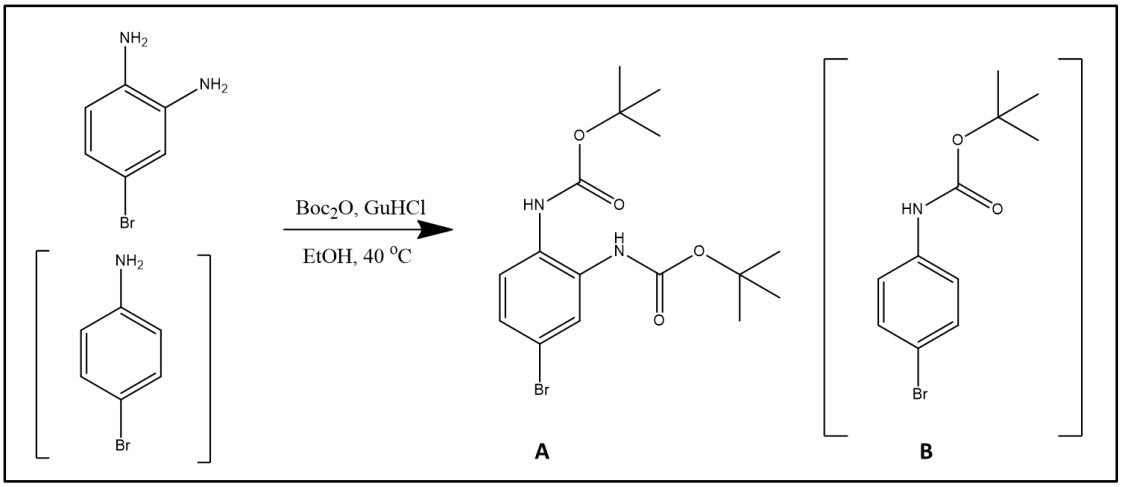

Scheme 3.3.1: The Boc_2O protected diamine (A) and amine (B) groups formed by using guanidine hydrochloride as a green organo-catalyst. The synthesis was carried out using procedures described in the literature[150].

The Boc_2O protected amine compounds A and B were characterized by NMR spectroscopy, data in Section 2.3.6, with the subsequent steps for their attachment to the ethynyl and pyrro-ethynyl BODIPYs shown in Scheme 3.3.2 with the expected target products. The effect of having amine groups at the extended meso-position was studied by having a third unsubstituted target compound that was formed by using iodobenzene.

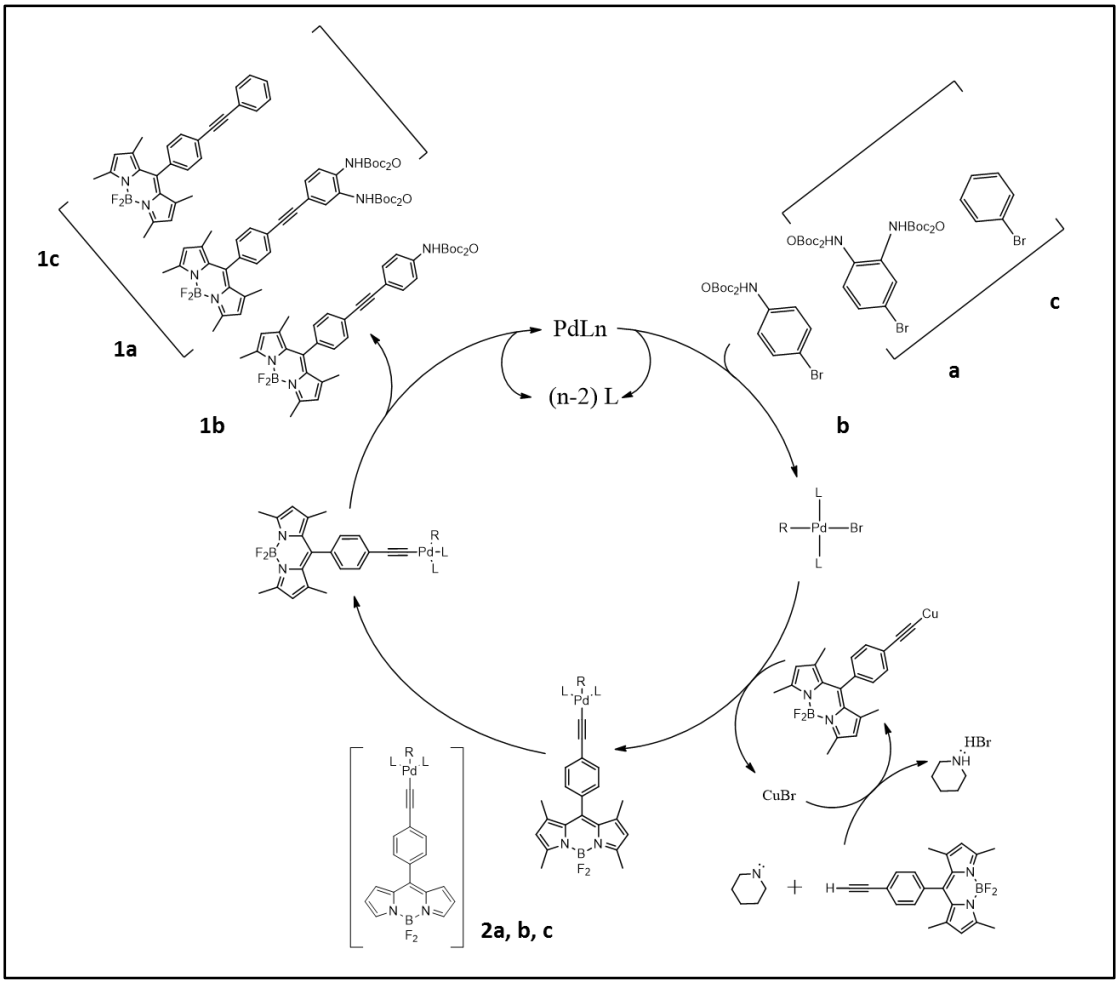

Scheme 3.3.2: The Sonogashira coupling cycle of Boc_2O protected groups with the BDY1 (Scheme 3.1.1) using $PdCl_2(PPh_3)_2$ as the catalyst, a CuI co-catalyst and piperidine as the amine base (1a, b, c). A derivative using the BDY2 is also proposed (2a, b, c).

All reagents and glassware were oven dried over-night and allowed to cool in the presence of N_2 gas. The water sensitive coupling reaction was carried out under Ar gas with a palladium catalyst and CuI co-catalyst. The mixture was heated in an. THF to reflux and held for a 20 h period before filtration and separation.

After extensive experimentation with the Sonogashira coupling reaction it became apparent that the synthetic strategy requires either improved control over the reaction conditions and/or the use of different reagents. A similar Sonogashira coupling reaction was carried out by Ulrich and Ziessel[58] for a meso-phenyl substituted BODIPY with an ethynyl group at the para-position with various bromo-substituted heterocycles. The authors reported that a homocoupling reaction was favoured by the use of low valent palladium(0) as the catalyst, since similar homocoupling reactions had been reported for reactions with other ethynyl-grafted compounds[151,152]. A similar serendipitous synthesis of a dimer of BDY1 linked at the para-positions of the meso-phenyl rings with a diethynyl bridge (AxBDY) was repeatedly achieved, Scheme 3.3.3, with no sign of the desired target compounds.

3.3.2. Synthesis and characterization of an axial BODIPY dimer (AxBDY and IAxBDY)

Ulrich and Ziessel[58] and Guo Fan Jin et al.[153] have previously reported the homocoupling reaction of an ethynylphenyl-functionalized BODIPY with ethyl groups at the 2, 6-positions under similar Sonogashira coupling reaction conditions. The long diethynyl bridge results in both chromophores absorbing at the same wavelength with a greater ε_{max} value when compared to that of the BDY1 monomer. This was also recognized by Guo Fan Jin and co-workers[153] who focused on using dyad systems to increase the light harvesting capabilities of the BODIPY chromophore for use in solar cells. In this study, a halogenation reaction at the freely available 2, 6-positions of AxBDY was carried out with NIS, to explore whether a high ϕ_{Δ} value would be obtained for the IAxBDY target compound.

Scheme 3.3.3 outlines the method used for the synthesis of AxBDY and the steps for the subsequent iodination at both BODIPY chromophores, Scheme 3.2.1. The air sensitive Sonogashira coupling reaction was carried out in oven dried glassware and an. THF. This was prepared on sodium wire with benzophenone as the indicator. Once the solution turned purple in colour the solvent was distilled onto 4 Å molecular sieves and kept in the dark under an Ar environment.

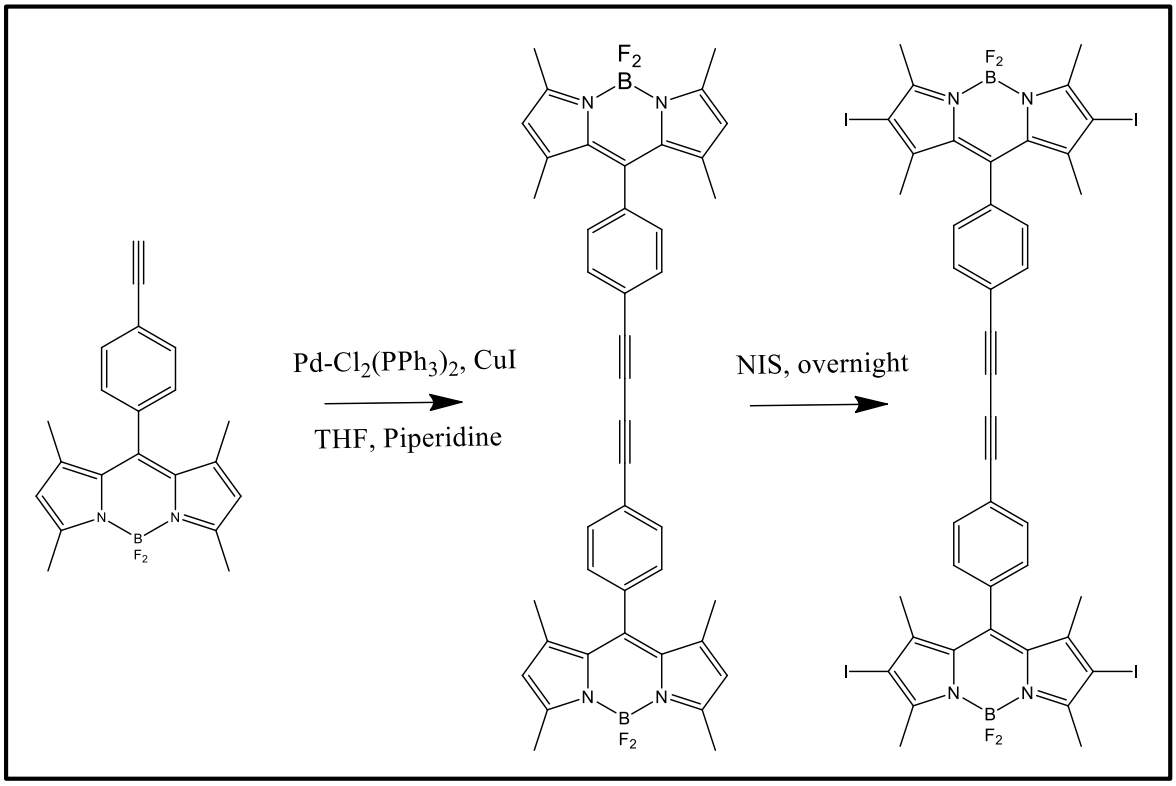

Scheme 3.3.3: Pathway outlining the Sonogashira coupling reaction for the synthesis of AxBDY. The functionalized with iodine atoms at both positions BODIPY core is also depicted resulting in the formation of IAxBDY. The reaction was conducted under Ar atmosphere.

Initially, BDY1 was added to a dry reaction vessel containing small amounts of the $PdCl_2(PPh_3)_2$ and CuI. The reagents were degassed with Ar in the solid state followed by addition of an. THF and

piperidine (2 eq.). The reaction was left to stir at reflux overnight in the dark yielding a black solution. After evaporation the product was purified by column chromatography with a 1:1 ethyl acetate: hexane mixture used as the eluent. The mass spectrum contains a single peak at 694.30 m/z aligned with the calculated molecular weight of 694.38 m/z. In the FTIR spectrum, the narrow vibrational C–H stretch at 3250 cm^{-1} belonging to the ethynyl group had completely disappeared. The UV-visible absorption spectrum, **Figure 3.3.3** which is more typical of a standard BODIPY, displayed a band maximum peaking at 507 nm identical to that of BDY1, **Figure 3.1.1**. The slight shoulder at ca. 477 nm can be ascribed to the vibrational (0-1) transition and there is a weaker band envelope at ca. 350 nm due to the $S_0 \rightarrow S_2$ (0-0) transition.

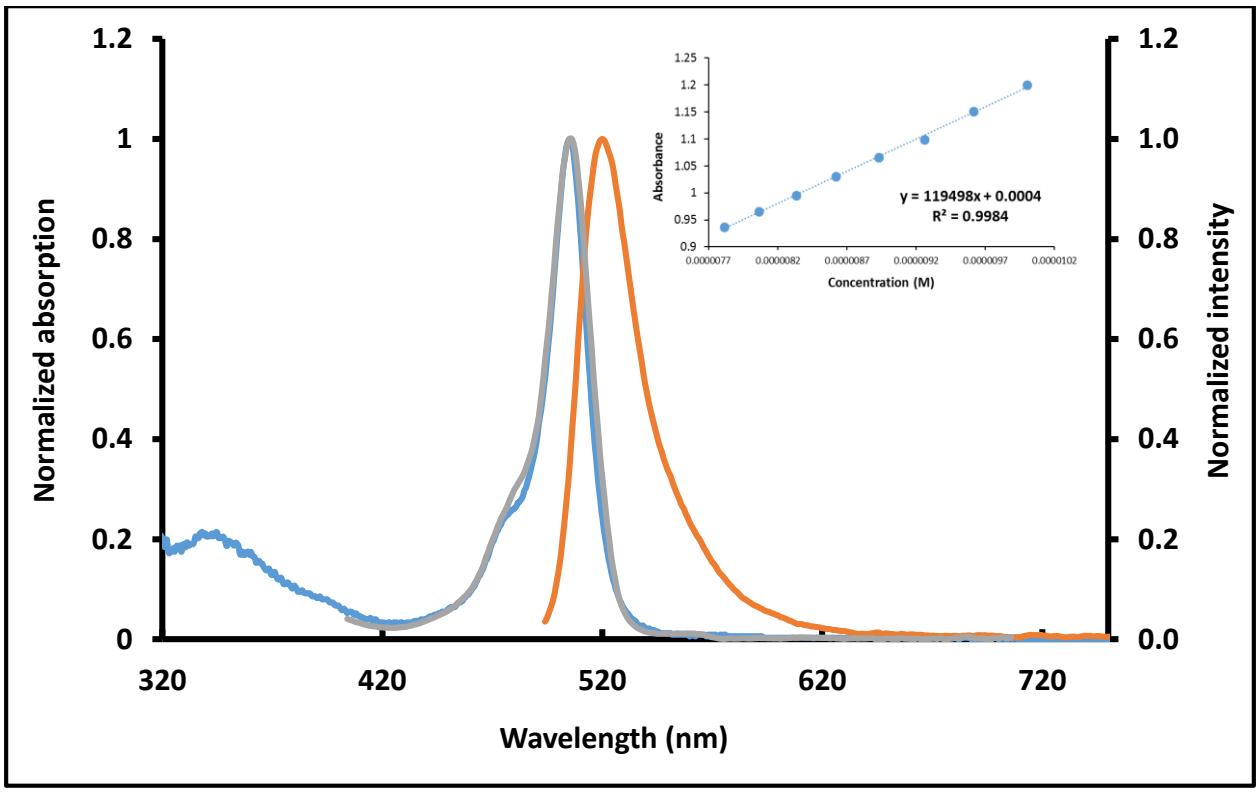

Figure 3.3.3: Absorption (blue) and fluorescence spectra obtained (λ_{exc} 480 nm) for AxBDY at room temperature in toluene. A linear plot showing the calculation of the molar ε (THF) is also displayed.

The emission maximum lies at 522 nm (excitation at 480 nm) is consistent with a small Stokes shift of 15 nm, a difference of only 3 nm from the monomer dye, and there is good mirror symmetry between the emission and excitation spectra (grey). The orthogonal arrangement of the chromophores of AxBDY prevent the dipole moments and transition dipoles from coupling and hence there is no extension in the π-conjugation and no shift in the band maximum to a longer wavelength. One consequence of the axial dimer formation is a dramatic increase in the ε value measured at 119000 $M^{-1}.cm^{-1}$ relative to the BDY1 value of 74100 $M^{-1}.cm^{-1}$ as both chromophores are involved in the absorption. The ϕ_F value was lowered to 30% in THF.

There was a total integration of thirty six protons in the ^{1}H-NMR analysis. The most noteworthy aspect is the removal of the C–H ethynyl peak at 3.18 ppm. The singlet peaks at 1.36 and 2.56 ppm, each integrating to twelve protons, relate to the methyl hydrogens on both chromophores. These peaks showed very minor chemical shifts, a ca. 0.02 ppm difference, when compared with BDY1 owing to the large displacement of the two chromophores. Larger differences were observed for the doublets of phenyl protons at 7.42-7.40 ppm (*J* = 8.0 Hz, 4 protons) and 8.19–8.17 (*J* = 8.0 Hz, 4 protons). There is a 75% increase in the extent of their coupling and a 0.5 ppm peak shift with respect to BDY1.

The τ values are shown in **Figure 3.3.4**. There is a small decrease to 1.61 ns relative to the value obtained for BDY1. It can be assumed that the changes in these values result from the different rotational axes of the AxBDY, which lies through two BODIPY chromophores and the acetylene bridge, by comparison with that of BDY1 which passes through the phenyl ring only.

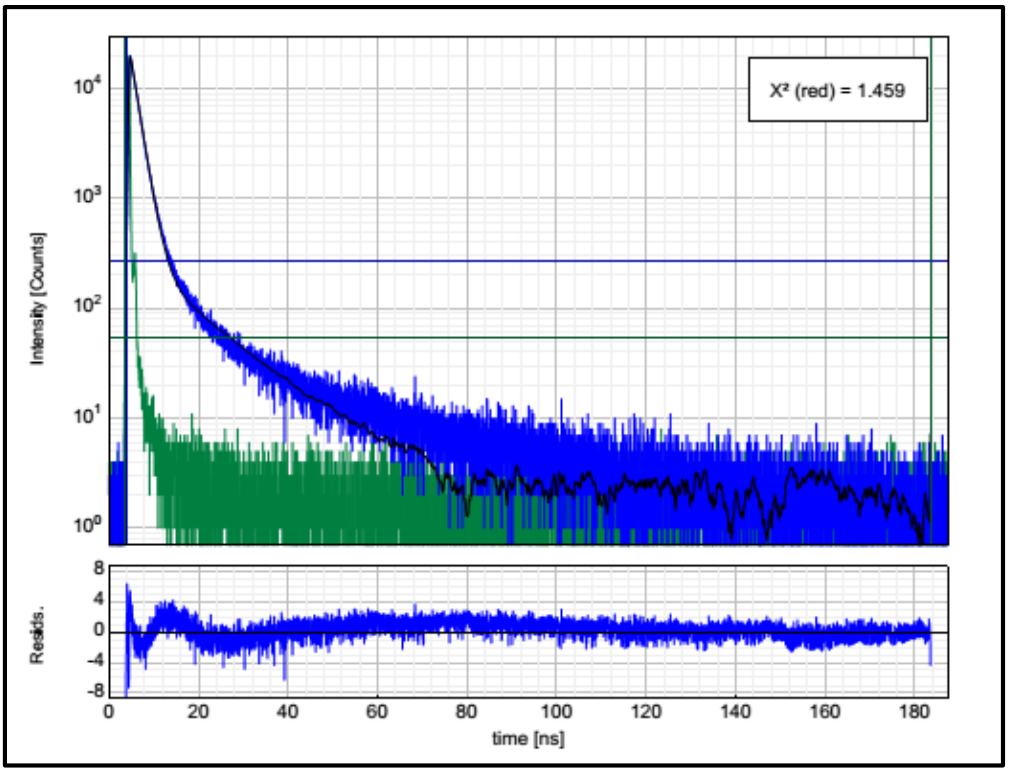

Figure 3.3.4: Fluorescence decay profile for AxBDY (ethanol) with residuals (λ_{exc} 522 nm).

3.3.3. Iodination and singlet oxygen studies of axial BODIPY dimer (IAxBDY)

It was postulated that the attachment of iodine atoms at the four sites available on AxBDY would improve the already high ϕ_{Δ} quantum yield value. The synthetic procedure was followed as presented in **Section 2.3.7** by varying the mole ratio to account for the extra occupancy sites, **Scheme 3.3.2**. NIS (6 eq.) was added to a stirring solution of AxBDY (1 eq.) and left to stir overnight in the dark. The UV-visible absorption spectrum was used as the first level of characterization, **Figure 3.3.5**.

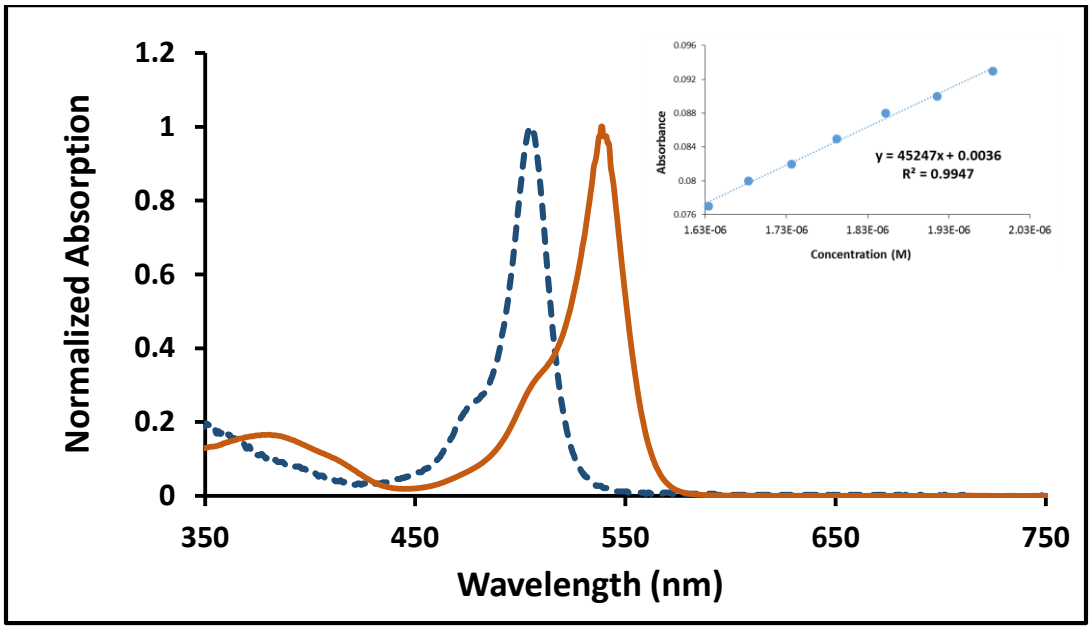

Figure 3.3.5: Shift in absorption maxima observed for the AxBDY (dashed blue) to IAxBDY (orange) with a linear plot showing the ε (THF).

The main absorption band shifts from 507 to 541 nm relative to the spectrum for AxBDY, due to the addition of four iodine atoms, two at each chromophore. The elemental analysis was carried out and was found to be consistent with an additional mole of adsorbed water. The parent peak at 1203 m/z in the mass spectrum confirmed the presence of IAxBDY. A significant lowering of the ε value was observed from 119000 to 45300 $M^{-1}.cm^{-1}$.

A study on the generation of $^1O_2$ by IAxBDY upon photosensitization was carried out. It was hypothesized that with the increased number of iodine groups would result in a larger ϕ_Δ quantum yield value due to the heavy atom effect. The results are presented below in **Figure 3.3.6**. As can be seen the efficiency is increased only slightly from 0.86 to 0.88 with respect to IBDY1.

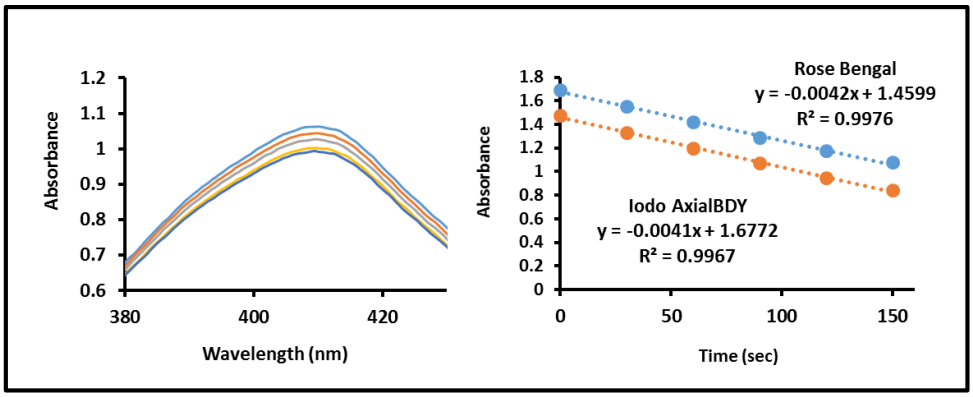

Figure 3.3.6: $^1O_2$ degradation over 30 sec intervals with Rose Bengal as the standard and DPBF as the $^1O_2$ scavenger molecule.

The presence of the second chromophore did not increase the ϕ_Δ quantum yield value to the extent anticipated. While the presence of two additional iodine groups enhances the rate of ISC their effect is not reflective of the relative ε value, which is proportional to the amount of absorbed photons rather than the efficiency of T_1 state formation. The effect is also dependent on the rate of other processes like non-radiative decay, which may be enhanced by the larger dyad structure.

3.4. Summary of photophysical properties

Throughout the research the different BODIPYs displayed the expected photophysical properties, Table 3.1.1. However, the changes in the ε values showed no logical progression. Solvent effects play a large role in this regard since the interactions between them can affect the ability of the compound to absorb light. This can be attributed to the effects on molecular vibration where incident photons are considered. All BODIPYs bearing a 1, 3, 5, 7-tetramethyl substitution pattern have a main absorption band in the ca. 508 nm region, as does BDY2, which has an unsubstituted core.

Table: 3.1.1. Photophysical data for synthesized BODIPY compounds

Compound	λ_{abs}	λ_{em}	Stokes shift	ε	ϕ_F	ϕ_Δ
BDY1	506	518	12	74100	0.45	-
IBDY1	538	-	-	39000	-	0.86
BDY2	508	-	-	28000	-	-
BDY3	507	519	12	54000	0.45	-
IBDY3	542	-	-	73000	-	0.87
AxBDY	507	522	15	119000	0.3	-
IAxBDY	541	-	-	45300	-	0.88

* ϕ_F data was obtained in EtOH against the standard Rhodamine 6G (ϕ_F^{std} = 0.94 in EtOH, cross over λ = 510 nm). The ε ($M^{-1}cm^{-1}$) values were obtained in THF, the absorption, excitation and emission values in toluene.

Iodination of BDY1, BDY3 and AxBDY results in a ca. 38 nm red shift of the main absorption band due to the extension of the π-conjugation system. A small increase is observed in the ϕ_Δ quantum yield values of IAxBDY with the attachment of two additional iodine atoms. Images of all synthesized BODIPYs in solution were captured and are shown in Figure 3.4.1. Each compound was irradiated with solar (left) and UV-light (right). Under ambient solar conditions BDY1 and BDY3 display a slight green fluorescence indicating the efficiency of the compounds as light harvesters. This is even more pronounced under a UV stimulation where the BODIPY image become saturated by the green fluorescence. This is particularly true for AxBDY, since it has a higher ε value.

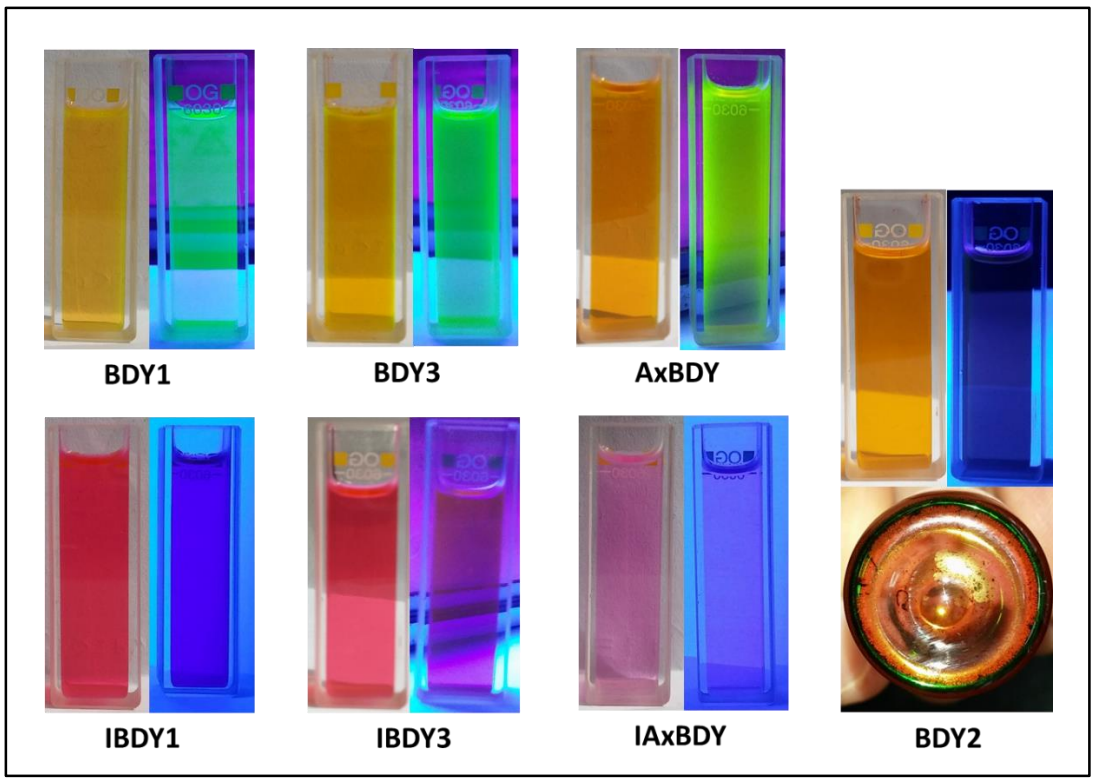

Figure 3.4.1: Images of Synthesized BODIPY dyes under solar radiation (left) and UV radiation (right). An image of BDY2 in its solid state is also shown.

IBDY1 and IBDY3 display no fluorescence emission under either of these conditions where the electronegative iodine atoms quench the fluorescence of the molecules. As pointed out in Section 3.1.2, BDY2 has no visible fluorescence due to the absorbed energy being dissipated by the unrestricted rotational motion of the meso-phenyl group[62]. However, in the solid state this vibrational motion is no longer observed and the fluorescence is switched "on" under ambient light.

CHAPTER FOUR

Molecular Modelling

4. Molecular Modelling

4.1. Molecular modelling parameters

Molecular modelling calculations have been used to elucidate trends in the predicted spectra and the electronic structures of the synthesized compounds (BDY1-3 and IBDY1, 3). All calculations were carried out at the Centre for High Performance Computing (CHPC) in Cape Town. Density functional theory (DFT) was used to carry out geometry optimizations using the Beck, three-Parameter, Lee-Yang-Parr (B3LYP) functional of the Gaussian09 program package[154] with 6-31G(d) basis sets. The B3LYP functional is a hybrid functional, since it exchange from semi-empiracal part Hartree-Fock (HF) theory with exchange and correlation calculated by DFT[155]. The electronic absorption properties were calculated under a time-dependent method (TD-DFT) with the Coulomb-Attenuated B3LYP (CAM-B3LYP) parameter, which includes a long range correction of the exchange potential. This accounts for the interelectronic separation by having an increased portion of the HF exchange which makes it more suitable for analyzing compounds when there is likely to be significant charge transfer in the electronic excited states. This is particularly important for AxBDY and IAxBDY where the two chromophores are separated by a diethynyl bridging moiety.

4.2. Electronic structure of BODIPY dyes

The rules for aromaticity set by Hückel are not consistent with the BODIPY chromophore as discussed in Section 1.2.1. Pseudo-aromatic properties are observed instead, since the BF_2 moiety holds the dipyrromethene ligand in a rigid conformation[45]. The angular nodal patterns of the BODIPY chromophore, which has similarities to an indacene plane when the boron atom is taken into consideration, are comparable to those of a parent $C_{12}H_{12}^{2-}$ hydrocarbon perimeter model.

This has a MO energy sequence of M_L = 0, ±1, ±2, ±3, ±4, ±5, 6 in ascending energy terms with regards to the magnetic quantum number, M_L, of the parent perimeter model. The inclusion of the BF_2 moiety into the indacene plane results in the degeneracy of the π-MOs being lifted due to the C_{2v} symmetry[156].

This type of cyclic polyene analysis was developed by Gouterman and Michl[157,158] to explain the absorption spectra of porphyrins and phthalocyanines and can be extended to the BODIPY structure. The BODIPY MOs, with nodal planes passing through the boron atom, remain largely unaffected with reference to those of the parent perimeter model. In contrast, the MOs around the horizontal nodal plane are significantly stabilized due to the increased electron density localized at the more electronegative nitrogen atoms and a stronger bonding interaction between the two pyrrole moieties. This type of study, as presented by Lu et al.[156], demonstrates the substantial lifting of the degeneracy of the HOMO and LUMO levels of the cyclic polyene, so that the main spectral band is almost completely dominated by the HOMO → LUMO one-electron transition.

4.2.1 BODIPYs and their iodination

The effect of structural modifications on the optical properties of the synthesized BODIPY dyes can be illustrated clearly by studying their MO energy levels. For comparison purposes, a model compound, IBDY2, was studied with two iodine atoms attached at the 2, 6-positions to the structure of BDY2. The main spectral bands of BDY1-3 and IBDY1-3 are dominated by the main HOMO → LUMO transitions with significant oscillator strengths, as would normally be anticipated for BODIPY derivatives. The MO coefficients of the HOMOs of BDY1-3 and IBDY1-3 are localized

symmetrically on either side of a nodal plane aligned with the short axis (through the boron atom and meso-carbon), **Figure 4.2.1**, while in contrast the LUMOs are aligned either side of a nodal plane aligned with the horizontal long axis. The formation of IBDY1 and IBDY3 via iodination results in a large stabilization of both the HOMO and LUMO due to the electron withdrawing properties of the halogen atoms. There is a narrowing of the HOMO–LUMO gap, due to a destabilization of the HOMO, which has large MO coefficients at the 2, 6-postions, **Figure 4.2.1**, due to the mesomeric effect associated with the lone pairs on the iodine atoms.

The LUMOs have large MO coefficients at the meso-position, **Figure 4.2.1**. This has no significant effect on the energies of the LUMOs of BDY1 and BDY3, due to the orthogonal arrangement of the phenyl rings with respect to the plane of the BODIPY core. The frontier π-MOs of BDY2 are lower in energy than those of its tetramethyl-substituted counterpart, BDY1, due to the effect of the weak electron donating properties of the methyl groups, **Figure 4.2.1.** For BDY1 and BDY3, both the HOMO and LUMO have significant MO coefficients at the 3, 5-positions, while the LUMOs have larger MO coefficients at the 1, 7-positions. The HOMO of BDY2 is stabilized relative to the LUMO, **Figure 4.2.3**, resulting in a significantly larger band HOMO–LUMO gap. The calculated MO energies for the iodinated analogue of this compound, IBDY2, demonstrate that the π-MOs are unevenly affected at the 2, 6-positions, since the LUMO is predicted to be stabilized, while the HOMO is destabilized. This results in a larger predicted red shift of the main spectra band, since the HOMO–LUMO band gap is significantly smaller, in comparison to that of BDY1. Under these circumstances, IBDY2 is predicted to have a more red-shifted absorption band, calculated at 437 nm, compared to those of IBDY1 and IBDY3 that are predicted to lie at 427 nm.

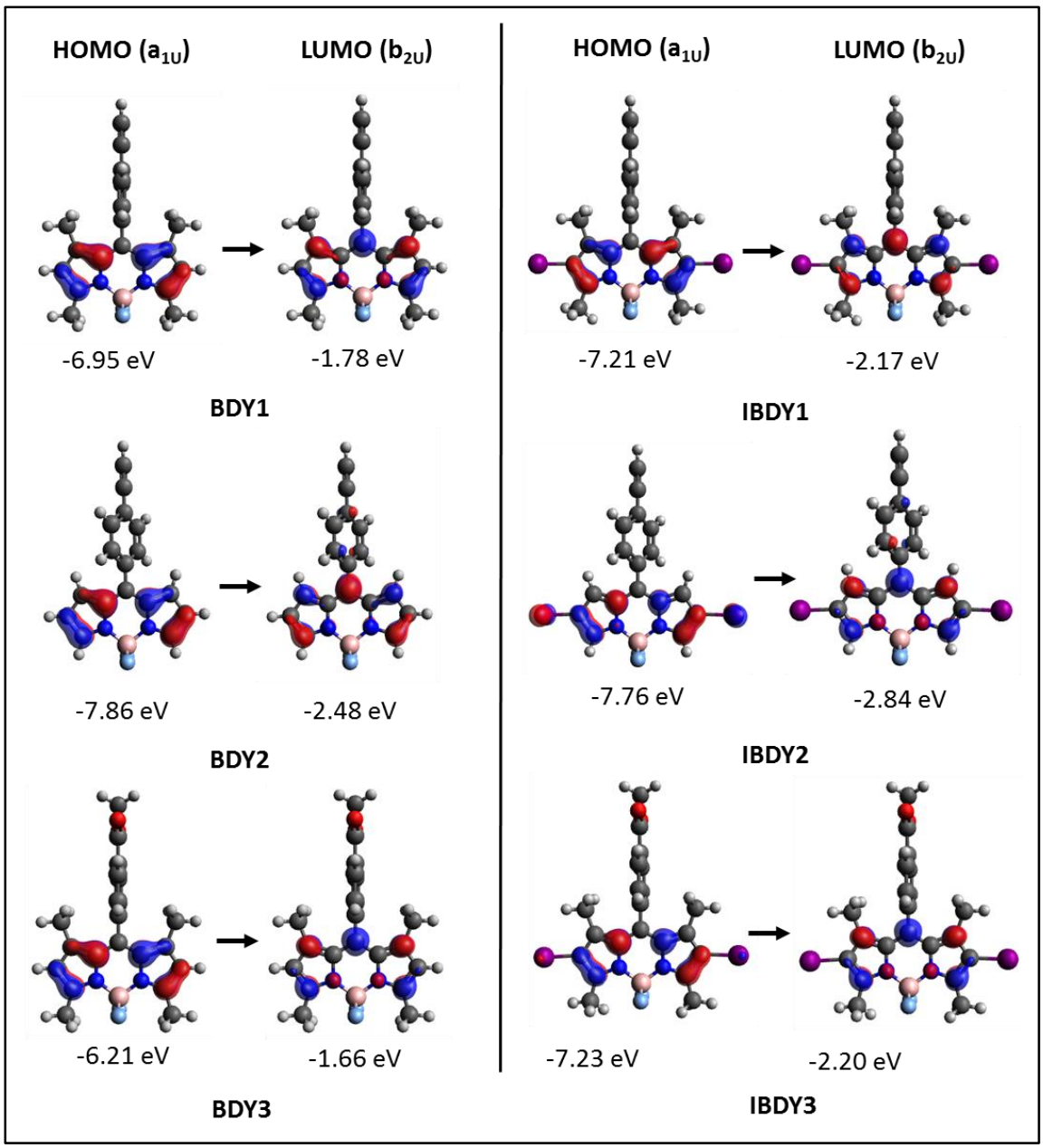

Figure 4.2.1: HOMO and LUMO diagrams (isosurface value of 0.05 a.u) for BODIPY dyes showing the major transitions associated with the main spectral bands in the visible region. All of the compounds were synthesized with the exception of IBDY2.

Table 4.2.1: TD-DFT calculated transitions for the BODIPY compounds BDY1 – IBDY3 with a B3LYP optimized geometries and CAM-B3LYP functional.

Compound	#	λ_{cal} (nm)	λ_{exp} (nm)	f_{cal}	Wavefunction
BDY1	S_1	407	506	0.54	H → L (96%); …
IBDY1	S_1	427	538	0.51	H → L (83%); …
BDY2	S_1	377	508	0.39	H → L (93%); …
IBDY2	S_1	437	–	0.52	H → L (54%); …
BDY3	S_1	389	507	0.54	H → L (96%); …
IBDY3	S_1	427	542	0.39	H → L (83%); …

* Oscillator strength (f_{cal}) with the TD-DFT predicted wavelengths (λ_{cal}) **and the experimentally observed** wavelengths (λ_{exp}). Percentage value for one electron transitions (1et) within each the excited states (#).

Considered next are the TD-DFT calculations for AxBDY and IAxBDY, Figure 4.2.2. These differ markedly from those of BDY1-3 and IBDY1-3, due to their dimer structures that result in near degenerate HOMO and LUMO levels. The HOMO and HOMO–1 of AxBDY are localized on each BODIPY chromophore at –7.01 eV, and for IAxBDY at –7.29 eV, resulting in transitions to the near degenerate LUMO and LUMO+1 at –1.90 eV for AxBDY, and –2.32 and –2.31 eV for IAxBDY. This explains why the extinction coefficient values for AxBDY and IAXBDY are approximately double those for the analogous monomer structures, since the band associated with the transitions between these orbitals have a significantly higher calculated oscillator strength, f_{cal}, than that predicted for the HOMO → LUMO transition of BDY1.

The HOMO–LUMO gap value for AxBDY is significantly larger than that of IAxBDY, Figure 4.2.3. This accounts for the observed red-shift of the main absorption band of IAxBDY at 541 nm, which is similar to the 538 nm maximum observed for IBDY1, Table 3.1.1. From an energetic standpoint,

there are large MO coefficients at the 2, 6-positions of one of the BODIPY ring moieties of AxBDY in the HOMO and HOMO–1, but in the LUMO and LUMO+1 levels they are entirely absent, since there is a nodal plane through the 2, 6-positions. The mesomeric effect associated with the lone pairs on the iodine atoms have a greater influence on the HOMO and HOMO–1 levels, resulting in a relative destabilization due to the large MO coefficients at the 2, 6-positions

The percentage values for the one-electron transitions that make the main contributions to the main spectral bands for AxBDY and IAxBDY, Table 4.2.2, are significantly different from those of BDY1-3 and IBDY1-3 due to the dimeric structures. Multiple one-electron transitions contribute significantly to the first two excited states, Table 4.2.2, since there are near degenerate HOMOs and LUMOs associated with the two BODIPY ring moieties. IAxBDY displays a broadly similar trend in its electronic distribution and in its excited states to those observed for AxBDY.

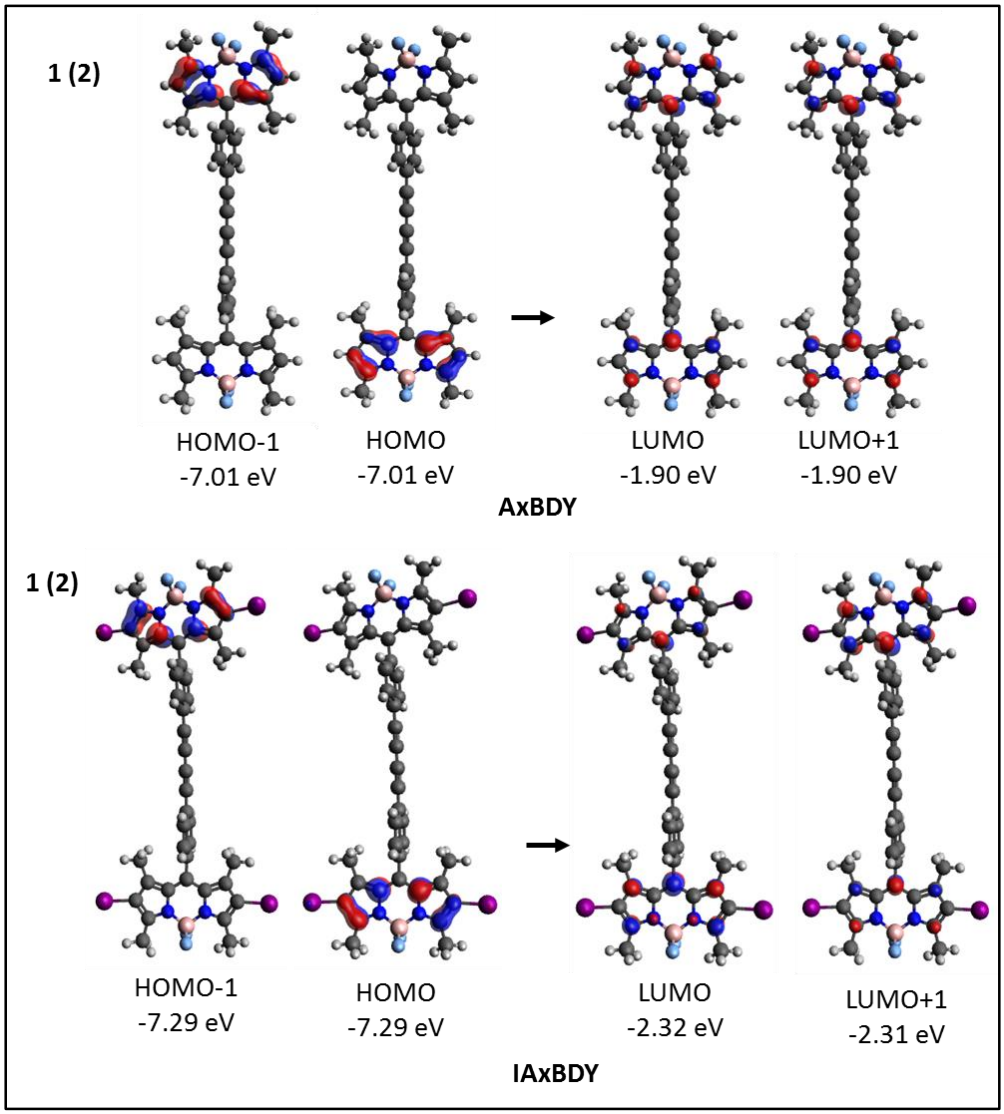

Figure 4.2.2: The MO diagrams (isosurface value of 0.05 a.u) for the near degenerate HOMOs and LUMOs that result for AxBDY and IAxBDY, due to their dimer structures. The diagrams also show the major transitions associated with the band maxima in the visible region.

Table 4.2.2: TD-DFT calculated transitions for the BODIPY compounds AxBDY and IAxBDY with a B3LYP optimized geometries and CAM-B3LYP functional.

Compound	#	λ_{cal} (nm)	λ_{exp}	f_{cal}	Wavefunction
AxBDY	S_1	411	507	0.54	H → L (24%), H → L+1 (24%), H-1→ L (24%), H-1→ L+1 (25%); …
	S_2	319		0.51	H → L (21%), H → L+1 (27%), H-1→ L (27%), H-1→ L+1 (21%); …
IBDY3	S_1	431	541	0.39	H → L (10%), H → L+1 (19%), H-1→ L (45%), H-1→ L+1 (22%); …
	S_2	331		0.52	H → L (22%), H → L+1 (45%), H-1→ L (20%), H-1→ L+1 (10%); …

* Oscillator strength (f_{cal}) with the TD-DFT predicted wavelengths (λ_{cal}) and the experimentally observed wavelengths (λ_{exp}). Percentage value for one electron transitions (1et) within each the excited states (#).

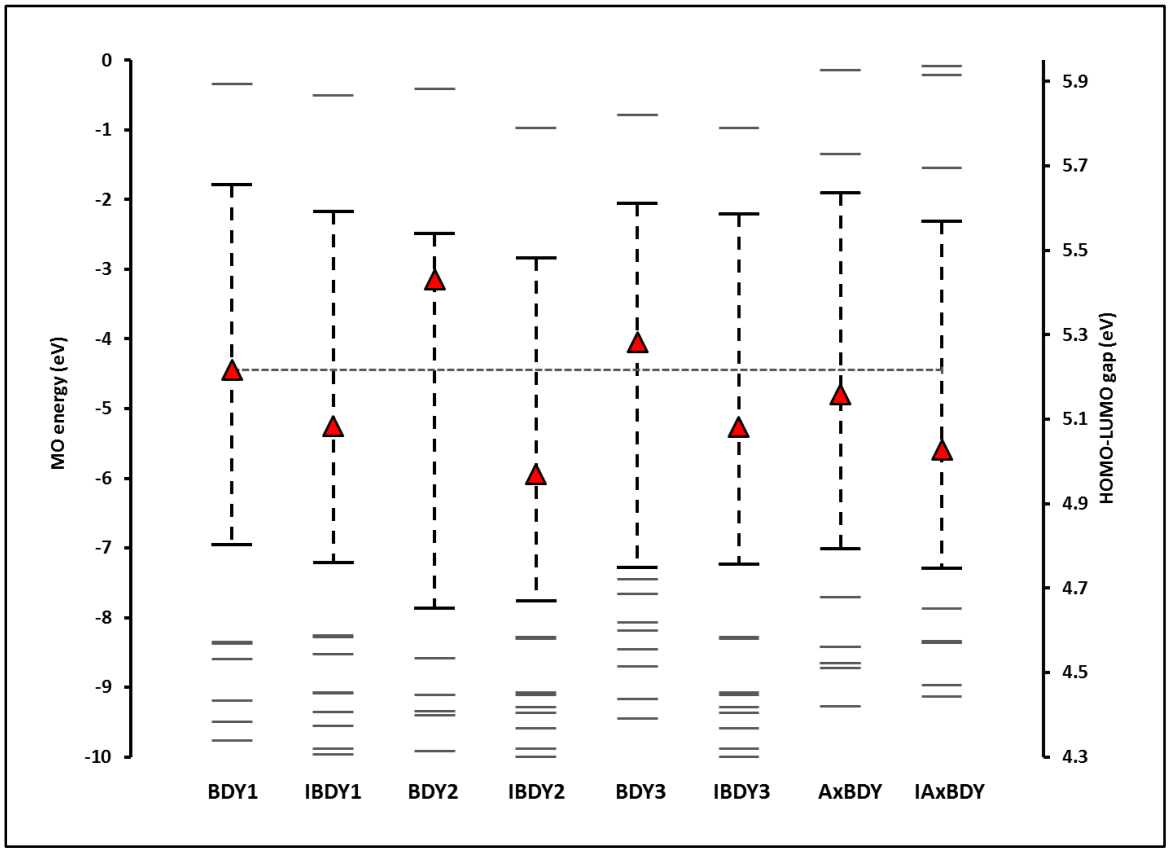

Figure 4.2.3: The predicted frontier π-MO energies for BDY1-3, IBDY1-3, AxBDY and IAxBDY. The HOMO and LUMO levels are indicated in bold (primary axis) and the HOMO–LUMO gap values are highlighted with red triangles (secondary axis).

Concluding remarks

The evaluation of a series of novel BODIPY target compounds was carried out by analyzing the results of DFT and TD-DFT calculations. While the compounds were not able to be synthesized, the calculations demonstrate their favourable attributes for the design of a molecular sensor. The TD-DFT calculations were also used to evaluate the electronic structures and optical properties of all of the compounds that were synthesized. Broadly similar trends were observed between the calculated and observed absorption maxima when a systematic over-estimation of the band energies is taken into account. Iodination is predicted to result in a narrowing of the HOMO–LUMO gap and hence a shift the band maximum of the main BODIPY spectral band significantly to the red in a manner that provides a good spectral overlap with the 540 nm emission band from the UCNPs. The theoretical calculations demonstrate that this is due to a relative destabilization of the HOMO, which has large MO coefficients at the 2, 6-positions, due to the mesomeric effect associated with the lone pairs of the iodine atoms. A similar pattern is observed for the calculations of the two novel BODIPY compounds, AxBDY and IAxBDY.

CHAPTER FIVE

Upconversion Nanoparticles

5. Upconversion Nanoparticles

The anti-Stokes process observed for UCNPs has gathered a lot of research momentum in the last couple of decades due to their possible use in biological applications[95]. This is directly related to their ability to absorb NIR radiation, within the therapeutic window, and produce a high energy output through the various energy transfer mechanisms detailed in Section 1.3. With conjugation to a PS where there is a significant overlap between the PS absorption and a UCNP emission band it is possible to generate $^1O_2$, since FRET can lead to the formation of the T_1 state of the PS. The main advantage lies in the low signal to noise ratio, in the context of biological autofluorescence, which is often a major drawback for photosensitizers absorbing in the high energy region of the spectrum.

This section examines the interaction between IBDY3 and three sets of UCNPs of different sizes. The nanoparticles were synthesized following a thermal decomposition method utilizing Yb^{3+} as the sensitizer and Er^{3+} as the activator in a fluoride host matrix. The three sets of oleate capped UCNPs, with diameters at ca. 210, 430 and 25 nm respectively, were silinized to obtain water dispersibility required for biological applications. Characterization was carried out using TEM, to determine particle size and dispersity, XRD to examine the phase purity and TCSPC to study the emission characteristics measured upon 978 nm excitation. An attempted functionalization with amine groups was then carried out, which provides the necessary framework for conjugation, but unfortunately this proved unsuccessful. Thereafter, a concentration study on the interaction between IBDY3 and UCNPs was carried out to establish the saturation point for maximum BODIPY absorption. Once this was obtained the silinized UCNP/IBDY3 mixture was irradiated with a hand held 978 nm laser to test for $^1O_2$ generation.

5.1. Synthesis of upconversion nanoparticles ($NaYF_4$: Yb/Er/Gd)

Uniform β-phase $NaYF_4$ nanocrystals were synthesized following a thermal decomposition method[123] with appropriate RE precursors, YNO_3 (5.2 x 10^{-4} mol), $ErCl_3$ (1.6 x 10^{-5} mol), $YbCl_3$ (1.4 × 10^{-4} mol) and $GdCl_3$ (1.2 × 10^{-4} mol). These were dissolved in methanol (4 ml) followed by the addition of the oleic acid (6 ml) capping agent and a high boiling point surfactant 1-octadecene (14 ml), which was required as high temperatures are involved during the reaction. After heating to 160 ^{o}C for 30 min the solution was allowed to cool at which point additional methanol (10 ml) was then added containing NH_4F (0.1161 g) and NaOH (0.080 g). Again, the solution was heated for 30 min at 70 ^{o}C, allowed to cool, and then heated to 300 ^{o}C and held for 1.5 h. The hydrophobic, oleate capped UCNPs (oleate@UCNP) were obtained in a dark brown/black colour and exhibit an excellent response to NIR stimulation by laser light, Section 5.2.3.

The oleate@UCNPs were rendered water dispersible by modifying the outer coating with a silica shell (Si@UCNPs). This was carried out by sonicating oleate@UCNPs (70 mg) in cyclohexane (5 ml) and the solution was made up to 60 ml. Igepal CO-520 (1 ml) was added as the emulsifier and the mixture was stirred until it was well dispersed. An additional Igepal CO-520 (4 ml) was added together with ammonia 25% (0.96 µl). Lastly, TEOS (400 µl) was added and the solution was left to stir under atmospheric conditions for 4 days and subsequently washed with ethanol. The Si@UCNPs appeared in modest yields as a fine, white/grey powder.

An organically modified salinizing agent, APTES, was used for the surface attachment of amine groups to provide the necessary scaffold for the formation of an amide link to IBDY3. The Si@UCNP particles (0.010 g) were washed with anhydrous ethanol and toluene, and were then

dissolved in DMF (12 ml) and toluene (8 ml) and allowed to stir until a complete dispersion was established. APTES (1 ml) was then added dropwise and the reaction was left to stir for 24 h at room temperature under an inert environment. A schematic outlining these procedures is provided in **Scheme 5.1.** This method was used for the synthesis of three sets of UCNPs, all adapted with silica coating, with variable sizes controlled during the final annealing step.

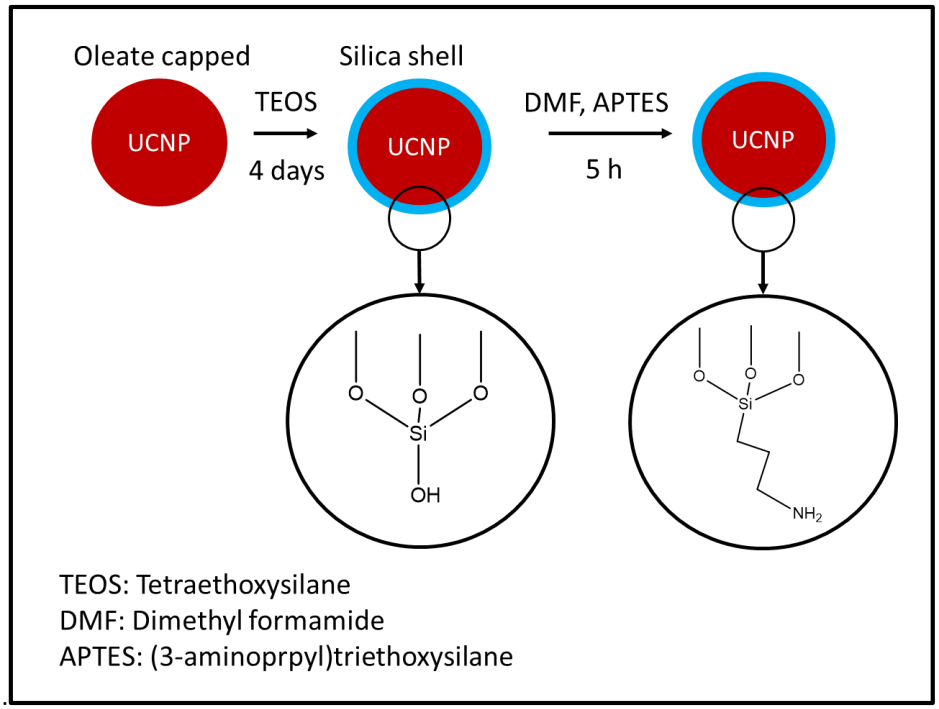

Scheme 5.1: Synthetic pathway for silica modified and amine functionalized of UCNPs

Rare-earth chloride precursors were used instead of the conventional sodium trifluoroacetates, for incorporating the Ln^{3+} dopants into the host matrix. The use of chlorides has some significant advantages; reduced costs, lower toxicity levels and relative insensitivity to air. The last factor was

tested by carrying out the reaction under atmospheric conditions, with the exception of the final annealing step at 300 °C. There were no observable changes in the overall yields or in the consistency of the nanoparticles.

5.2. Characterization of upconversion nanoparticles

5.2.1. Transmission Electron Microscopy (TEM)

TEM provides the first level characterization of the nanoparticles, **Figure 5.2**. Consistently, uncapped UCNPs exhibited low levels of aggregation and were well dispersed with a good size distribution. Sample A, with an average diameter of 216 nm, is clearly comprised of hexagonally shaped nanoparticles. The growth of these larger nanoparticles is thought to result from Oswald ripening[159] at higher temperatures where the smaller particles are re-dissolved due to the high surface energy and larger particles can grow. Sample B displays an increased average diameter of 436 nm with a tendency towards hexagonal particles. Closer inspection of these UCNPs reveals their formation through the aggregation of ± 46 nm sized particles. These results were confirmed by X-ray diffraction (XRD) measurements. where the average crystalline size calculated with the Debye-Scherrer equation[160] (**Equation 5.1**) focusing at the 53.7° (the (211) Miller index plane) is consistent with an average diameter of 48.5 nm. This type of aggregation is expected where the reaction time has been extended during the annealing phase of the synthesis, in this case to only 2 h. Similar results were observed by Mai and coworkers[161]. Sample C displays a narrow size distribution with relatively small spherical shapes (average diameter of ca. 24 nm) due to a restriction of the Oswald ripening process with the temperatures being held at 280 °C for the duration of the annealing phase.

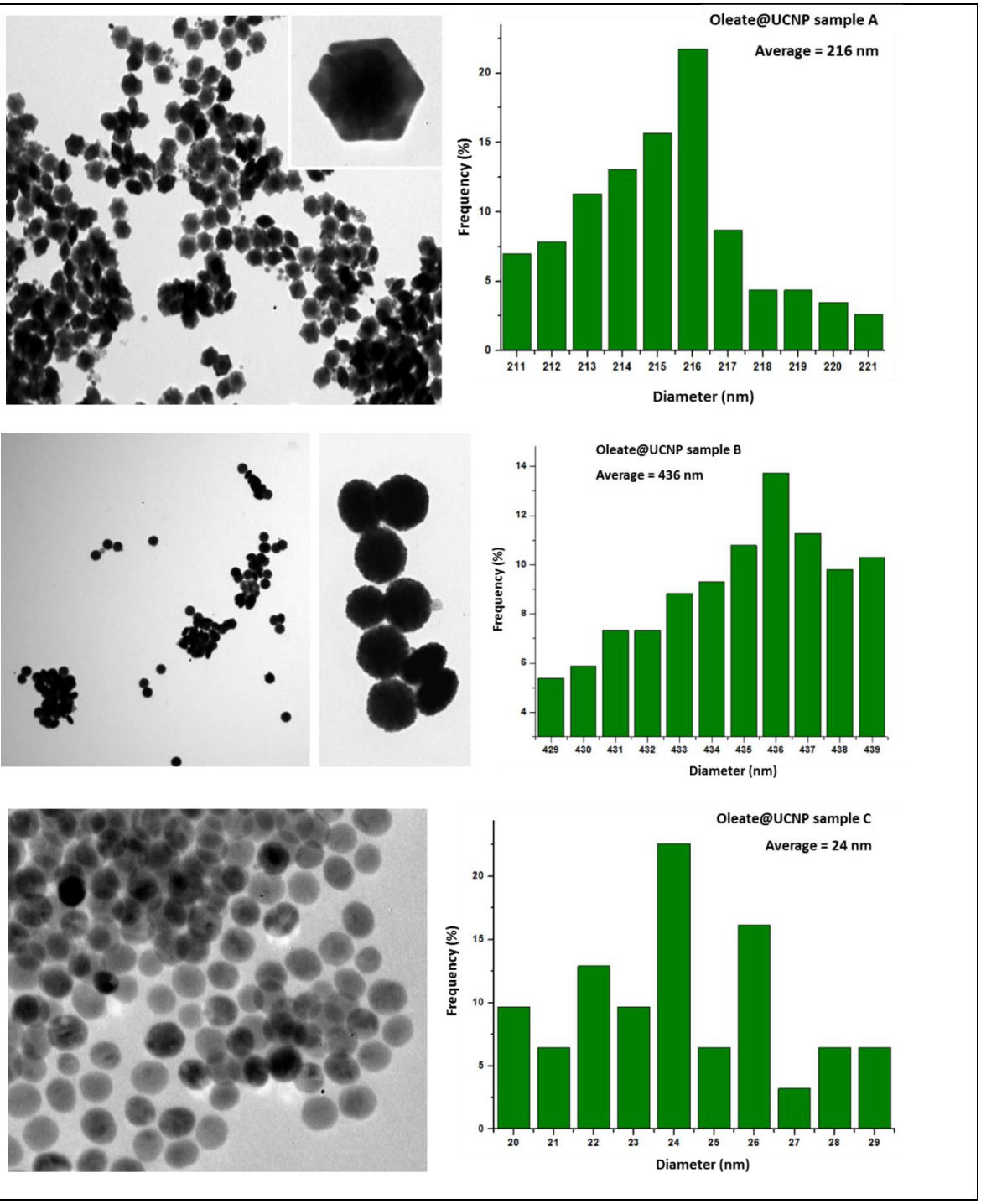
Oleate@UCNP sample A
Average = 216 nm
Frequency (%)
Diameter (nm)
Oleate@UCNP sample B
Average = 436 nm
Frequency (%)
Diameter (nm)
Oleate@UCNP sample C
Average = 24 nm
Frequency (%)
Diameter (nm)

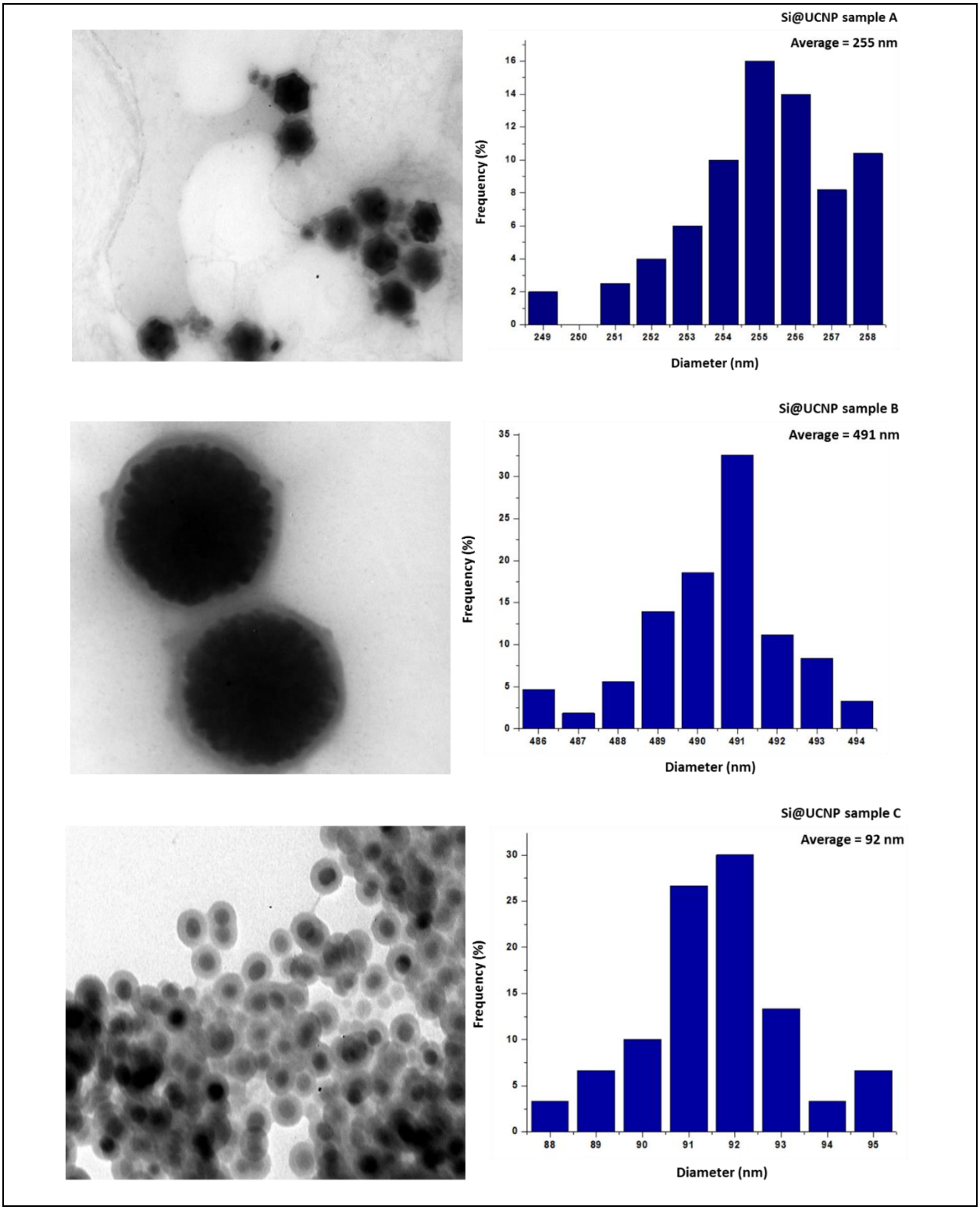

Figure 5.2: TEM images depicting oleate@UCNP samples A-C and their subsequent silica coating each with the corresponding average diameter.

The oleate@UCNP samples A–C were then coated with a SiO_2 layer and showed a steady size increase of 39, 55 and 68 nm, respectively, for Si@UCNP sample A, B and C, calculated using the ImageJ software. The extent of the silica coating is largely dependent on the reaction time. Stirring for four days produced a uniform coating as shown in Si@UCNP sample A, while the capping process for samples B and C were run for an extra 24 h. The expected thicker silica layer can be observed in the TEM images, **Figure 5.2**. Small amounts of aggregation are observed in the silinized particles but solitary particles were also isolated. This aggregation is related to slow evaporation of the solvent during sample preparation.

5.2.2. Powder X-ray Diffraction (XRD)

The size and phase were confirmed with the XRD patterns indexed to the β-$NaYF_4$ nanocrystals below with 2θ values at 17.1, 29.9, 30.8, 34.7, 39.8, 43.5, 46.5, 53.7 and 61.3° corresponding to the (100), (110), (101), (200), (111), (201), (210), (211) and (112) hkl miller indices, respectively (JCPDS standard card no 28-1192)[162]. Detailed analysis revealed that there were no impurities with reference peaks that are consistent with the pure β-phase. The average crystallite sizes of all samples were calculated with the Debye-Scherrer equation[160] (**Equation 5.1**) by focusing on the peak at 53.7°, and were found to confirm those derived using TEM, the aggregation of sample B being the only exception, shown in **Figure 5.2**.

$$d(\text{Å}) = \frac{k\lambda}{\beta \text{Cos}\theta} \qquad (5.1)$$

In **Equation 5.1**, *k* is a proportionality constant with a value of 0.9, which depends on the size and shape distribution, λ is the wavelength of the X-ray source (1.5405 Å for a Cu source), β is the full width at half maximum of the selected diffraction peak in radians and θ is the angular position, normally referred to as the Bragg angle[116].

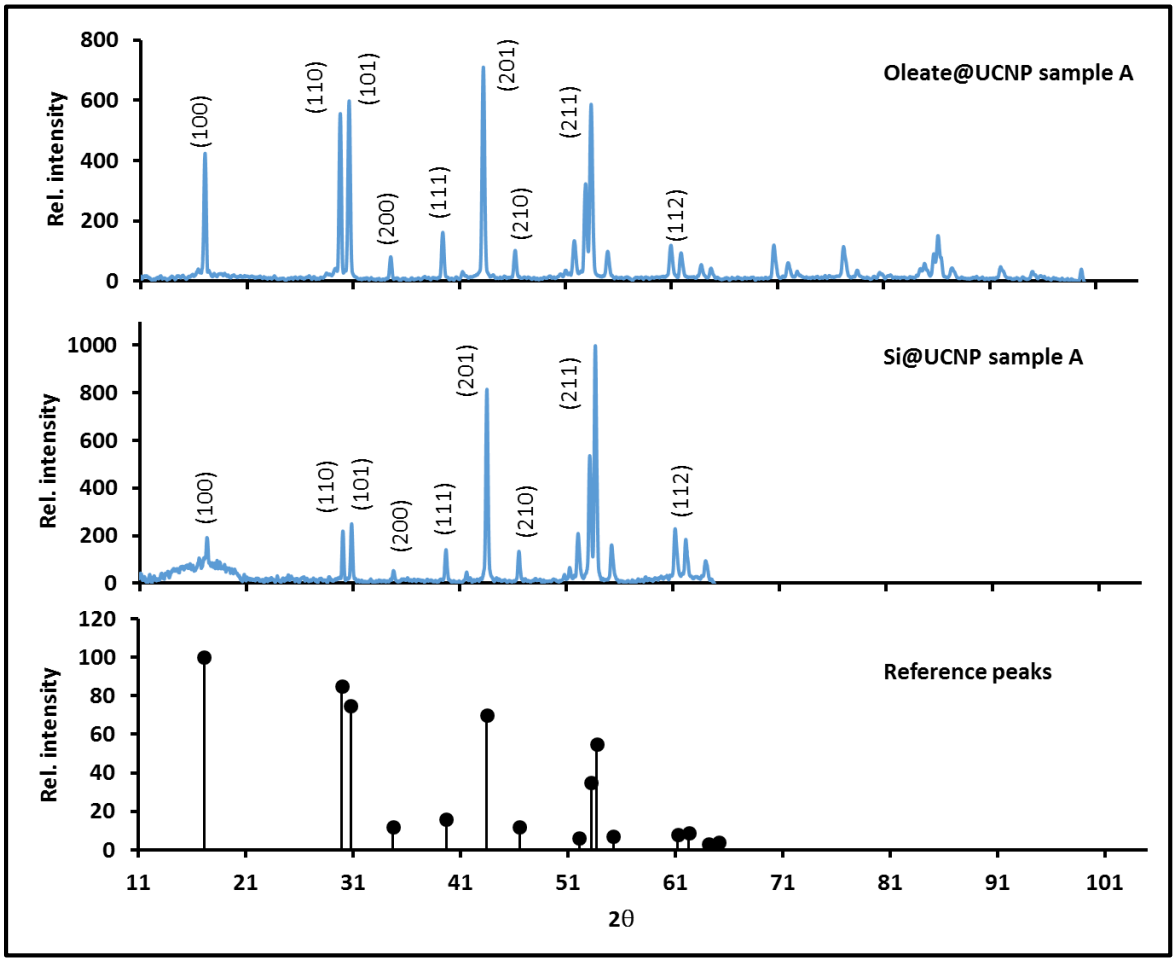

Figure 5.3.1: Powder X-ray diffraction pattern for sample A showing the effect of oleate and silica capping.

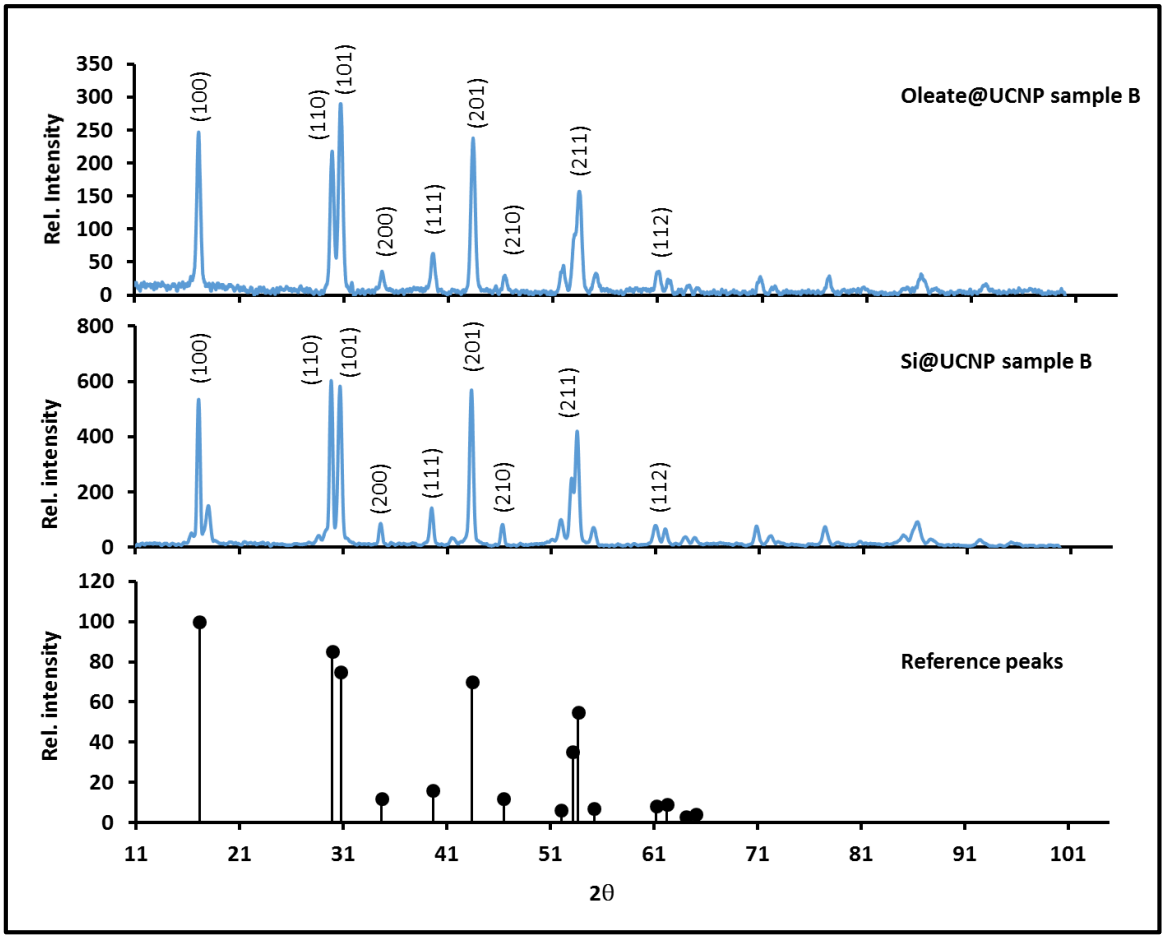

Figure 5.3.2: Powder X-ray diffraction pattern for sample B showing the effect of oleate and silica capping.

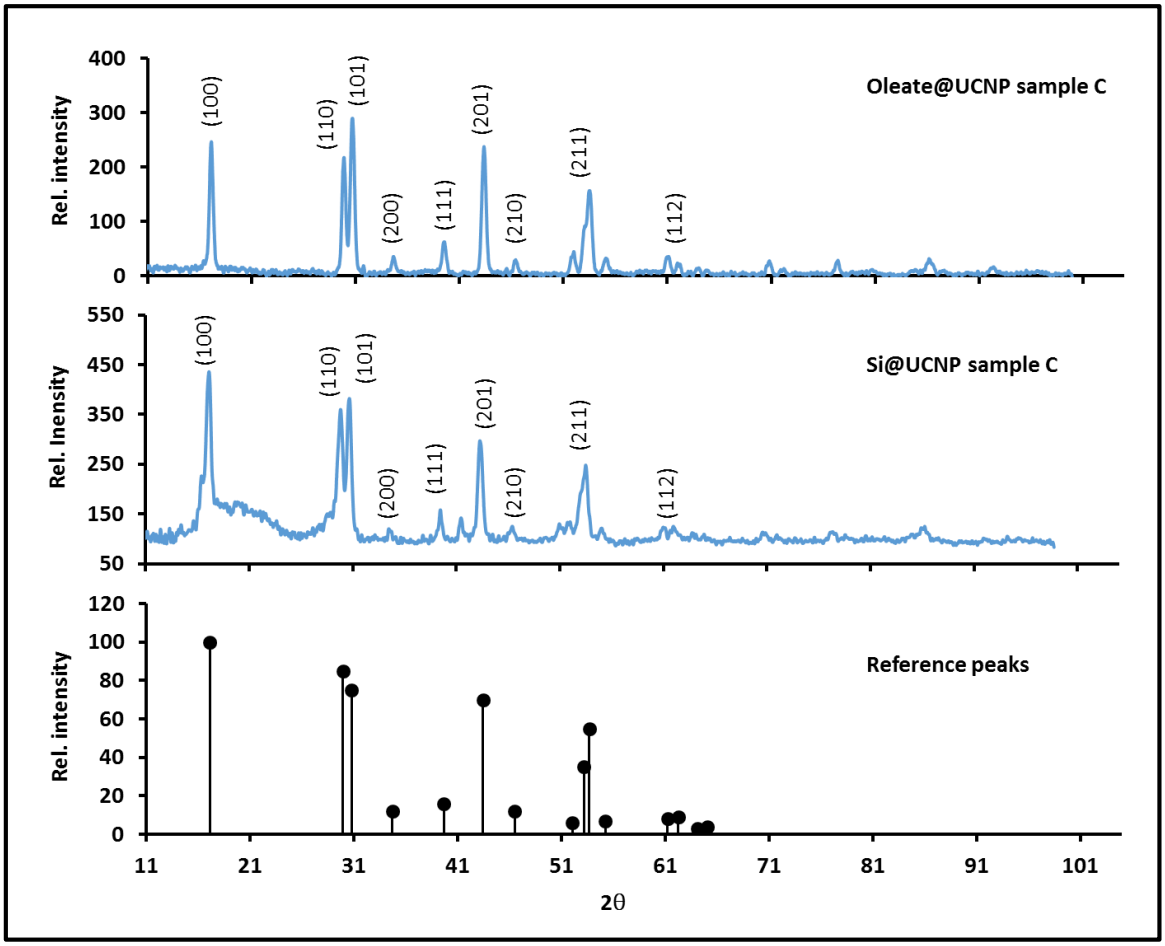

Figure 5.3.2: Powder X-ray diffraction pattern for sample C showing the effect of oleate and silica capping.

The silica coated samples, Figure 5.3.1-5.3.3, show a clear peak broadening at ca. 20° which can be unambiguously assigned to the amorphous nature of the shell. The nanoparticles maintain their crystallinity throughout showing that the SiO_2 layer does not alter the phase of the $NaYF_4$:Yb/Er UCNPs.

5.2.3. Steady state and time resolved fluorescence spectroscopy

The steady state fluorescence spectra for the UCNPs were obtained by excitation with a 972 nm continuous wave laser. Various emission bands can be observed from the activated levels of Er^{3+} at ca. 840 (NIR), 658 (red), 540 (green) and 410 nm (blue). The transitions giving rise to these bands are shown on spectra, **Figure 5.3.3 – 5.3.5.** The dominant emission bands at ca. 540 nm and 658 nm are associated with the $^2H_{11/2}$ and $^4F_{9/2}$ states, respectively, and result from two photon absorption. The intensity of the peaks reflect firstly the efficiency of the system as an upconverter, and secondly the relative extent to which weaker nonradiative relaxations occur.

The weaker 840 and 410 nm emission bands arise from the lowest and highest states, respectively, of the Er^{3+} ion by comparison with the 540 and 658 nm bands. Access to the higher energy states requires multiple steps of resonant absorption to reach and this is of significantly lower likelihood in probability terms. The weak peak in the 840 nm region can be assigned to either direct absorption to the activator or a single resonant transfer from the sensitizer, due to the near resonance between the Er^{3+} state ($^4I_{11/2}$) and a Yb^{3+} state ($^2F_{5/2}$) which have a ca. 4 cm^{-1} mismatch[114]. We can also assume that since no emission bands are observed from the activator $^4I_{11/2}$ or $^4I_{13/2}$ states cross relaxation from the Yb^{3+} ion or radiative relaxation from the $^4I_{11/2}$ state does not occur.

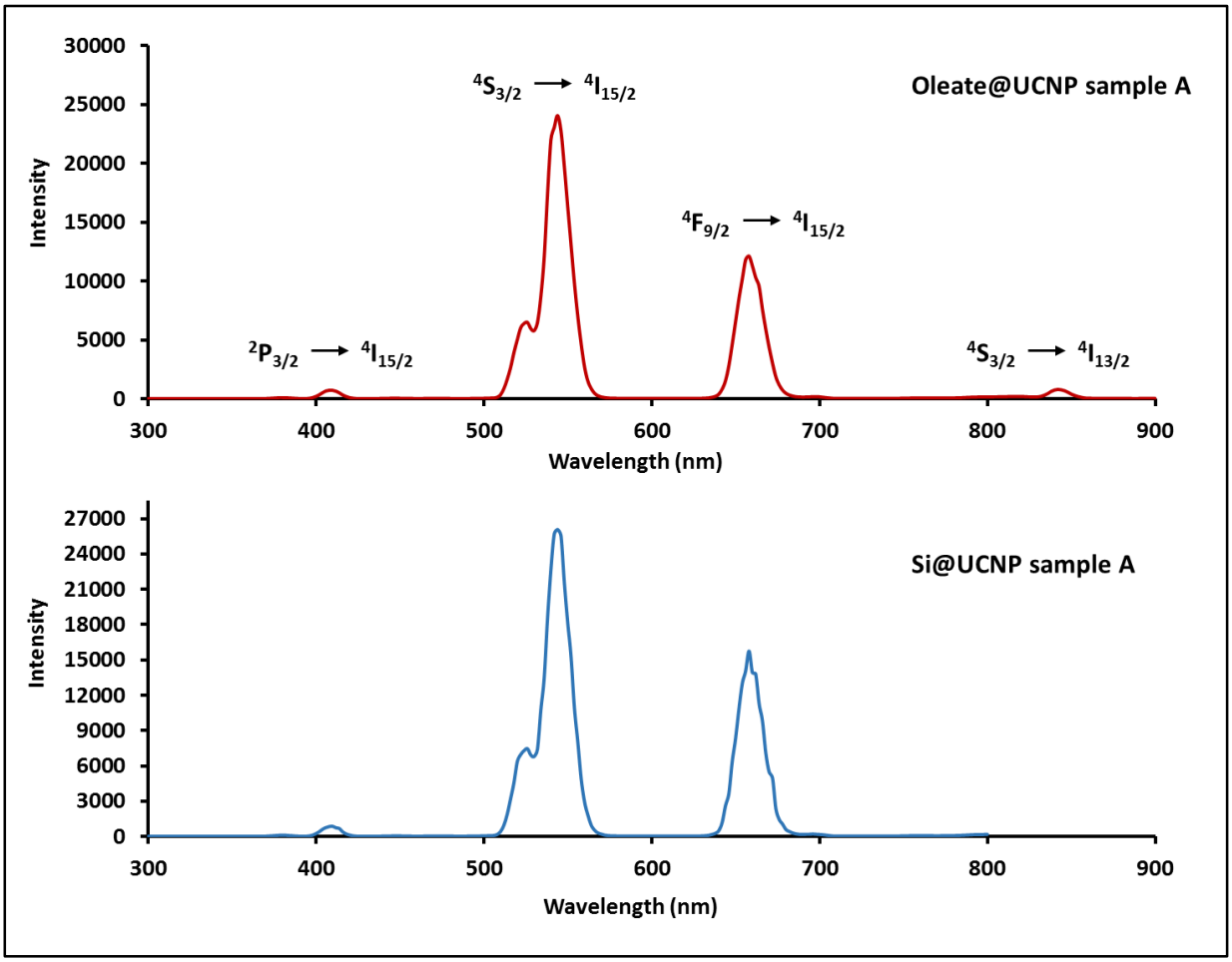

Figure 5.3.3: Emission profile of UCNPs sample A with an oleate cap (cyclohexane, top) and the silica coating (EtOH, bottom) after excitation at 972 nm.

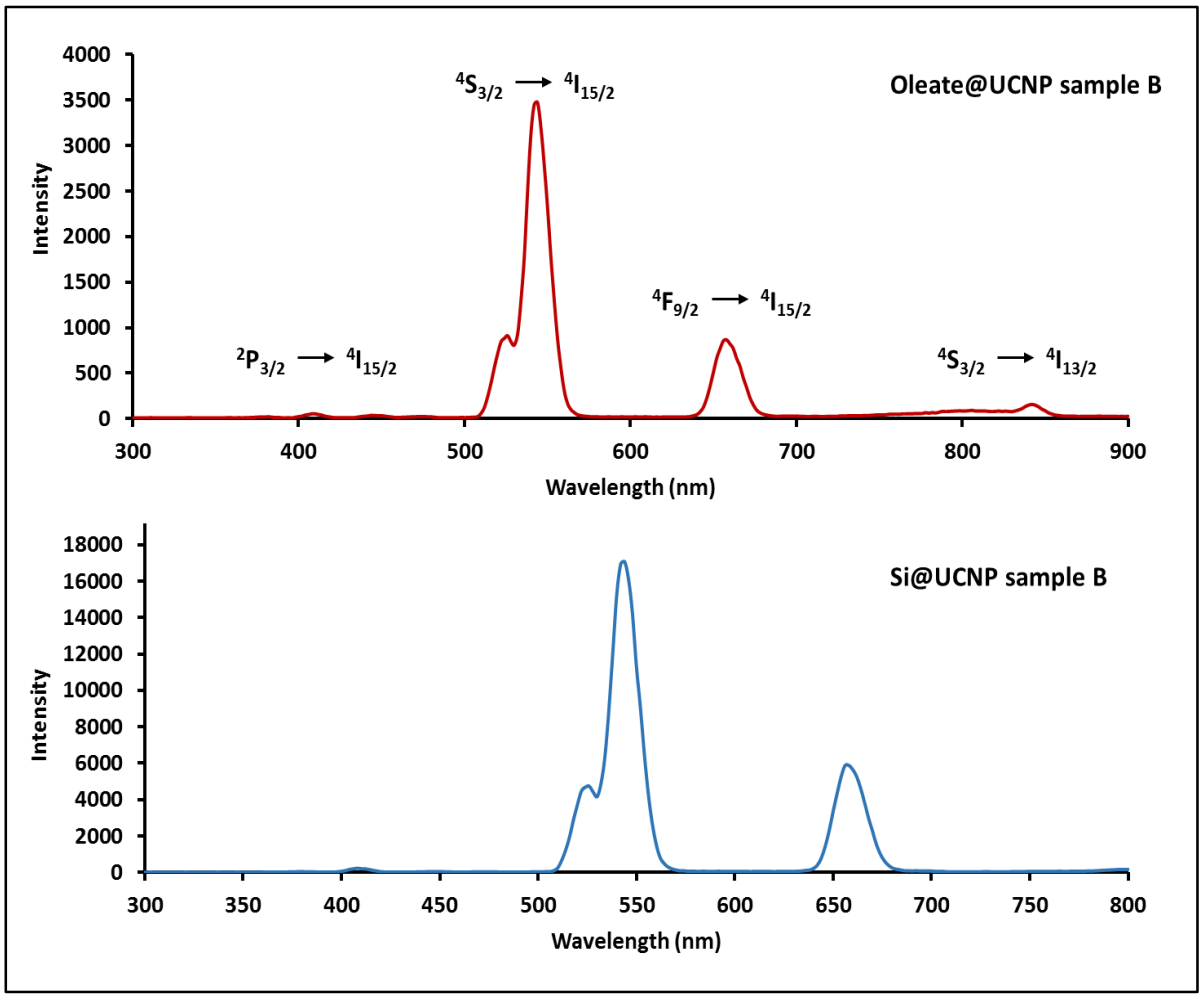

Figure 5.3.4: Emission profile of UCNPs sample B with an oleate cap (cyclohexane, top) and the silica coating (EtOH, bottom) after excitation at 972 nm.

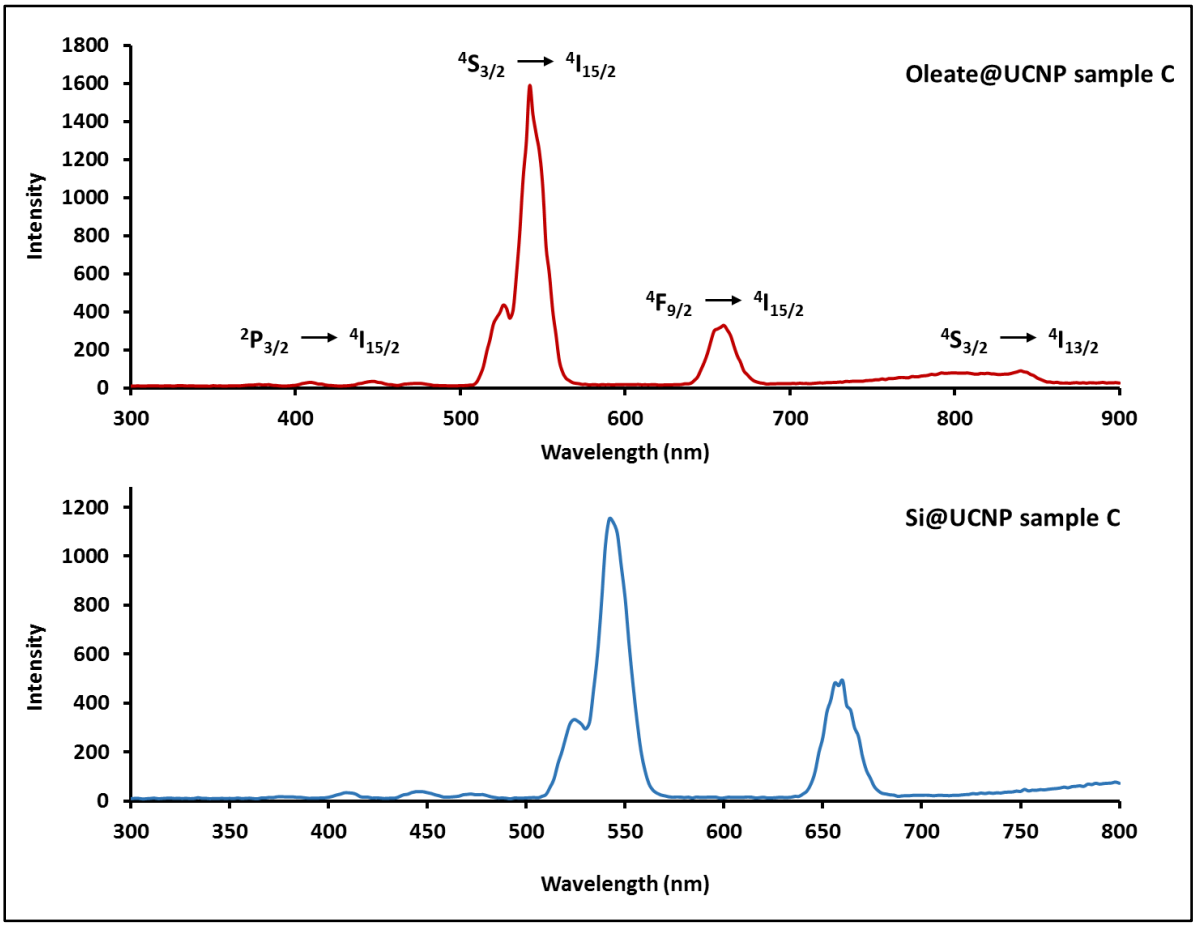

Figure 5.3.5: Emission profile of UCNPs sample C with an oleate cap (cyclohexane, top) and the silica coating (EtOH, bottom) after excitation at 972 nm.

It should be noted that in the context of stimulated emission, the power of laser excitation plays a significant role here. A study conducted by Suyver and coworkers[99] have shown that the relative emission band intensities become constant once a saturation power level is reached, found to be ca. 40 W/cm^2 for UCNPs with 2% Er^{3+}, 18% Yb^{3+} concentrations.

The excitation of nanoparticles with a SiO_2 shell was carried out in a solution of an. EtOH. Similar emission spectra were measured in all cases with minimal deviation from those of the uncapped

UCNPs. As reported in the literature[128], the hydrophobic layer has no effect on the UCNP emission spectrum.

Steady state fluorescent measurements were used to obtain lifetime values, which were found to lie in the μs timeframe. The data obtained for the oleate@UCNPs for samples A, B and C yielded values of 0.26 μs (R^2 = 1.067) 0.26 μs (R^2 = 1.012) and 0.20 μs (R^2 = 1.008), respectively, closely matching the values for Si@UCNPs samples A, B and C of 0.27 μs (R^2 = 1.017) 0.19 μs (R^2 = 1.008) and 0.17 μs (R^2 = 1.003). These values directly reflect the efficiency of the system as an upconverter, since long lifetimes are required to enable the sequential absorption of photons.

5.3. Studies on NIR stimulated singlet oxygen generation: Upconversion and BODIPYs

The method described for amine functionalization was carried out on Si@UCNPs sample C, since it has the smallest particle size. The Si@UCNPs were then analyzed by FTIR as the first level of characterization. The FTIR spectrum of the uncoated nanoparticles showed minor peaks at 1705 cm^{-1} and 2924 cm^{-1} representing the C=O and C–H stretches respectively. A broad, prominent band appeared at 1048 cm^{-1} after silinization indicating the presence of the Si–O bending vibration and, after amine functionalization, an almost identical spectrum was observed. According to the literature[163], the presence of amine groups should produce a minor, broad band due to the C–NH_2 bending vibration at 1653 cm^{-1}, which was not observed in the spectrum. Nevertheless, the procedure for conjugation, adapted from an organic synthetic method[164], was carried out. The resulting emission spectrum is shown in **Figure 5.3.6**.

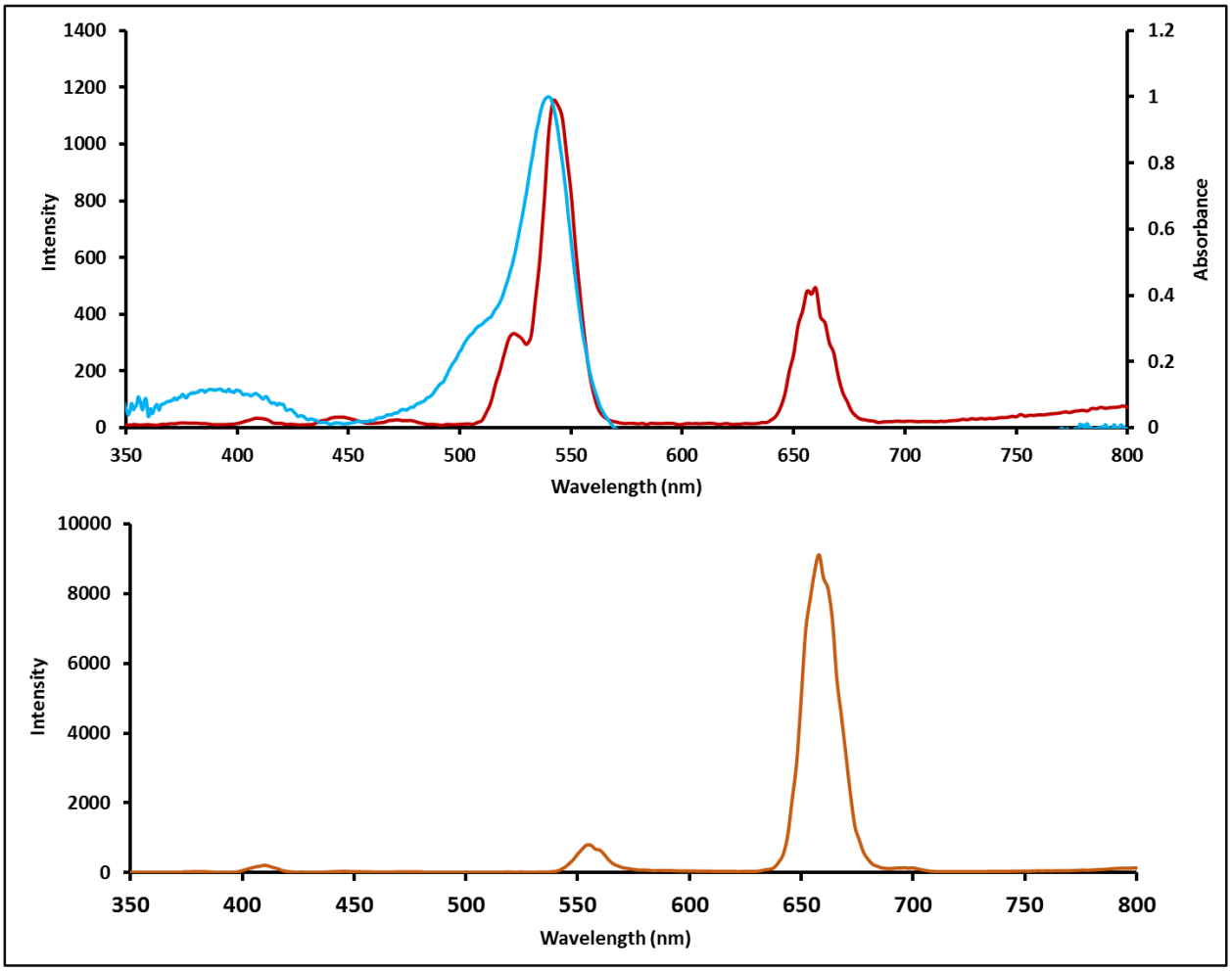

Figure 5.3.6: [top] An overlay spectrum between Si@UCNPs emission spectrum (red, EtOH) against the absorption of IBDY3 (blue, EtOH), secondary axis. [bottom] Spectrum showing the prewashed solution for attempted conjugation between Si@UCNPs with IBDY3, Scheme 5.1.

While the functionalization procedure proved unsuccessful it unambiguously showed that the Si@UCNP sample C green emission band could be significantly quenched in the presence of IBDY3, **Figure 5.3.6 bottom**, due to overlap in the IBDY3 absorption band and the Si@UCNP emission band at ca. 540 nm, **Figure 5.3.6 top**. The prewashed solution of IBDY3 and Si@UCNP sample C displays a weak emission intensity at ca. 555 nm relating to the saturation point for BODIPY absorption.

Following extraction of the nanoparticles by centrifugation in DCM and EtOH 1:1 there was a complete reappearance of the green emission band indicating that the conjugation was unsuccessful.

A study was then carried out to determine the saturation point for IBDY3 absorption. The stepwise increase in IBDY3 concentration, 1.18 x 10^{-3} M, was carried out until the UCNP green emission peak stabilized indicating the point of maximum BODIPY absorption, **Figure 5.3.7**. The inconsistency of the bands measured at the lower concentrations is a result of the long lifetimes of UCNPs after repetitive laser excitation. A study by Watkins et al.[165] on similar Si@UCNP samples in the presence of aluminium phthalocyanines demonstrated how the fluorescence emission could be stabilized when the nanoparticles were embedded in electrospun fibers. This effect was attributed to high phonon energies causing a loss via nonradiative decay which lowered the fluorescence lifetimes. In the context of repetitive laser excitation, this caused a stabilization of the emission bands.

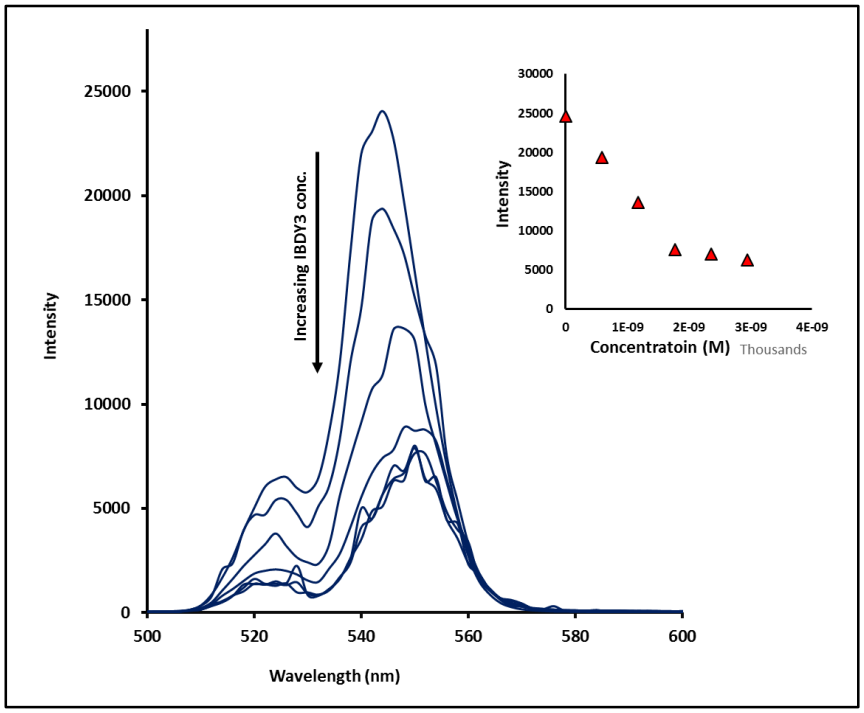

Figure 5.3.7: The observed decrease in the Si@UCNP sample Cs peak with increasing IBDY3 concentration (EtOH). The inset shows intensity as a function of concentration.

Previous research[166] has indicated that for the emission band of UCNPs to be sufficiently quenched there does not need to be a formal bond between the UCNPs and the PS dye. The energy transfer here is based on the proximity of the donor and acceptor which, once at saturation point, is indicative of the complete encapsulation of the UCNPs by IBDY3. Once the saturation point was obtained, the samples were irradiated with a 1000 mW 978 nm hand held laser. Unfortunately, no standard could be obtained since the study is based on a transfer process and not on direct stimulation. The $^1O_2$ quencher DPBF was used as before with irradiation time varying from 0.5 to 60 s then increased to 5, 10 and 20 min and was finally irradiated for a 30 min period. At each

interval the samples were analyzed with UV-visible spectrometry. No decrease in the DPBF absorbance was observed at any of the time intervals.

The utilization of a BODIPY, with a carboxylic acid at the meso-position, as a PS had previously been reported by Gonzales-Bejar et al.[143] where the BODIPY was embedded in polyethylene glycol (PEG) and used to cap the UCNPs, as well as being grafted to the PEG-UCNP surface afterwards. In this way they managed to concentrate the photosensitizer molecules to such a degree that $^1O_2$ could be generated from the energy transfer between the two. The results demonstrated a 50% cancer cell death after low energy stimulation.

In the context of this study, although energy from the UCNP emission band is absorbed by the IBDY3 π-system to an extent sufficient to quench its intensity, attempts to monitor the rates of $^1O_2$ generation that resulted from this proved unsuccessful. It is possible that the main issue in this regard is related to using the comparative method. The absorbance value at the λ_{max} value of the DPBF $^1O_2$ scavenger was greater than 1.5, outside the linear response range of most spectrophotometers. There also appeared to be issues relating to the solubility of UCNPs in the EtOH solution at the concentrations used for the measurements, where prolonged irradiation through repetitive laser excitation may have enhanced their solubility and this may have had an effect on the observed absorbance value. Therefore, a better approach for the quantitative measurement of a ϕ_Δ quantum yield value needs to be identified if this research is to be expanded upon in the future. It is possible that a comparison of the time decay profile for $^1O_2$ phosphorescence decay at 1270 nm after laser excitation in the NIR region with that of a known standard would provide a better approach. A significant issue faced in carrying out measurements at this wavelength is that most of the known literature standards for ϕ_Δ measurements have

absorption bands that lie in the visible region. This is problematic when laser excitation at ca. 980 nm is involved, but recent advances in the synthesis of porphyrin and phthalocyanine dyes, with appreciable ϕ_{Δ} quantum yield values and absorption bands in the NIR region, may provide a viable standard for comparison.

CHAPTER SIX

Conclusions

6. Conclusion

A novel BODIPY dimer (AxBDY), ethynyl (BDY1) and ester (BDY3) functionalized BODIPY dyes were successfully synthesized and characterized using a wide range of techniques. The compounds were then successfully modified for $^1O_2$ production by attachment of iodine atoms at selected positions on the core. This was carried out to induce the transfer of energy from the singlet to triplet state via the heavy atom effect required for $^1O_2$ generation. The measured compounds showed very high ϕ_Δ quantum yield values of 0.86 and 0.87 for IBDY1 and IBDY3, respectively. In the context of the novel AxBDY, an increase in the ϕ_Δ quantum yield value was expected after the attachment of iodine atoms due to the presence of two additional iodination site on the BODIPY chromophore. However, a small increase from 0.86 to 0.88 was observed by comparison to the IBDY1 monomer which can be attributed to the low ε value. As most BODIPY dyes with a 1, 3, 5, 7-tetramethyl conformation, which sterically hinders the phenyl group rotation, a BODIPY with an unsubstituted core was synthesized, BDY2, with the same ethynyl functionality at the meso-position as BDY1. Its characterization revealed a significantly lower ε value with reference to its BDY1 counterpart as well as the absence of fluorescence emission. The properties of the synthetic dyes were elucidated and confirmed by studying the MOs generated by TD-DFT calculations.

A second study was carried out with IBDY3 in conjunction with UCNPs since these display a good overlapping wavelength at ca. 540 nm. The selected BODIPY was chosen for its methyl ester group which provides the functionality for linkage to amine functionalized UCNPs and, after iodination, a high ϕ_Δ quantum yield value. Here, three sets of UCNPs of different sizes, ca. 210, 430 and 25 nm respectively, were synthesized using the dopant ions Yb^{3+} and Er^{3+} together with Gd^{3+}, the ion assisting in phase change, incorporated into a $NaYF_4$ host matrix. The samples were characterized

using TEM, XRD and TCSPC. The later were used to measure the upconversion emission spectrum after 978 nm excitation and showed the characteristic peaks in the blue, green and red regions of the spectrum with varying intensity depending on their upconversion probability. The same characterization techniques were used after silinization in order to render the UCNPs water dispersible and applicable for use in biological studies. The silica coated nanoparticles underwent an amine functionalization procedure for the attachment to IBDY3, which proved unsuccessful.

It was found, however, that the absorption cross section between the IBDY3 and Si@UCNPs was sufficient to completely quench the main ca. 540 nm emission band of the nanoparticles. A study was then conducted to find the maximum amount of energy that could be transferred from UCNP to BODIPY, the saturation point. As conjugation could not be achieved the measurements were based on the proximity of IBDY3 to the UCNPs in solution. Once found, the sample was then tested for $^1O_2$ generation with DPBF as the singlet oxygen scavenger but without the use of a standard due to the singlet oxygen being generated from an energy transfer process rather than direct PS stimulation. Irradiation with a 978 nm hand held laser proved this study unsuccessful but nevertheless revealed insights into the energy transfer process between UCNPs and BODIPY dyes. The high ϕ_Δ values of the 2, 6-iodinated BODIPY dyes as well as their chemical durability make them excellent candidates for future applications in biological fields. The main drawback in this regard and in other contexts is their absorption at ca. 500 nm, well outside the therapeutic window, and their lack of solubility in aqueous solvents. This research provides the foundation for further studies into the versatility of the BODIPY dyes and their relationship to UCNPs. The amine functionalization of UCNPs and their conjugation to IBDY3, or IAxBDY, should be focused on in future studies, since this would address both issues. A different method for the measuring the ϕ_Δ

quantum yield values should also be employed in future. The synthesis of BODIPYs was one of the main limitations faced, due to the conditions required to produce near quantitative yields. Future work could focus on perfecting the water precipitation method, Section 3.1.2, which was less problematic at the critical starting phase of the synthetic procedure. A study on the solid state fluorescence properties of BDY2 should also be carried out for possible dye sensitized solar cell applications.

References

(1) Kruk, I. *Environmental Toxicology and Chemistry of Oxygen Species*, 2.1 ed.; Springer: Berlin, 1998.

(2) DeRosa, M. C.; Crutchley, R. J. *Coord. Chem. Rev.* 2002, *233-234*, 351–371.

(3) Lee, S.; Vu, D. H.; Hinds, M. F.; Davis, S. J.; Hasan, T.; Khachemoune, A.; Rice, W. *SPIE Pap.* 2006, *6139*, 26–31.

(4) Egorov, S. Y.; Kamalov, V. F.; Koroteev, N. I.; Krasnovsky, A. A.; Toleutaev, B. N.; Zinukov, S. V. *Chem. Phys. Lett.* 1989, *163* (4-5), 421–424.

(5) Gould, I. R.; Noukakis, D.; Gomez-Jahn, L.; Young, R. H.; Goodman, J. L.; Farid, S. *Chem. Phys.* 1993, *176*, 439–456.

(6) Berezin, M. Y.; Achilefu, S. *Chem. Rev.* 2010, *110* (5), 2641–2684.

(7) Lakowicz, J. R. *Principles of fluorescence Spectroscopy*, 2nd ed.; Springer: Maryland, 2006.

(8) Valeur, B.; Berberan-Santos, M. N. *Molecular Fluorescence*, 2nd ed.; Wiley-VCH: Germany, 2012.

(9) Zabuga, A. V.; Kamrath, M. Z.; Rizzo, T. R. *J. Phys. Chem. A* 2015, *119* (42), 10494–10501.

(10) Kasha, M.; Rawls, H. R.; Ashraf El-Bayoumi, M. *Pure Appl. Chem.* 1965, *11* (3-4), 371–392.

(11) Gilbert, A.; Baggott, J. *Essentials of Molecular Photochemistry*; Blackwell Sciences Ltd, 1991.

(12) Forster, L. S. *Coord. Chem. Rev.* 2006, *250* (15-16), 2023–2033.

(13) Kasha, M. In *Discuss. Faraday Soc.*; 1950; Vol. 9, pp 14–19.

(14) Karatay, A.; Miser, M. C.; Cui, X.; Küçüköz, B.; Yılmaz, H.; Sevinç, G.; Akhüseyin, E.; Wu, X.; Hayvali, M.; Yaglioglu, H. G.; Zhao, J.; Elmali, A. *Dyes Pigments* 2015, *122*, 286–294.

(15) Ludin, N. A.; Al-Alwani Mahmoud, A. M.; Bakar Mohamad, A.; Kadhum, A. A. H.; Sopian, K.; Abdul Karim, N. S. *Renew. Sustain. Energy Rev.* 2014, *31*, 386–396.

(16) Yersin, H.; Rausch, A. F.; Czerwieniec, R.; Hofbeck, T.; Fischer, T. *Coord. Chem. Rev.* 2011, *255* (21-22), 2622–2652.

(17) Blume, M.; Watson, R. E. *Proc. R. Soc. Lond. A* 1962, *270* (1340), 165–183.

(18) Szabo, A.; Ostlund, N. S. *Modern Quantum Chemistry: Introduction to Advanced Electronic Structure Theory*, 1st ed.; Dover Publications, INC.: New York, 2012.

(19) Redmond, R. W.; Kochevar, I. E.; Krieg, M., Smith, G.; McGimpsey, W. *J. Phys. Chem. A* 1997, *101* (15), 2773–2777.

(20) McGown, L. B.; Nithipatikom, K. *Appl. Spectrosc. Rev.* 2000, *35* (4), 353–393.

(21) Huber, K. P.; Herzberg, G. *Molecular Spectra an Molecular Structure. I. Specrtra of Diatomic Molecules*, 2nd ed.; Van Nostrand: New York, 1950.

(22) Neugebauer, J.; Jan Baerends, E.; Nooijen, M. *J. Phys. Chem. A* 2005, *109* (6), 1168–1179.

(23) Pollack, S. A. *J. Chem. Phys.* 1963, *38* (1), 98–108.

(24) Kitai, A. *Luminescent Materials and Applications*; John Wiley and Sons, Ltd: England, 2008.

(25) Lin, M.; Zhao, Y.; Wang, S.; Liu, M.; Duan, Z.; Chen, Y.; Li, F.; Xu, F.; Lu, T. *Biotechnol. Adv.* 2012, *30* (6), 1551–1561.

(26) Valeur, B. *Coord. Chem. Rev.* 2000, *205* (1), 3–40.

(27) Brouwer, A. M. *Pure Appl. Chem.* 2011, *83* (12), 2213–2228.

(28) Laverdant, J.; Marcillac, W. D. De; Barthou, C.; Chinh, V. D.; Schwob, C.; Coolen, L.; Benalloul, P.; Nga, P. T. *Materials* 2011, *4*, 1182–1193.

(29) Fischer, M. *Chem. Phys. Lett.* 1996, *2614* (260), 115–118.

(30) Hackbarth, S.; Ro, B.; Spiller, W.; Kliesch, H.; Wo, D. *J. Porphyrins Phthalocyanines* 1998, *2*, 145–158.

(31) Kuznetsova, N. A.; Gretsova, N. S.; Yuzhakova, O. A.; Negrimovskii, V. M.; Kaliya, O. L.; Luk'yanets, E. A. *Russ. J. Gen. Chem.* 2001, *71* (1), 36–41.

(32) Treibs, A.; Kreuzer, F. *Eur. J. Org. Chem.* 1968, *718* (1), 208–223.

(33) Schmitt, A.; Hinkeldey, B.; Wild, M.; Jung, G. *J. Fluoresc.* 2009, *19* (4), 755–758.

(34) Camerel, F.; Ulrich, G.; Barberá, J.; Ziessel, R. *Eur. J. Chem.* 2007, *13* (8), 2189–2200.

(35) Bergström, F.; Mikhalyov, I.; Hägglöf, P.; Wortmann, R.; Ny, T.; Johansson, L. B. Å. *J. Am. Chem. Soc.* 2002, *124* (2), 196–204.

(36) Ulrich, G.; Ziessel, R.; Harriman, A. *Angew. Chem. Int. Ed.* 2008, *47* (7), 1184–1201.

(37) Qin, W.; Baruah, M.; De Borggraeve, W. M.; Boens, N. *J. Photochem. Photobiol. A* 2006, *183* (1-2), 190–197.

(38) Rurack, K.; Spieles, M. *Anal. Chem.* 2011, *83* (4), 1232–1242.

(39) Ziessel, R.; Ulrich, G.; Harriman, A. *New J. Chem.* 2007, *31* (4), 496–501.

(40) Singh-rachford, T. N.; Haefele, A.; Ziessel, R.; Castellano, F. N. *J. Am. Chem. Soc.* 2008, *130* (48), 16164–16165.

(41) Singh, S. P.; Gayathri, T. *Eur. J. Org. Chem.* 2014, *2014* (22), 4689–4707.

(42) Zheng, Q.; Xu, G.; Prasad, P. N. *Eur. J. Chem.* 2008, *14* (19), 5812–5819.

(43) Tram, K.; Yan, H.; Jenkins, H. A.; Vassiliev, S.; Bruce, D. *Dyes Pigments* 2009, *82* (3), 392–395.

(44) Zhou, Y.; Xiao, Y.; Li, D.; Fu, M.; Qian, X. *J. Org. Chem.* 2008, *73* (4), 1571–1574.

(45) Miao, Q. *Polycyclic Arenes and Heteroarenes: Synthesis, Properties, and Applications*;

Wiley-VCH, 2015.

(46) Loudet, A.; Burgess, K. *Chem. Rev.* 2007, *107* (11), 4891–4932.

(47) Jiao, C.; Zhu, L.; Wu, J. *Eur. J. Chem.* 2011, *17* (24), 6610–6614.

(48) Devaraj, N. K.; Hilderbrand, S.; Upadhyay, R.; Mazitschek, R.; Weissleder, R. *Angew. Chem.* 2010, *122* (16), 2931–2934.

(49) Rihn, S.; Retailleau, P.; Bugsaliewicz, N.; Nicola, A. D.; Ziessel, R. *Tetrahedron Lett.* 2009, *50* (50), 7008–7013.

(50) Leen, V.; Qin, W.; Yang, W.; Cui, J.; Xu, C.; Tang, X.; Liu, W.; Robeyns, K.; Van Meervelt, L.; Beljonne, D.; Lazzaroni, R.; Tonnelé, C.; Boens, N.; Dehaen, W. *Chem. Asian J.* 2010, *5* (9), 2016–2026.

(51) Nuri Kursunlu, A.; Guler, E. *J. Luminesc.* 2014, *145*, 608–614.

(52) Nagai, A.; Miyake, J.; Kokado, K.; Nagata, Y.; Chujo, Y. *J. Am. Chem. Soc.* 2008, *130*, 15276–15278.

(53) Rohand, T. *Arkivoc* 2007, *2007* (10), 307–324.

(54) Zhang, M.; Hao, E.; Xu, Y.; Zhang, S.; Zhu, H.; Wang, Q.; Yu, C.; Jiao, L. *RSC Adv.* 2012, *2*, 11215–11218.

(55) Lee, C. Y.; Hupp, J. T. *Langmuir* 2010, *26* (5), 3760–3765.

(56) Jiao, L.; Yu, C.; Uppal, T.; Liu, M.; Li, Y.; Zhou, Y.; Hao, E.; Hu, X.; Vicente, M. G. H. *Org. Biomol. Chem.* 2010, *8* (11), 2517–2519.

(57) Vos de Wael, E.; Pardoen, J. A.; van Koeveringe, J. A.; Lugtenburg, J. *Eur J. Org. Chem.* 1977, *96* (12), 306–309.

(58) Ulrich, G.; Ziessel, R. *J. Org. Chem.* 2004, *69* (6), 2070–2083.

(59) Boens, N.; Leen, V.; Dehaen, W. *Chem. Soc. Rev.* 2012, *41* (3), 1130–1172.

(60) Jiao, L.; Yu, C.; Liu, M.; Wu, Y.; Cong, K.; Meng, T.; Wang, Y.; Hao, E. *J. Org. Chem.* 2010, *75* (17), 6035–6038.

(61) Karolin, J.; Johansson, L. B. A.; Strandberg, L.; Ny, T. *J. Am. Chem. Soc.* 1994, *116* (17), 7801–7806.

(62) Lu, J.; Qi, X.; Yue, T.; Tang, W.; Ding, L. *Tetrahedron* 2015, 71, 1304–1310.

(63) Baruah, M.; Qin, W.; Flors, C.; Hofkens, J.; Vallée, R. A. L.; Beljonne, D.; Van Der Auweraer, M.; De Borggraeve, W. M.; Boens, N. *J. Phys. Chem. A* 2006, *110* (18), 5998–6009.

(64) Duvva, N.; Sudhakar, K.; Badgurjar, D.; Chitta, R.; Giribabu, L. *J. Photochem. Photobiol. A* 2015, *312*, 8–19.

(65) Wang, R.; Geng, Y.; Zhang, L.; Wu, W.; Fan, W.; Li, Z.; Wang, L.; Zhan, L.; Wu, X.; Wu, M. *Chin. J. Chem.* 2015, *33* (11), 1251–1258.

(66) Sunahara, H.; Urano, Y.; Kojima, H.; Nagano, T. *J. Am. Chem. Soc.* 2007, *129* (17), 5597–5604.

(67) Wu, Y.; Peng, X.; Guo, B.; Fan, J.; Zhang, Z.; Wang, J.; Cui, A.; Gao, Y. *Org. Biomol. Chem.* 2005, *3*, 1387–1392.

(68) Bozdemir, O. A.; Guliyev, R.; Buyukcakir, O.; Selcuk, S.; Kolemen, S.; Gulseren, G.; Nalbantoglu, T.; Boyaci, H.; Akkaya, E. U. *J. Am. Chem. Soc.* 2010, *132* (23), 8029–8036.

(69) Zhu, S.; Zhang, J.; Vegesna, G.; Tiwari, A.; Luo, F.-T.; Zeller, M.; Luck, R.; Li, H.; Green, S.; Liu, H. *RSC Adv.* 2012, *2* (2), 404–407.

(70) Lu, H.; Zhang, S.; Liu, H.; Wang, Y.; Shen, Z.; Liu, C.; You, X. *J. Phys. Chem. A* 2009, *113* (51), 14081–14086.

(71) Buyukcakir, O.; Bozdemir, O. A.; Kolemen, S.; Erbas, S.; Akkaya, E. U. *Org. Lett.* 2009, *11*, 4644–4647.

(72) Kolemen, S.; Cakmak, Y.; Erten-Ela, S.; Altay, Y.; Brendel, J.; Thelakkat, M.; Akkaya, E. U. *Org. Lett.* 2010, *12* (17), 3812–3815.

(73) Liu, J.-Y.; Ermilov, E. A.; Röder, B.; Ng, D. K. P. *Chem. Commun.* 2009, 1517–1519.

(74) Shao, J.; Guo, H.; Ji, S.; Zhao, J. *Biosens. Bioelectron.* 2011, *26* (6), 3012–3017.

(75) Hecht, M.; Fischer, T.; Dietrich, P.; Kraus, W.; Descalzo, A. B.; Unger, W. E. S.; Rurack, K. *ChemistryOpen* 2013, *2* (1), 25–38.

(76) Li, L.; Nguyen, B.; Burgess, K. *Bioorg. Med. Chem. Lett.* 2008, *18* (10), 3112–3116.

(77) Atilgan, S.; Ozdemir, T.; Akkaya, E. U. *Org. Lett.* 2008, *10* (18), 4065–4067.

(78) Massue, J.; Frath, D.; Ulrich, G. *Org. Lett.* 2011, *13* (22), 6098–6101.

(79) Leen, V.; Gonzalvo, V. Z.; Deborggraeve, W. M.; Boens, N.; Dehaen, W. *Chem. Commun.* 2010, *46*, 4908–4910.

(80) Rohand, T.; Qin, W.; Boens, N.; Dehaen, W. *Eur. J. Org. Chem.* 2006, *20*, 4658–4663.

(81) Leen, V.; Braeken, E.; Luckermans, K.; Jackers, C.; Van der Auweraer, M.; Boens, N.; Dehaen, W. *Chem. Commun.* 2009, *30*, 4515–4517.

(82) Benniston, A. C.; Copley, G. *Phys. Chem. Chem. Phys.* 2009, *11*, 4124–4131.

(83) Jiao, L.; Yu, C.; Li, J.; Wang, Z.; Wu, M.; Hao, E. *J. Org. Chem.* 2009, *74* (19), 7525–7528.

(84) Stucky, G. D.; Dougall, J. E. M. *Science* 2012, *247* (4943), 669–678.

(85) Alivisatos, A. P. *Science* 1996, *271*, 933–937.

(86) Vennerberg, D.; Lin, Z. *Sci. Adv. Mater.* 2011, *3* (1), 26–40.

(87) Pokutnii, S. I. *Semiconductors* 2010, *44* (4), 488–493.

(88) Shukla, R.; Bansal, V.; Chaudhary, M.; Basu, A.; Bhonde, R. R.; Sastry, M. *Langmuir* 2005, *21* (23), 10644–10654.

(89) Murphy, C. J.; Gole, A. M.; Stone, J. W.; Sisco, P. N.; Alkilany, A. M.; Goldsmith, E. C.; Baxter, S. C. *Acc. Chem. Res.* 2008, *41* (12), 1721–1730.

(90) Connor, E. E.; Mwamuka, J.; Gole, A.; Murphy, C. J.; Wyatt, M. D. *Small* 2005, *1* (3), 325–327.

(91) Ghosh, S. K.; Pal, T. *Chem. Rev.* 2007, *107* (11), 4797–4862.

(92) Sreenivasan, V. K. A.; Zvyagin, A. V; Goldys, E. M. *J. Phys. Condens. Matter* 2013, *25* (19), 1–23.

(93) Auzel, F. *J. Luminesc.* 1990, *45* (1-6), 341–345.

(94) Hao, S.; Chen, G.; Yang, C. *Theranostics* 2013, *3* (5), 331–345.

(95) Wang, M.; Abbineni, G.; Clevenger, A.; Mao, C.; Xu, S. *Nanomedicine* 2011, *7* (6), 710–729.

(96) Wang, F.; Liu, X. *Chem. Soc. Rev.* 2009, *38*, 976–989.

(97) Aboshyan-Sorgho, L.; Besnard, C.; Pattison, P.; Kittilstved, K. R.; Aebischer, A.; Bünzli, J. C. G.; Hauser, A.; Piguet, C. *Angew. Chem.* 2011, *50*, 4108–4112.

(98) Dong, H.; Sun, L. D.; Yan, C. H. *Nanoscale* 2013, *5* (13), 5703–5714.

(99) Suyver, J. F.; Aebischer, A.; Biner, D.; Gerner, P.; Grimm, J.; Heer, S.; Krämer, K. W.; Reinhard, C.; Güdel, H. U. *Opt. Mater.* 2005, *27* (6), 1111–1130.

(100) Wang, F.; Deng, R.; Wang, J.; Wang, Q.; Han, Y.; Zhu, H.; Chen, X.; Liu, X. *Nature Mater.* 2011, *10* (12), 968–973.

(101) Joubert, M. F. *Opt. Mater.* 1999, *11*, 181–203.

(102) Yamada, N.; Shigeo, S.; Kushida, T. *J. Phys. Soc. Jpn.* 1972, *32* (6), 1577–1586.

(103) Suyver, J. F.; Grimm, J.; Kramer, K. W.; Gudel, H. U. *J. Luminesc.* 2005, *114*, 53–59.

(104) Shan, J.; Qin, X.; Yao, N.; Ju, Y. *Nanotechnology* 2007, *18* (44), 607–614.

(105) Haase, M.; Schäfer, H. *Angew. Chem.* 2011, *50* (26), 5808–5829.

(106) van Dijk, J. M. F.; Schuurmans, M. F. H. *J. Chem. Phys.* 1983, *78* (9), 5317–5323.

(107) Bunzli, J. C. G.; Eliseeva, S. V. *Basics of Lanthanide Photophysics*; Hanninen, P., Harma, H., Eds.; Lausanne, 2011.

(108) Bünzli, J. C. G.; Comby, S.; Chauvin, A. S.; Vandevyver, C. D. B. *J. Rare Earths* 2007, *25*, 257–274.

(109) Dongdong, L. I.; Qiyue, S.; Yan, D.; Jianqing, J. *J. Rare Earths* 2014, *32* (11), 1032–1036.

(110) Auzel, A. *Chem. Rev.* 2004, *104* (1), 139–173.

(111) Li, Z.; Zhang, Y.; Jiang, S. *Adv. Mater.* 2008, *20* (24), 4765–4769.

(112) Chao, Z.; Lingdong, S. U. N.; Yawen, Z.; Chunhua, Y. A. N. *J. Rare Earths* 2010, *28* (6), 807–819.

(113) Sivakumar, S.; Van Veggel, F. C. J. M.; May, P. S. *J. Am. Chem. Soc.* 2007, *129* (3), 620–625.

(114) Lin, C.; Berry, M. T.; Anderson, R.; Smith, S.; May, P. S. *Chem. Mater.* 2009, *5*, 3406–3413.

(115) Zhang, F.; Li, J.; Shan, J.; Xu, L.; Zhao, D. *Eur. J. Chem.* 2009, *15*, 11010–11019.

(116) Liao, J.; Yang, Z.; Wu, H.; Yan, D.; Qiu, J.; Song, Z.; Yang, Y.; Zhou, D.; Yin, Z. *J. Mater. Chem. C* 2013, *1* (40), 6541.

(117) Renero-Lecuna, C.; Martín-Rodríguez, R.; Valiente, R.; González, J.; Rodríguez, F.; Krämer, K. W.; Güdel, H. U. *Chem. Mater.* 2011, *23*, 3442–3448.

(118) Wang, F.; Banerjee, D.; Liu, Y.; Chen, X.; Liu, X. *Analyst* 2010, *135*, 1839–1854.

(119) Liang, X.; Wang, X.; Zhuang, J.; Peng, Q.; Li, Y. *Adv. Funct. Mater.* 2007, *17*, 2757–2765.

(120) Li, C.; Quan, Z.; Yang, J.; Yang, P.; Lin, J. *Inorg. Chem.* 2007, *46* (16), 6329–6337.

(121) Wang, F.; Wang, J.; Liu, X. *Angew. Chem.* 2010, *49* (41), 7456–7460.

(122) Shannon, R. D. *Acta Cryst.* 1976, *32* (5), 751–767.

(123) Wang, F.; Han, Y.; Lim, C. S.; Lu, Y.; Wang, J.; Xu, J.; Chen, H.; Zhang, C.; Hong, M.; Liu, X. *Nature* 2010, *463* (7284), 1061–1065.

(124) Kuisheng, Y. *J. Rare Earths* 2006, *24*, 162–166.

(125) Vetrone, F.; Boyer, J. C.; Capobianco, J. A.; Speghini, A.; Bettinelli, M. *J. Appl. Phys.* 2004, *96* (1), 661–667.

(126) Mai, H. X.; Zhang, Y. W.; Si, R.; Yan, Z. G.; Sun, L. D.; You, L. P.; Yan, C. H. *J. Am. Chem. Soc.* 2006, *128* (19), 6426–6436.

(127) Boyer, J. C.; Vetrone, F.; Cuccia, L. A.; Capobianco, J. A. *J. Am. Chem. Soc.* 2006, *128* (23), 7444–7445.

(128) Muhr, V.; Wilhelm, S.; Hirsch, T.; Wolfbeis, O. S. *J. Am. Chem. Soc.* 2014, *47* (12), 3481–3493.

(129) Darbandi, M.; Thomann, R.; Nann, T. *Chem. Mater.* 2005, *17* (23), 5720–5725.

(130) Yi, D. K.; Selvan, S. T.; Lee, S. S.; Papaefthymiou, G. C.; Kundaliya, D.; Ying, J. Y. *J. Am. Chem. Soc.* 2005, *127* (14), 4990–4991.

(131) Xie, P.; Rand, S. C. *Opt. Lett.* 1992, *17* (17), 1198–1200.

(132) Gibart, P.; Auzel, F.; Guillaume, J.-C.; Zahraman, K. *Jpn. J. Appl. Phys.* 1996, *351* (8), 4401–4402.

(133) Liu, Y.; Ai, K.; Lu, L. *Nanoscale* 2011, *3* (11), 4804–4810.

(134) Meruga, J. M.; Cross, W. M.; May, P. S.; Luu, Q.; Crawford, G. A.; Kellar, J. J.

Nanotechnology 2012, *23* (9), 395201.

(135) Carling, C. J.; Boyer, J. C.; Branda, N. R. *J. Am. Chem. Soc.* 2009, *131* (31), 10838–10839.

(136) Boyer, J. C.; Carling, C. J.; Gates, B. D.; Branda, N. R. *J. Am. Chem. Soc.* 2010, *132* (44), 15766–15772.

(137) Zijlmans, H. J.; Bonnet, J.; Burton, J.; Kardos, K.; Vail, T.; Niedbala, R. S.; Tanke, H. J. *Anal. Biochem.* 1999, *267* (1), 30–36.

(138) Lim, S. F.; Riehn, R.; Ryu, W. S.; Khanarian, N.; Tung, C. K.; Tank, D.; Austin, R. H. *Nano Lett.* 2006, *6* (3), 169–174.

(139) Chatterjee, D.; Rufaihah, A.; Zhang, Y. *Biomaterials* 2008, *29* (7), 937–943.

(140) Hampl, J.; Hall, M.; Mufti, N. A.; Yao, Y. M.; MacQueen, D. B.; Wright, W. H.; Cooper, D. E. *Anal. Biochem.* 2001, *288* (2), 176–187.

(141) Corstjens, P. L. A. M.; Van Lieshout, L.; Zuiderwijk, M.; Kornelis, D.; Tanke, H. J.; Deelder, A. M.; Van Dam, G. J. *J. Clin. Microbiol.* 2008, *46* (1), 171–176.

(142) Liu, B.; Tan, H.; Chen, Y. *Anal. Chim. Acta* 2013, *761*, 178–185.

(143) Bejar, M.; Liras, M. *J. Mater.* 2014, *2* (28), 1–19.

(144) Hamze, A.; Provot, O.; Alami, M.; Brion, J. D. *Org. Lett.* 2005, *7* (25), 5625–5628.

(145) Zhong, F.; Karatay, A.; Zhao, L.; Zhao, J.; He, C.; Zhang, C.; Yaglioglu, H. G.; Elmali, A.; Küçüköz, B.; Hayvali, M. *Inorg. Chem.* 2015, *54* (16), 7803–7817.

(146) Verwilst, P.; David, C. C.; Leen, V.; Hofkens, J.; De Witte, P. A. M.; De Borggraeve, W. M. *Bioorg. Med. Chem. Lett.* 2013, *23* (11), 3204–3207.

(147) Gibbs, J. H.; Wang, H.; Bhupathiraju, N. V. S. D. K.; Fronczek, F. R.; Smith, K. M.; Vicente, M. G. H. *J. Organomet. Chem.* 2015, 5–9.

(148) Yogo, T.; Urano, Y.; Ishitsuka, Y.; Maniwa, F.; Nagano, T. *J. Am. Chem. Soc.* 2005, *127*, 12162–12163.

(149) Zhang, X. F.; Yang, X. *J. Phys. Chem. B* 2013, *117* (18), 5533–5539.

(150) Jahani, F.; Tajbakhsh, M.; Golchoubian, H.; Khaksar, S. *Tetrahedron Lett.* 2011, *52* (12), 1260–1264.

(151) Fairlamb, I. J. S.; Bäuerlein, P. S.; Marrison, L. R.; Dickinson, J. M. *Chem. Commun.* 2003, (5), 632–633.

(152) Negishi, E.; Anastasia, L. *Chem. Rev.* 2003, *103* (5), 1979–2017.

(153) Jin, G. F.; Cho, Y.; Wee, K.; Hong, S. A.; Suh, I.; Son, H.; Lee, J.; Han, W.; Cho, D. W.; Kang, S. O. *Dalton Trans.* 2015, *44* (6), 2780–2787.

(154) Frisch, M. J.; Trucks, G. W.; Schlegel, H. B.; Scuseria, G. E.; Robb, M. A.; Cheeseman, J. R.; Scalmani, G.; Barone, V.; Mennucci, B.; Petersson, G. A. ; Nakatsuji, H.; Caricato, M.; Li, X.; Hratchian, H. P.; Ismaylov, A. F.; Bloino, J.; Zheng, G.; Sonnenberg, J. L.; Hada, M.; Ehara, M.; Toyota, K.; Fukuda, R.; Hasegawa, J.; Ishida, M.; Nakjima, Y.; Honda, Y.; Kitao, O.; Nakai, H.; Vreven, T.; Montgomery, J. A.; Jr, Peralta, J. E.; Ogliaro, F.; Bearpark, M.; Heyd, J. J.; Brothers, E.; Kudin, K. N.; Staroverov, R.; Kobayashi, V. N.; Normand, K.; Raghavachari, J.; Rendell, A.; Burant, J. C.; Iyengar, S. S.; Tomasi, J.; Cossi, M.; Rega, N.; Millam, M. J.; Klene, M.; Knox, J. E.; Cross, J. B.; Bakken, V.; Adamo, C.; Jaramillo, J.; Gomperts, R.; Stratmann, R. E.; Yazyev, O.; Austin, A. J.; Cammi, R.; Pomelli, C.; Ochterski, J. W.; Martin, R. L.; Morokuma, K.; Zakrzewski, V. G.; Voth, G. A.; Salvador, P.; Dannenberg, J. J.; Dapprich, S.; Daniels, A. D.; Farkas, Ö.; Foresman, J. B.; Ortiz, J. V.; Cioslowski, J.; Fox, D. J. Gaussian Inc.: Wallingford CT 2009, 19, 227–238.

(155) Becke, A. D. *J. Chem. Phys.* 1993, *98* (7), 5648–5652.

(156) Lu, H.; Mack, J.; Yang, Y.; Shen, Z. *Chem. Soc. Rev.* 2014, *43* (13), 4778–4823.

(157) Gouterman, M. *The Porphyrins, Vol lll*, D. Dolphin. (Ed.); Academic Press: New York, 1978, pp. 1–165.

(158) Michl, J. *J. Am. Chem. Soc.* 1973, *365* (13), 6801–6811.

(159) Sreenivasan, V. K. A.; Zvyagin, A. V; Goldys, E. M. *J. Phys. Condens. Matter* 2013, *25* (19), 194101.

(160) Parres-Esclapez, S.; Illán-Gómez, M. J.; de Lecea, C. S.-M.; Bueno-López, A. *Appl. Catal. B Environ.* 2010, *96* (3-4), 370–378.

(161) Mai, H. X.; Zhang, Y. W.; Sun, L. D.; Yan, C. H. *J. Phys. Chem. C* 2007, *111*, 13730–13739.

(162) Ding, M.; Chen, D.; Yin, S.; Ji, Z.; Zhong, J.; Ni, Y.; Lu, C.; Xu, Z. *Sci. Rep.* 2015, *5*, 1–14.

(163) Xiong, L. Q.; Chen, Z. G.; Yu, M. X.; Li, F. Y.; Liu, C.; Huang, C. H. *Biomaterials* 2009, *30* (29), 5592–5600.

(164) Kim, J.; Kang, S.; Hong, S.; Yum, S.; Kim, Y. M.; Jung, Y. *Eur. J. Med. Chem.* 2012, *48*, 36–44.

(165) Watkins, Z.; Taylor, J.; D'Souza, S.; Britton, J.; Nyokong, T. *J. Fluoresc* 2015, *25* (5), 1417–1429.

(166) Wang, M.; Hou, W.; Mi, C.; Wang, W.; Xu, Z.; Teng, H.; Mao, C.; Xu, S. *Anal. Chem.* 2009, *81* (21), 8783–8789.